Renewable and Sustainable Energy Reviews 203 (2024) 114740

Contents lists available at ScienceDirect

Renewable and Sustainable Energy Reviews

journal homepage: www.elsevier.com/locate/rser

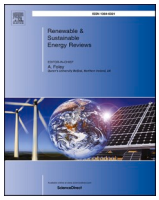

Chemical vapor deposition-grown graphene transparent conducting electrode for organic photovoltaics: Advances towards scalable transfer-free synthesis

Michael S.A. Kamel [a,b,**], Michael Oelgemöller [c], Mohan V. Jacob [a,*]

[a] Electronic Materials Research Lab, College of Science and Engineering, James Cook University, Townsville, 4811, Australia
[b] Physics Department, Faculty of Science, Minia University, P.O. Box 61519, Minia, Egypt
[c] Hochschule Fresenius gGmbH-University of Applied Sciences, Faculty of Chemistry and Biology, D-65510, Idstein, Germany

ARTICLE INFO

Keywords:
Chemical vapor deposition
Transfer-free graphene
Transparent conducting electrode
Doping
Post-treatment
Scalable CVD-Graphene production

ABSTRACT

Chemical vapor deposition (CVD)-grown graphene has gained significant attention as a potential alternative to indium tin oxide (ITO) transparent conducting electrode (TCE) for organic photovoltaics (OPVs). However, the high cost, complex manufacturing process, and elevated deposition temperatures limit the widespread application of CVD-graphene for TCEs. Furthermore, the transfer of CVD-graphene from the growth substrate (metal catalyst) onto the transparent target substrate (e.g. glass, PET, etc.) can result in substantial degradation of the graphene characteristics. Therefore, the direct growth of high-quality CVD-graphene on transparent substrates is an ultimate goal. Plasma-enhanced CVD facilitates graphene growth on dielectric substrates, but the resulting films often exhibit high sheet resistance and structural defects. This critical review discusses the advancements in CVD-graphene TCEs over the past decade. It investigates the synthesis of CVD-graphene on metal catalysts and explores various transfer methods in detail. The growth of CVD-graphene on dielectric substrates and the different strategies proposed to enhance its properties for TCE applications are scrutinized. More importantly, the most recent advances in single-step manufacture of CVD-graphene TCEs are discussed. This report also presents new insights and perspectives to address the current challenges of scalable production of transfer-free graphene TCEs for OPVs and other optoelectronics.

List of abbreviations

A	Acceptor/electron acceptor
AFM	Atomic force microscope
AgNWs	Silver nanowires
AgNWs-Gr	Silver nanowires-graphene, with graphene is grown on silver nanowires
Ar	Argon
B.E.	Binding energy
BHJ	Bulk heterojunction
C_2H_2	Ethyne
C_2H_6	Ethane
C_6H_6	Benzene
CH_4	Methane
CNTs	Carbon nanotubes
CTL	Charge transport layer
CVD	Chemical vapor deposition
D	Donor/electron donor
dc	Direct current
EB	Electron beam
E_f	Fermi level
EG	Exfoliated graphene
E_g	Bandgap
E-Gr	Epitaxial graphene
ETL	Electron transport layer
EVA	Ethylene vinyl acetate
FF	Fill factor
FLG	Few-layer graphene
FoM	Figure of merit
FOSCs	Flexible organic solar cells
GQDs	Graphene quantum dots
Gr-AgNWs	Graphene-silver nanowires, with silver nanowires are coated on top of graphene

(continued on next column)

(continued)

(continued on next page)

* Corresponding author.
** Corresponding author. Electronic Materials Research Lab, College of Science and Engineering, James Cook University, Townsville, 4811, Australia.
E-mail addresses: michael.kamel@my.jcu.edu.au (M.S.A. Kamel), mohan.jacob@jcu.edu.au (M.V. Jacob).

https://doi.org/10.1016/j.rser.2024.114740
Received 22 November 2023; Received in revised form 25 June 2024; Accepted 8 July 2024
Available online 20 July 2024

(*continued*)

H_2	Hydrogen
HOMO	Highest occupied molecular orbital
HTL	Hole transport layer
IPA	Isopropyl alcohol
ITO	Indium tin oxide
J	Current density
J_{max}	Maximum current density of the solar cell
J_{SC}	Short-circuit current density
J-V	Current density-Voltage
LUMO	Lowest unoccupied molecular orbitals
MLG	Multi-layer graphene
MoO_3	Molybdenum trioxide
MW-PECVD	Microwave plasma enhance chemical vapor deposition
NWs	Nanowires
OLEDs	Organic light emitting diodes
OPVs	Organic photovoltaics
OSCs	Organic solar cells
P	Power density
P3HT	Poly (3-hexylthiophene)
PAHs	Polycyclic aromatic hydrocarbons
PAN	Polyacrylonitrile
PATCVD	Plasma assisted thermal chemical vapor deposition
$PC_{70}BM$/ $PC_{71}BM$	[6,6]-Phenyl-C71-butyric acid methyl ester
PCBM/ $PC_{60}BM$	Phenyl-C61-butyric acid methyl ester
PCE	Power conversion efficiency
PECVD	Plasma enhanced chemical vapor deposition
PEDOT: PSS	poly (3,4-ethylenedioxythiophene) polystyrene sulfonate
PEN	Polyethylene naphthalate
PES	Polyestersulfone
PET	Polyethylene terephthalate
PFSA	Perfluorinated sulfonic acid
PI	polyimide
P_{max}	Maximum power density generated by the solar cell
PMMA	Poly methyl methacrylate
PS	Polystyrene
PSCs	Perovskite solar cells
PVA	Polyvinyl alcohol
R2R	Roll-to-roll
RF	Radio frequency
RF-PECVD	Radio frequency plasma enhanced chemical vapor deposition
RH	Relative humidity
rms	Root mean square
R_s	Sheet resistance
R_{ser}	Series resistance
R_{sh}	Shunt resistance
sccm	Standard cubic centimeter per minute
SEM	Scanning electron microscope
SLG	Single-layer graphene
TCE	Transparent conducting/conductive electrode
TEM	Transmission electron microscope
TFSA	Bis(trifluoromethanesulfonyl)amide
TiO_2	Titanium oxide
TRT	Thermal release tape
UPS	Ultraviolet photoelectron spectroscopy
UV	Ultraviolet
V	Voltage
VG	Vertically-oriented graphene
V_{max}	Maximum voltage of the solar cell
V_{OC}	Open-circuit voltage
WCA	Water contact angle
WF	Work function
WT	Wet transfer
XPS	X-ray photoelectron spectroscopy
ZnO	Zinc oxide

1. Introduction

Organic photovoltaics (OPVs) have achieved high records of power conversion efficiency (PCE), which push this promising technology towards large-scale commercialization [1–3]. Their mechanical flexibility, lightweight, low fabrication cost, and material abundancy make OPVs an excellent candidate to replace expensive first- and second-generation PV systems such as crystalline silicon, CdTe, and CuInSe solar cells [4–7]. In addition, the solution processability enables the roll-to-roll (R2R) fabrication and ink-jet printing of OPVs for flexible and wearable electronics applications [8–10]. However, there are major challenges for OPVs that should be resolved before they can enter the PV market. A typical OPV device consists of a p-type and an n-type organic semiconductors, which represent the photoactive layer of the device where light absorption occurs, sandwiched between a transparent and a semi-transparent or opaque electrode. In addition, two charge transport layers (CTLs) are typically deposited between the photoactive layer and the two electrodes to facilitate the transport and collection of the photo-generated charge carriers [4,11,12]. More details on the structure of OPVs and how they function are given in section 2. Thus, the transparent conducting electrode (TCE) is a major component in an OPV device, which acts as the window electrode that allows incident sunlight to reach the photoactive layer of the device. Moreover, it collects charge carriers (electrons or holes) generated through light absorption within the active layer. Therefore, the window electrode should possess high optical transmittance and high electrical conductivity to be an efficient TCE [13–15].

Transparent conducting oxides such as indium tin oxide (ITO) are the most commonly used TCEs for OPVs and other optoelectronic devices due to their good optical and electrical properties [13,16,17]. Nonetheless, the drawbacks of ITO such as poor mechanical and chemical stabilities [18,19], the scarcity of indium and the high fabrication expense [20,21] demand efficient alternatives. It has been reported that the ITO is responsible for almost 30 % of the overall fabrication cost of an OPV device [22]. Furthermore, the need for high vacuum and high temperature during ITO preparation by sputtering techniques consume up to 87 % of the total energy consumed during R2R fabrication of OPVs [23,24]. More importantly, the ceramic nature of ITO makes it prone to cracking, which limits its applicability in flexible optoelectronic devices [25,26]. Consequently, the development of ITO-free OPVs has received intensive research interest over the past years in order to make this promising technology more reliable and cost-effective [27–32]. A wide range of materials has been proposed to replace ITO for OPVs and other optoelectronics applications. This included metal thin films [33,34], metal oxides [35], and conducting polymers [36]. More importantly, low-dimensional materials such as carbon nanotubes (CNTs) (1D material) [37], silver nanowires (AgNWs) (1D material) [31,38–40], and graphene (2D material) [41] have shown great potential as TCE candidates. Among the above-mentioned materials, graphene received the greatest attention as an ITO substitute thanks to its extraordinary optical, electrical, and mechanical properties [42–44].

The production of graphene TCEs for optoelectronic devices by a variety of techniques has been broadly investigated over the past years. Chemical vapor deposition (CVD) has shown the greatest potential to produce high-quality and scalable graphene films for optoelectronics. In a CVD process, graphene is grown on a metal catalyst surface (nickel, copper, etc.) from carbon-containing reactants, in a gaseous form, at elevated temperatures (~1000 °C) and with the help of carrier gas/es [14]. The high purity, finely grained structure, and high stiffness of graphene films produced by CVD made it the most commonly used method to prepare graphene TCEs [41,45–47]. However, there are many drawbacks associated with CVD graphene such as elevated costs, time-consumption, the use of environmentally-hazardous and unsustainable carbon sources (e.g. methane and ethane), and the application of explosive carrier gases (e.g. H_2). Moreover, graphene films can be damaged during the complex transfer procedures from the catalyst to the transparent substrate (polymer, glass, etc.) [41].

Consequently, substantial research effort has been devoted to develop damage-free transfer processes [48–51] and to adopt plasma-enhanced CVD (PECVD) to reduce reaction temperature and time, which paved the way towards transfer-free graphene production [52–54]. Nevertheless, there are crucial issues with the PECVD-grown graphene such as its high sheet resistance (R_s), high structural defect

concentration, environmental impact, and relatively high cost that limit their scalability for optoelectronics. Several approaches have been investigated to make CVD- and PECVD-graphene feasible TCEs for OPVs and other optoelectronic devices [55,56]. Despite these, further research is still needed to realize high quality, affordable, and transfer-free CVD-based graphene TCEs.

The primary aim of this review is to establish a promising platform that can facilitate the single-step and commercial production of high-quality CVD-graphene TCEs on transparent substrates in the near future. To achieve this, the recent advancements and existing challenges associated with CVD-graphene TCEs for OPVs are comprehensively reviewed. Notably, critical issues related to scalability and sustainability of CVD-graphene TCEs are emphasized. Furthermore, this article offers perspectives and insights into the prospects of achieving scalable and transfer-free production of high-quality CVD-graphene TCEs. Addressing these key concerns represents a significant step forward in the advancement of ITO-free optoelectronics. For a better understanding of the topic, a brief overview of OPVs, graphene, and CVD is given first. To

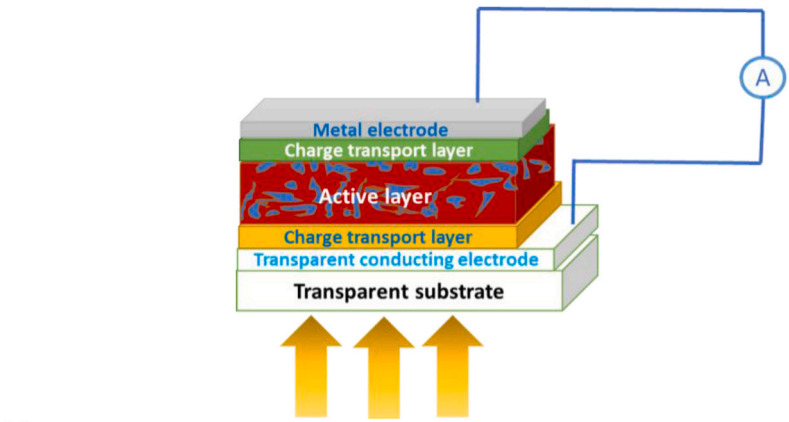

(a)

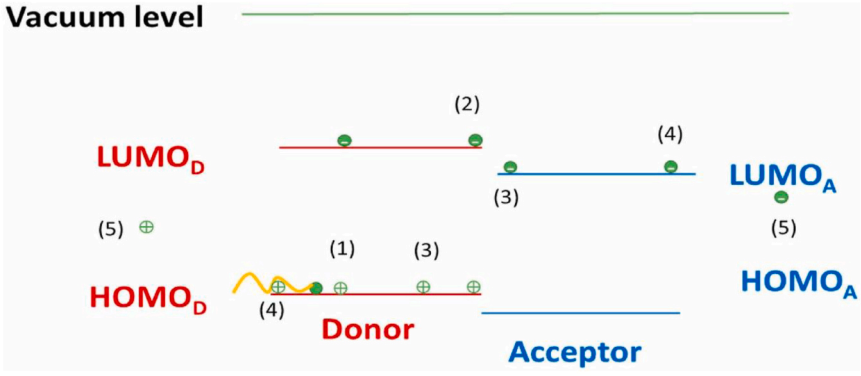

(b)

(d)

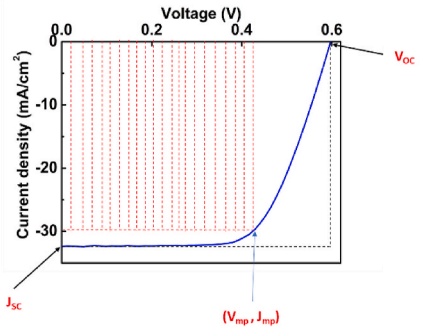

(c)

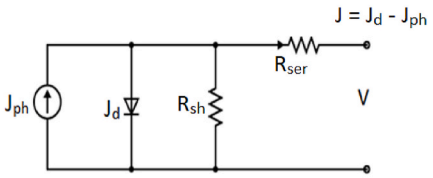

Fig. 1. a) Structure of a BHJ OPV device. b) A schematic diagram showing the different steps of the PV effect in BHJ OPVs, reproduced from Ref. [4] (1) light absorption and generation of exciton, (2) exciton diffusion towards D/A interfaces, (3) exciton dissociation into a free electron and a free hole, (4) free charge carriers transport towards the anode and the cathode where they can be collected (5) to produce photocurrent. c) The J-V curve of a typical solar cell under illumination. d) Equivalent circuit of a solar cell device. The photocurrent (J_{ph}) is represented by a current source in an opposite direction to the dark current (J_d). The net illumination current (J) is the difference between both currents.

the best of the authors' knowledge, a few articles on graphene prepared by different methods for optoelectronic applications can be found in literature [20,41]. Yet, none of them was fully dedicated to CVD-grown graphene TCEs for OPVs. More importantly and more specifically, no review articles on the transfer-free and large-scale production of CVD-graphene TCEs can be found. This work will help researchers to develop low-cost and large-scale transfer-free CVD-graphene TCEs which should accelerate the commercialization of OPVs and other renewable energy technologies (e.g. perovskite solar cells)".

2. Fundamentals

2.1. Organic photovoltaics – device structure and operation

The structure of a typical bulk heterojunction (BHJ) OPV device is shown in Fig. 1a. The device consists of a number of thin film layers with thicknesses ranging from a few to around 200 nm, deposited on top of a transparent substrate (e.g. glass, PET, PEN, etc.). The incident sunlight passes through the TCE and the first CTL before reaching the photoactive layer where it is absorbed. The active layer of a BHJ OPV device consists of p-type and n-type organic semiconductors, namely electron donor (D) and electron acceptor (A), blended together to form interpenetrating networks. Photons with adequate energies are absorbed by the D material and an exciton (a bound state of electron-hole pair) is created. The photo-generated excitons diffuse towards the D-A interfaces and dissociate into free charge carriers before they can recombine. Nano-scale interpenetrating networks between the D and A materials in the BHJ structure enhance the diffusion of excitons and reduces their recombination rate [57]. Then, the free electrons and holes are transported within the A and D materials to be collected at the cathode and the anode, respectively. The presence of CTLs facilitates the transport and collection of the charge carriers. The main stages of the photovoltaic effect in an OPV device are depicted in Fig. 1b.

The performance of a solar cell is evaluated by studying its current density (J)-voltage (V), i.e. J-V characteristic curve. Device performance can be described by a number of photovoltaic parameters calculated from the J-V curve, namely short-circuit current density (J_{SC}), open-circuit voltage (V_{OC}), fill factor (FF) and PCE. The J-V curve of a typical solar cell under illumination conditions are shown in Fig. 1c. PCE is defined as the ratio between the maximum power density (P_{max}) delivered by the cell and the power density of the incident light P_{in}. The power density (P) delivered by the solar cell to the external load is the product of V and the corresponding J, which is represented by the area under the J-V curve. Although J_{SC} and V_{OC} are the maximum current density and voltage of the device, the power density at those two points is zero. The current density and voltage at the point of maximum power density (P_{max}) of the J-V curve, J_{max} and V_{max}, always shift from the maximum theoretical values (J_{SC} and V_{OC}) as shown in Fig. 1c.

The deviation of J_{max} and V_{max} from J_{SC} and V_{OC} is mainly attributed to losses associated with the electric resistance offered by the bulk semiconductor, metallic electrodes and the contact between the semiconductor and the electrodes, which act as a series resistance (R_{ser}) connected to the ideal circuit that represents the device as shown in Fig. 1d. In addition, other losses are due to the leakage of the photo-generated current through the defects within the junction or at edges of the cell. Those defects act as alternative paths for the photo-generated charge carriers and these losses can be expressed by a parallel resistance connected with the cell known as shunt resistance (R_{sh}) (Fig. 1d). Thus, for an efficient solar cell, the value of R_{sh} should be as large as possible while R_{ser} should be minimized. The values of R_{ser} and R_{sh} can be calculated from the J-V curve using the slope of tangents at J_{SC} and V_{OC}, respectively [58].

The ratio between P_{max} and the product of V_{OC} and J_{SC} gives rise to the *FF* which is a measure to the squareness of the J-V curve. *FF* is maximum when R_{ser} is minimum and R_{sh} is maximum and vice versa. The *FF* and PCE are related according to the following equations [59,60].

$$FF = \frac{P_{max}}{J_{SC} * V_{OC}} = \frac{J_{max} * V_{max}}{J_{SC} * V_{OC}} \quad (1)$$

$$PCE\ (\%) = \frac{P_{max}}{P_{in}} = \frac{FF * J_{SC} * V_{OC}}{P_{in}} \times 100\% \quad (2)$$

Based on this brief overview of the structure and performance of an OPV device, it can be concluded that an efficient TCE is crucial for realizing a highly performing device. An effective TCE should possess high light transmittance and excellent electrical conductivity. The R_s and morphology of the TCE directly affect R_{ser}, R_{sh}, and hence the overall performance of the associated OPV device. The exceptional features of intrinsic graphene such as its extraordinary electrical, optical, and structural properties make it an outstanding TCE candidate. Nonetheless, the properties of CVD-grown graphene can vary significantly from their intrinsic counterparts as a result of the synthesis process. Therefore, a solid understanding of the CVD of graphene and the underlying growth mechanisms is inevitable. More crucially, understanding the impact of the different deposition parameters on the properties of the resulting CVD-graphene film is essential to realize high-quality graphene sheets.

2.2. CVD-graphene

Graphene is a 2D material consisting of sp^2 hybridized carbon atoms bonded in a honeycomb structure with a single-atom thickness (Fig. 2a). The extended hexagonal graphene structure represents the fundamental building units for other carbon allotropes. For example, stacked graphene layers produce graphite (3D), while rolled and wrapped graphene result in CNTs (1D) and fullerenes (0D), respectively (Fig. 2b–d) [61]. The long-range π-conjugation (Fig. 2e) within its structure leads to the outstanding electrical, thermal, and mechanical properties of graphene [62]. Being a 2D material with a single-carbon atom thickness, graphene has excellent optical transmittance reaching 97.7 % for single-layer graphene (SLG) [63]. The remarkable electronic features of graphene are attributed to its high-quality 2D lattice, which shows a minimum density of defects that hinder charge transport as a result of scattering. The ballistic charge transport within graphene lattice is responsible for its high carrier mobility. A typical value of 2×10^5 cm^2 V^{-1} s^{-1} for the carrier mobility of graphene was experimentally reported [64]. A SLG is considered a zero-band gap semiconductor in which the valence and conduction band edges meet at a single point (Dirac point), while multi-layer graphene (MLG) exhibit metallic behaviour due to the overlap of the wave functions of their charge carriers [62]. Since it was first prepared by Geim and Novoselov [65] in 2004 through mechanical exfoliation of graphite (Fig. 2b) using Scotch tape, many approaches have been developed to synthesize large-area graphene for practical applications. These methods can be divided into two main mechanisms: top-down and bottom-up.

In a top-down approach, graphene is isolated from the 3D graphite structure via a peel-off process known as exfoliation [69]. The exfoliation process can be mechanical, chemical oxidation-reduction, electrochemical and liquid phase exfoliation [70]. In a mechanical exfoliation process, adhesive tape is used to peel off single to a few layer graphene (FLG) from highly oriented pyrolytic graphite, while an electric potential (voltage) is applied to achieve electrochemical exfoliation [71]. In a liquid phase exfoliation, a fast heating, sonication, or large shear force is used to exfoliate graphene layers after increasing the interlayer spacing in graphite via reducing the van der Waals forces through a reduction reaction [72]. Chemical oxidation-reduction exfoliation is the most common top-down synthesis approach in which graphite is first oxidized into graphite oxide via different ways such as Hummers' method using concentrated acids and strong oxidizing agents [73]. Then, graphite oxide is reduced into graphene through thermal, chemical, or electrochemical approaches [74–76]. More details on top-down graphene

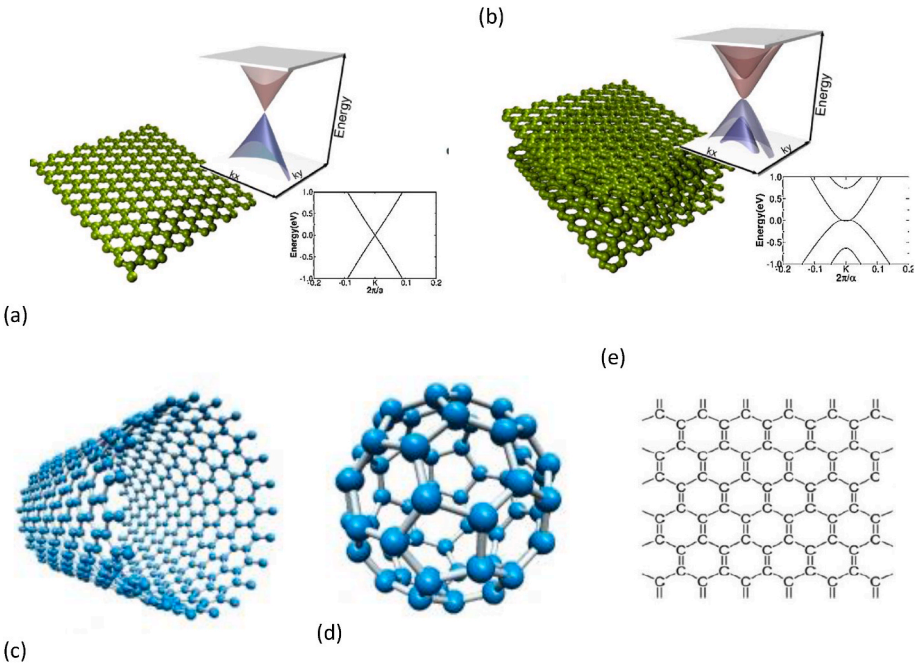

Fig. 2. The hexagonal honeycomb structure of graphene (a) and graphite structure consisting of stacked 3d graphene (b). The edges of the valence band and the conduction band meet at Dirac point for SLG and overlap for MLG structure, reproduced with permission from ref. [66]. Rolled and wrapped graphene sheet form CNTs (c) and fullerenes (d), adapted with permission from ref. [67]. (e) The chemical bonds within graphene lattice [68].

preparation of graphene can be found in the comprehensive review by Kumar et al. [70].

The second main approach for graphene production, the bottom-up methodology, uses hydrocarbons as carbon sources to synthesize graphene sheets on a growth substrate. Examples for bottom-up methods include CVD, epitaxial growth, thermal pyrolysis, laser-assisted and organic synthesis [77]. CVD is the most common bottom-up method due to its scalability, good quality of the resulting graphene, and relatively low cost [47]. The involved steps and the associated mechanism in CVD are discussed below.

A typical CVD process includes the passage of vapor of a carbon-containing precursor such as methane (CH_4) or ethane (C_2H_6) and carrier gases, mainly H_2 and Ar, though the surface of the growth substrate (often a metal catalyst e.g. Cu, Ni, etc.) at elevated temperature (around 1000 °C), where chemical bonds break and carbon atoms are bonded in the hexagonal 2D sheet of graphene. The growth mechanism of graphene by CVD includes three major steps: (1) decomposition of the hydrocarbon precursor vapor (dehydrogenation), (2) nucleation, and (3) growth or expansion, as shown in Fig. 3a [78]. Moreover, various processes can occur between the dehydrogenation and nucleation steps, depending on the substrate properties and other deposition parameters. For example, in case of a Ni catalyst substrate, the bulk diffusion of carbon atoms through Ni can be dominant due to its high carbon solubility, then carbon is segregated towards the Ni surface leading to other nucleation on the surface during the cooling down of the CVD reactor, leading to MLG films [79]. Consequently, it is difficult to obtain uniform graphene sheets without microstructure defects on metal catalysts with high carbon solubility. In contrast, metal catalysts with low carbon solubility such as Cu minimize the bulk diffusion of carbon atoms after the dehydrogenation step, and increase the surface migration of the

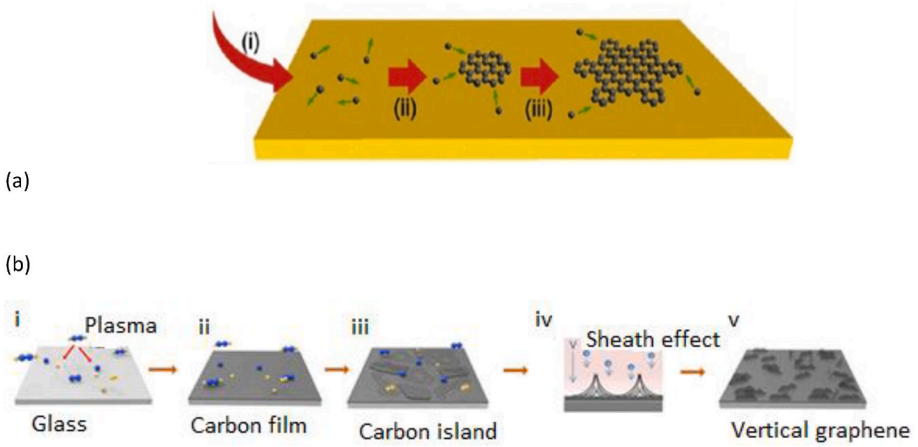

Fig. 3. Schematic representation of the growth of CVD graphene on Cu substrate (a), reproduced with a permission from ref. [82]. (b) Schematic growth process of VG film on glass substrate in a PECVD system. (i) Dissociation of carbon-hydrogen bonds by plasma. (ii) Formation of the carbon buffer layer on the glass substrate. (iii) Simultaneous growth of graphene and carbon islands. (iv) Sheath effect and ion bombardment between bulk plasma and the substrate. (v) Sparse distribution of VG nanosheets on the glass substrate, reproduced with a permission from ref. [83].

carbon adatoms towards nucleation sites on the catalyst surface, which facilitates the growth of SLG [80]. More crucially, the polycrystalline nature of the substrates can induce grain boundaries within graphene lattice, which diminish the electrical and optical properties of the resulting CVD-graphene. Also, the precursor (carbon source) represents another important factor that affects the CVD growth of graphene. The energy needed for the decomposition of the precursor vapor to produce active carbon species required for nucleation was found to vary significantly for different precursors, which remarkably affects the growth temperature. For instance, the use of liquid (benzene, C_6H_6) and solid precursors (poly methyl methacrylate, PMMA, and polystyrene, PS) enabled the growth of graphene on Cu foil at lower temperatures compared to CH_4 [81]. Additionally, the precursor type had a crucial impact on the quality of the resulting graphene as will be discussed in more detail later in this review.

For growing graphene on other substrates than metal catalysts, including dielectric substrates, PECVD is utilized. The plasma discharge provides part of the energy required for the precursor decomposition and for graphene growth, which can reduce the growth temperature of graphene on non-catalytic substrates. However, the growth mechanism of graphene in a PECVD process (Fig. 3b) differs from that in a conventional thermal CVD approach. Following the decomposition of the precursor molecules, the formation of a thin carbon buffer layer horizontal to the substrate surface is observed. This buffer layer can be graphene, graphite or amorphous carbon, depending on the deposition parameters [84]. Then, carbon islands form above the buffer layer prior to the growth of vertically oriented graphene (VG) nanosheets. The horizontal growth of graphene is not favored in a PECVD for the following reasons [83].

- Discontinuity in horizontal graphene sheets as a result of their simultaneous growth with carbon islands.
- Strain energy in the defects and edges within initial graphene, which may make the intermediate layer unable to have a complete 2D film, but 3D crystals instead [85].
- The collisions of the energetic ions in plasma with the substrate surface resulting in defects in graphene surface and supporting the growth of VG.

Thus, the properties of the resulting graphene can be adjusted for a particular application through the optimization of the deposition parameters. In the following sections, the implementation of CVD and PECVD based graphene TCEs for OPVs is discussed in detail. More importantly, the progress made towards single-step (transfer-free) of graphene TCEs is comprehensively investigated.

3. Characterization methods of graphene TCEs

The structural, optical, electrical and electronic properties of graphene are crucial to realize an efficient TCE for high-performing OPVs and other optoelectronics. In this section, the most common characterization methods used to assess graphene TCEs for OPVs are briefly discussed.

3.1. Raman spectroscopy

Raman spectroscopy is a fundamental characterization technique for graphene research which provides a fingerprint spectrum describing graphene sample. It is a powerful and non-destructive tool to get an in-depth insight on the quality, number of layers, and different structural defects of graphene. A typical Raman spectrum for graphene sample consists of a number of characteristic peaks at specific Raman shifts (cm^{-1}). The 2D peak (around 2670 cm^{-1}) is characteristic of the second order of the zone-boundary phonons and an evidence on the formation of the graphene-like structure [86]. Another characteristic peak is the G-peak (around 1570 cm^{-1}) which is associated with the in-plane E_{2g} vibration of sp^2 hybridized carbon [87]. Moreover, the structural imperfections of graphene are represented mainly by the D-peak (around 1340 cm-1) [88]. Other defect-related peaks are the D' (1610 cm^{-1}), D + D" (around 2426 cm^{-1}), D + G (around 2915 cm^{-1}), and 2D/(around 3210 cm^{-1}) [89]. The ratio of the intensity of the 2D to G peaks (I_{2D}/I_G) gives information on the number of graphene layers, with this ratio increases for lower number of layers. Whilst, the ratio of I_D/I_G gives insights on the structural defects in graphene sample, and increases with increased defects. For efficient graphene TCE for OPVs, the number of graphene layers should be optimized within the film to achieve high electrical conductivity (low sheet resistance) at reasonable optical transmittance. More details on Raman spectroscopy for graphene can be found in previous literature [88]. Typical representative Raman spectra for different graphene films will be discussed in the next sections.

3.2. Compositional, morphological and structural characterization

The purity of the graphene structure can be investigated using X-ray photoelectron spectroscopy (XPS) as a non-destructive method to determine the elemental composition of graphene film. XPS uses x-ray beam to irradiate the surface of the solid material under study (graphene film) and the kinetic energies of the ejected electrons (by photoelectric effect) from the top surface of the film (up to 10 nm) are recorded. The surface elements can be identified and quantified by the energies and intensities of the photoelectron peaks in XPS spectrum. Thus, XPS provides a quantitative analysis of the different elements in the graphene film. Detailed discussion on XPS spectra for graphene films can be found in our previous work [14,86,87].

Transmission electron microscope (TEM) is a powerful tool to study the nanostructure of graphene. TEM images present information on the number of graphene layers and structural imperfections as discussed in later sections. Scanning electron microscope (SEM) and atomic force microscope (AFM) are typically used to investigate the morphology and roughness of graphene films. A high surface roughness of TCE material can result in poor interface with the CTL which increases carrier recombination and degrades the device performance. Morphology optimization of graphene TCEs is critical especially for VG films as will be discussed in later sections. Representative TEM, SEM, and AFM images for graphene films will be presented and discussed in the next sections.

3.3. Four point probe measurements

The electrical properties of graphene TCE play a substantial role in realizing high-performance graphene-based OPV devices. The sheet resistance of the TCE material has a significant impact on the transfer of the photo-generated charge carriers. A high sheet resistance hinders the transport and collection of the dissociated photo carriers within the device leading to a high increase in carrier recombination. The series resistance of an OPV device depends strongly on the sheet resistance of the TCE material. The R_{ser} of the device increases with increasing the sheet resistance of the electrode. A high R_{ser} results in inefficient carrier collection and reduced *FF* and PCE. The sheet resistance of graphene films increases with structural defects. For MLG, the sheet resistance decreases with increasing the number of layers. Four point probe is the most common method to measure the sheet resistance of TCEs. In a four point setup, a fixed current is applied through the two external probes, while the two internal probes measure the voltage. The probes are equidistant. The sheet resistance of the electrode is determined from the slope of the straight line between the current and voltage according to the following equation [90,91]:

$$R_s = 4.53 \times C \frac{dV}{dI} \quad (3)$$

where, $\frac{dV}{dI}$ is the slope of the straight line I–V relation and C is a correction

that depends on sample dimensions and the distance between the probes. More details on the four-point measurements and setup can be found in our previous work [86,89].

3.4. Optical transmittance

The light transmission of a TCE material plays a vital role in determining the overall performance of the associated OPV device. An efficient TCE has to be as optically transparent as possible to allow as much incident sunlight to reach the photoactive layer of the device as possible. The optical transmittance of the TCE material strongly affects the J_{SC} and hence the PCE of the OPV device, with J_{SC} increases with increasing the transmittance of the TCE material. Graphene has outstanding optical transmittance (around 97.5 % for SLG) which makes it an ideal TCE candidate. FLG and MLG are used for TCE applications with the optical transmittance drops with increasing the number of layers. Thus, the number of layers has to be compromised to achieve optimum sheet resistance and optical transmittance. UV-VIS absorption and Ellipsometer are used to measure the optical transmittance of graphene TCEs.

3.5. Electronic properties

The electronic properties of graphene TCE have a crucial role in realizing a high efficiency OPV device. The work function of the graphene film is an important factor that determines a good contact with subsequent layers of the device. For efficient transport and collection of the charge carriers generated in the active layer, an efficient contact between the active layer and the TCE is essential. This means an Ohmic contact between the graphene TCE and the charge transport layer between the TCE and the active layer must be realized for efficient device performance. Therefore, the fermi level of the graphene film and the HOMO/LUMO/valence or conduction band edge of the CTL must be taken into consideration to achieve excellent interface between the active layer and graphene TCE. The work function of graphene can vary with film quality, number of layers, the presence of dopants, defects, grain boundaries, etc. Ultraviolet photoelectron spectroscopy (UPS) is a common method to determine the fermi level (work function) of graphene [92]. Graphene has excellent carrier mobility owing to the ballistic charge transport which results in outstanding electrical properties of graphene TCEs. Thus, carrier mobility affects the potential of graphene TCE to achieve an efficient OPV device. The excellent carrier mobility of intrinsic graphene greatly drops due to grain boundaries, vacancies, and other structural imperfections. Carrier mobility of graphene can be measured using the Hall effect method [93].

3.6. Surface wettability

Graphene is a hydrophobic material which represents a drawback in solution-processing OPV device fabrication. For instance, PEDOT: PSS aqueous solution and ZnO sol-gel are the most common HTL and ETL for regular and inverted geometry, respectively. In order to achieve a homogeneous and a uniform coating for the CTL, the graphene surface has to be engineered for enhanced wettability. For example, plasma treatment is an effective approach to decrease the hydrophobicity of graphene surface to achieve uniform coating of CTL. However, plasma treatment has to be conducted for short time and at low power to avoid graphene damage. Other surface modification strategies can include the deposition of ultrathin layer of MoO_3 on graphene surface or the addition of surfactant to the CTL solution [94]. Contact angle measurement is a common method to determine the surface wettability of graphene where a micro droplet of the CTL solution are dropped onto the graphene surface and the wetting angle at the point of contact with the substrate is measured. A low contact angle for graphene TCE is essential to deposit a uniform coating and hence a high-performing OPV device.

4. CVD graphene for OPVs

The implementation of CVD graphene as a TCE for optoelectronic devices has received a widespread research interest over the past decade. CVD shows promising potential towards the scalable production of graphene for large-scale application. In addition, the utilization of different forms of plasma with CVD enables graphene synthesis at lower temperatures and on a wide variety of substrates. In the following sections of this review, the progress in CVD-graphene based TCEs for OPVs over the past decade will be discussed. The current challenges and possible solutions are also highlighted.

4.1. Thermal CVD graphene for OPVs

A conventional thermal CVD reactor uses an external heater for the decomposition of the precursor vapor molecules, nucleation, and growth of graphene on the growth substrates. Due to the high temperature (~1000 °C) required for graphene synthesis, metal catalyst substrates such as Cu and Ni are the best choices for graphene deposition. Consequently, a graphene transfer procedure from the metal catalyst onto the transparent target substrate is necessary for TCE applications. Despite the high quality and scalability of the resulting CVD graphene on the metal catalyst, there is a high possibility of critical damage to the graphene features during the transfer process. Thus, multi-step transfer procedures are used to minimize graphene deformation, which increase the production cost of the TCE and the overall OPV device.

The formation of thin graphitic layers on transition metals-carbide and Ni substrates via CVD of hydrocarbon precursors has been known for almost half a century [95]. In the same regard, the growth of mono-layer carbon by surface adsorption or segregation of carbon on Ni and Co at high temperatures was observed four decades ago [96–98]. Nonetheless, the high carbon solubility of these metals leads to the formation of thicker graphite films by excess carbon while the substrate cools down. Many attempts were made to synthesize graphene on metal catalyst from solid (camphor) [99] and gaseous (methane) precursors [100]. Later in 2009, the production of SLG and FLG by CVD on metal catalyst substrates from CH_4 was reported by many research groups [95,101–103]. For instance, in order to avoid the growth of large graphite crystals, Kim et al. [95] deposited a 300 nm Ni film on the SiO_2/Si substrate using electron beam evaporation prior to the CVD step. Then, the Ni-coated Si substrate was heated inside a quartz tube at 1000 °C under an Ar atmosphere. The precursor gas mixture (CH_4: H_2: Ar = 50: 65: 200 sccm) was applied to the chamber and the samples were cooled down quickly under Ar at a rate of 10 °C per minute. The authors proposed that the rapid cooling played a vital role in inhibiting MLG growth and facilitated graphene expansion through the substrate. In the same year, Li and co-workers [102] reported CVD graphene on Cu foil (25 μm thick) using a CH_4 and H_2 mixture and demonstrated the potential of their approach to grow graphene on a 300 mm thick Cu film-coated Si substrate. In addition, they investigated the effect of both the deposition time and substrate thickness under constant temperature and pressure on the properties of the synthesized graphene. Interestingly, they observed that the structure of the graphene films grown for more than 1 h was very similar to that with 10-min deposition time, while for growth times ≪10 min the resulting graphene films did not fully cover the Cu foil. The variation of Cu foil thickness (12.5 μm, 25 μm, and 50 μm), under isothermal and isobaric conditions had no impact on the structure of the grown graphene films, which showed regions with double and triple flakes, but neither continuous MLG with thicker Cu foil nor discontinuous SLG with thinner Cu foil was noticed. These observations led them to the following important conclusions: the CVD of graphene on Cu is (1) a self-limited, (2) surface-catalysed process in contrast to the precipitation growth in case of Ni substrates [95,104,105].

In 2010, De Arco et al. reported CVD graphene TCEs with a good potential for rigid and flexible device applications [106]. In this work, SLG and FLG films were deposited on Ni-coated Si/SiO_2 wafers and then

transferred onto PET and glass substrates. First, a 100 nm layer of elemental Ni was deposited on the Si/SiO_2 wafer by thermal evaporation. Then, the Ni layer was annealed at high temperature (reaching 800 °C) in H_2: Ar (1: 10) atmosphere. The heating and cooling steps were conducted at a slow rate of 0.15 °C per minute so that polycrystalline Ni can form through the Si/SiO_2 substrate. Graphene deposition was subsequently performed at 900 °C under a 600 sccm H_2 flow and a 100 sccm flow of CH_4 for 8 min. The CVD-graphene TCEs exhibited R_s of 230

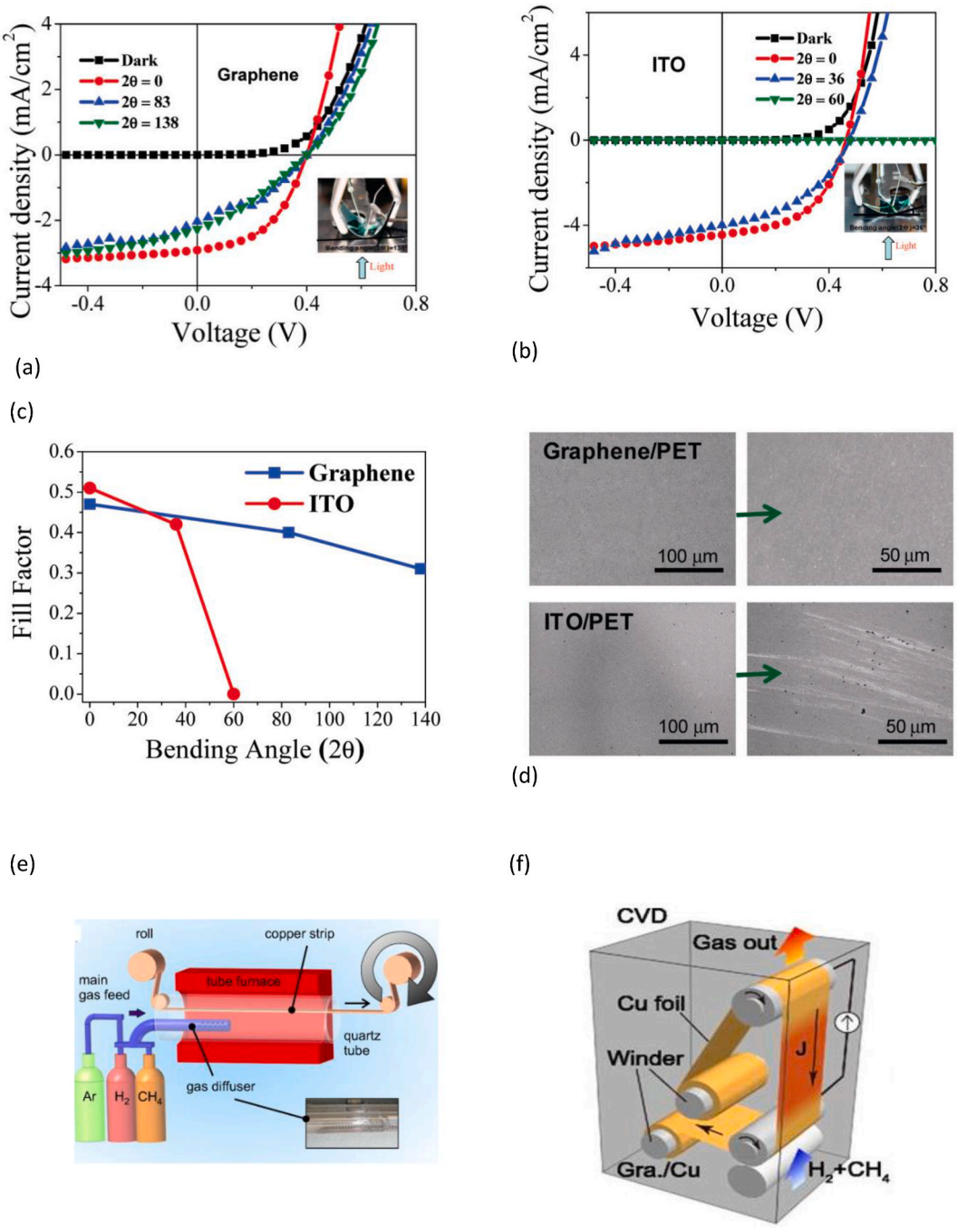

Fig. 4. Current density *vs* voltage characteristics of CVD graphene (a) or ITO (b) photovoltaic cells under 100 mW/cm^2 AM1.5G spectral illumination for different bending angles. Insets show the experimental setup employed in the experiments. (c) FF dependence of the bending angle for CVD graphene and ITO devices. (d) SEM images showing the surface structure of CVD graphene (top) and ITO (bottom) photovoltaic cells after being subjected to the bending angles described in panels a and b, adapted with a permission from ref.[106]. (e) Schematic representation of the CVD growth setup. Cu is fed continuously through the 25 mm diameter quartz tube furnace with a roll-to-roll system at a velocity of 1–40 cm/min. Ar and H_2 are fed into the main tube, whereas CH4 is provided through the gas diffuser system, reproduced with a permission from ref. [108]. (f) Continuous roll-to-roll CVD system using selective Joule heating to heat a copper foil suspended between two current-feeding electrode rollers to 1000 °C to grow graphene, reproduced with a permission from ref. [109]. Photographs of the roll-based production of graphene films. (g) Copper foil wrapping around a 7.5-inch quartz tube to be inserted into an 8-inch quartz reactor. The lower image shows the stage in which the copper foil reacts with CH4 and H2 gases at high temperatures. (h) Roll-to-roll transfer of graphene films from a thermal release tape to a PET film at 120 °C. (i) A transparent ultralarge-area graphene film transferred on a 35-inch PET sheet. (j) Screen printing process of silver paste electrodes on graphene/PET film. The inset shows 3.1-inch graphene/PET panels patterned with silver electrodes before assembly. (k) An assembled graphene/PET touch panel showing outstanding flexibility. (l) A graphene-based touch-screen panel connected to a computer with control software, reproduced with a permission from ref. [110].

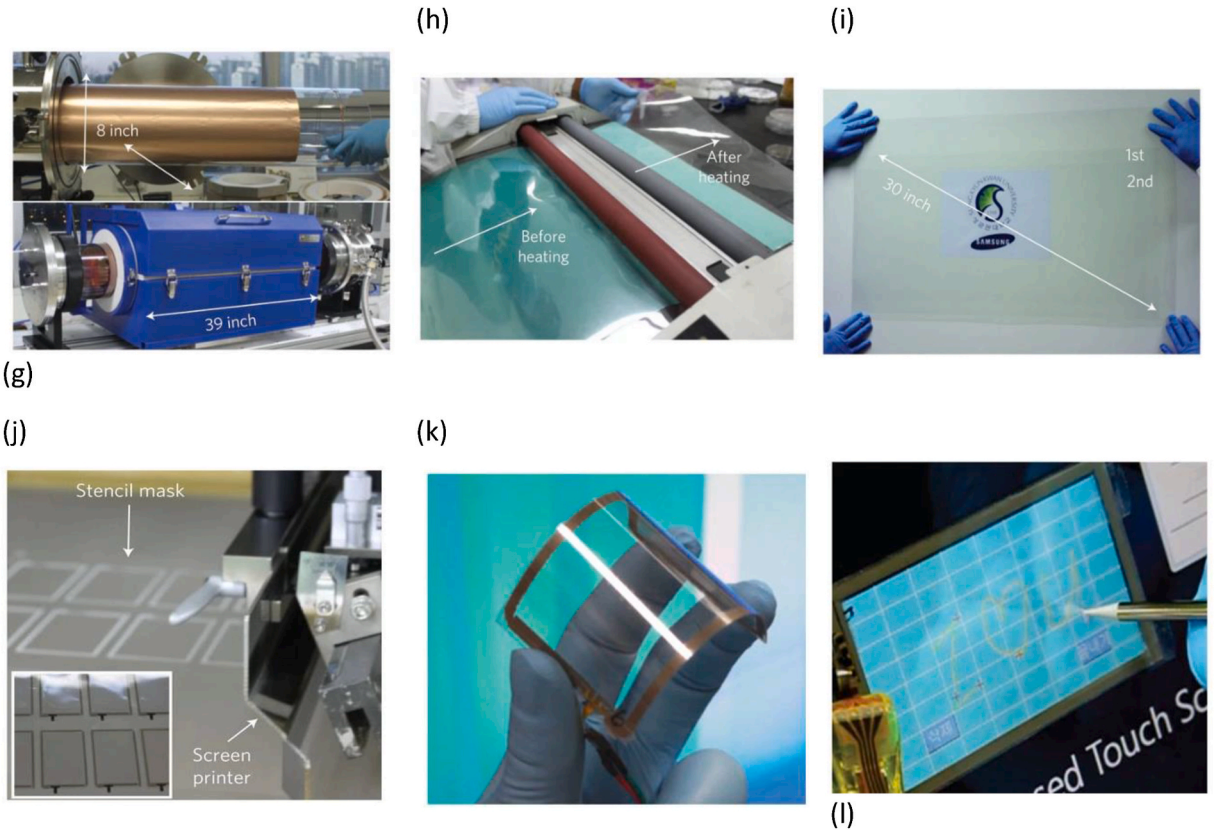

Fig. 4. (*continued*).

$\Omega\square^{-1}$ – 8.3 $k\Omega\square^{-1}$ at optical transmittance of 72 %–91 %, respectively. Flexible OPVs developed on CVD-graphene had a comparable PCE of 1.18 % to that of its ITO-counterpart (1.27 %). More importantly, the graphene-based flexible device revealed higher mechanical stability than that on ITO as shown in Fig. 4a–d. In addition, CVD-graphene, prepared on Cu foil at 1000 °C, was used as a top electrode for semi-transparent OPVs [107].

In contrast to other methods such as exfoliation, CVD possesses a high potential to produce large-area and high-quality graphene films for TCE applications. Following this approach, large-scale production of flexible graphene films has been reported by many researchers [108, 110,111]. Inspired by the method reported in Ref. [102], a SLG graphene film was synthesized on a 30-inch (in diagonal) flexible Cu substrate that was wrapped around a 7.5-inch quartz tube, inserted and suspended in an 8-inch quartz tubular CVD reactor to avoid non-uniformity in the graphene film as a result of a radial temperature gradient [110]. After thermal annealing of the flexible Cu foil under H_2 flow (for 30 min at 1000 °C) in order to increase its grain size for high quality graphene growth, a mixture of CH_4 and H_2 gases was applied into the reactor at 1000 °C for an additional 30 min.

More importantly, the continuous production of graphene has also been reported. For instance, a graphene film was grown on a 1 m long Cu foil using a R2R atmospheric pressure CVD reactor (Fig. 4e) [108]. However, the resulting film was found to be defective MLG, which may have been caused by graphene growth under atmospheric pressure at a high CH_4 concentration. Moreover, Kobayshi and colleagues [109] developed an approach to enable continuous R2R production of graphene on a suspended flexible Cu foil of 100 m length, in a low pressure CVD reactor via selective Joule heating of the Cu foil (Fig. 4f).

Despite the advances achieved in the development of high-quality and large area graphene films using thermal CVD, the resulting graphene has to be subsequently transferred from the Cu foil onto a transparent target substrate (PET, glass, etc.). These transfer procedures can lead to substantial damage to the graphene films. For example, R2R based thermal release tape (TRT) and wet transfer methods were used to transfer the graphene films reported in Ref. [110] from the Cu foil onto PET for developing an efficient and flexible touch screen (Fig. 4e–j). SLG transferred using the TRT method had an R_s of almost 270 $\Omega\square^{-1}$, while that from wet transfer had an R_s of 140 $\Omega\square^{-1}$. The higher R_s in case of R2R large-scale TRT graphene indicated damage to the transferred film. In comparison, the wet transfer is more complex, time-consuming and not scalable. Additional procedures such as doping can be utilized to enhance the properties of the transferred graphene films for TCE applications [109]. Thus, further limitations need to be overcome before commercializing these TCEs for optoelectronics. The major obstacles with this technology are its cost- and time-inefficiencies, the use of unsustainable and environmentally unfriendly carbon sources, and the complex transfer procedures to prevent possible damages to the graphene sheets. Therefore, different pathways to enable the transfer-free production of graphene, ranging from improving the transfer methods, doping strategies to the implementation of different types of plasma discharge, have been investigated.

4.2. Transfer methods of CVD-graphene

In order to best exploit the extraordinary electrical and optical properties of graphene for electronic and optoelectronic devices, graphene films need to be transferred onto different dielectric substrates. Thus, efficient transfer methods that can produce scalable and high-quality graphene films with minimum defects are inevitable for commercializing CVD-graphene electrodes. Several transfer methods have been developed to achieve this aim. In the following, a detailed discussion of the major methods including (1) wet, and (2) dry transfer will be presented.

4.2.1. Wet transfer

The wet transfer (WT) of CVD-graphene films from the metal substrates onto arbitrary substrates has received significant attention due to its ability to produce high quality SLG or MLG films. WT of graphene is based on the addition (often coating) of a support film (often polymer) on top of the graphene/metal (often Cu foil). Then, the resulting support layer/graphene/Cu is placed in a Cu etchant solution until the Cu foil is completely dissolved (typically hours). Subsequently, the support film/graphene is then transferred onto the target substrate and the support film is removed to release the transferred graphene on the target substrate. One of the most common wet transfer methods is the PMMA-mediated transfer method proposed by Jiao and co-workers [112]. In the PMMA-mediated WT method, a support layer (50–300 nm thick) is deposited on top of graphene/Cu substrate from a PMMA solution by spin coating. The resulting PMMA/graphene/Cu substrate is dried to remove any residual solution, is then placed in a Cu-etchant solution such as ammonium persulfate until the Cu is totally etched and this step is repeated in a fresh ammonium persulfate etchant. After that, the PMMA/graphene is well rinsed in isopropyl alcohol and then uploaded onto the target substrate (e.g. glass, PET, etc.). The PMMA/-graphene/target substrate is dried in a nitrogen flow and then thermally annealed on a hot plate at ~200 °C for a few minutes to increase the adhesion of graphene with the target substrate. Finally, the PMMA layer is dissolved by acetone leaving behind a graphene film on the target substrate for further applications (Fig. 5).

Although PMMA-transfer has been widely used, it has some limitations including the deterioration of graphene properties through mechanical damage and or PMMA residues. Due to the high growth temperature, the surface of the substrate can exhibit remarkable surface reconstructions resulting in a rough metal surface with the grown graphene following the metal surface underneath. Consequently, upon transfer onto the target substrate, the graphene film is not in a complete contact with the substrate and gaps can exist in between, leading to cracks and tears in graphene sheet during PMMA dissolving [113]. In order to make PMMA-mediated transfer of CVD-graphene more efficient, many efforts have been exerted to minimize cracks or tears in the resulting graphene films. For instance, Li and co-workers proposed a modified process through repeating the spin-coating step of PMMA on top of PMMA/graphene/target substrate, after etching Cu. This approach significantly improved the morphology and minimized the cracks of the transferred film compared to that transferred without repeated PMMA coating. The second PMMA facilitated the dissolution of the first PMMA support layer (because of drops of liquid PMMA during second coating) and improved the mechanical contact of the transferred graphene on the target substrate [113]. In the same regard, Her et al. [114] proposed a PMMA-mediated transfer with reduced residues using acetic acid instead of acetone to remove the PMMA support from the graphene surface. The implementation of UV irradiation has also shown good potential towards clean PMMA-based CVD-graphene transfer [115]. It was found that UV irradiation of the PMMA support layer under ambient conditions results in a degradation of the PMMA film through the cleavage of ester group side chains, which reduces the intermolecular interaction of PMMA with graphene underneath. The transfer process starts by spin coating a 50 nm PMMA film on graphene/Cu substrate, followed by UV (256 nm) irradiation for 30 min. Then, a 200 nm-thick PMMA layer is coated without further UV irradiation. After that, the Cu foil is chemically etched and the PMMA/PMMA (UV-treated)/graphene film is placed on the target arbitrary substrate, dried, and cleaned in a mixture of acetone: isopropyl alcohol: methyl isobutyl ketone (1:1:1 vol/vol) for 6 h. The graphene films transferred with the modified PMMA method exhibited higher carrier mobility compared to those transferred with the conventional PMMA method that entailed one PMMA film (200 nm) without UV irradiation and the PMMA was removed using acetone only. The improved properties suggested a more effective graphene transfer with minimum PMMA residues, which was confirmed by X-ray photoelectron spectroscopy (XPS) and contact angle measurements (Fig. 6). Another support film for CVD graphene transfer is based on thermal release tape (TRT) [110,116]. PET/Silicone double layer clean transfer was also reported [117].

Besides the possible damage of graphene films and chemical residues, PMMA-based WT has many challenges that reduce its effectiveness for scalable applications. These obstacles include the excessively long time, high cost, the heat treatment and complexity, which can dramatically impact the electrical and physical properties of the transferred film [118–120]. It is worth noticing that in the WT process, the Cu catalyst is not recyclable as it is dissolved in the etchant liquid (e.g. $FeCl_3$, ammonium persulfate, etc.), which increases the overall fabrication costs and generates chemical wastes for the CVD-graphene TCEs [121]. Therefore, the development of direct and dry transfer methods, which recycle Cu substrates for subsequent depositions, and avoid contaminating the transferred graphene by chemical residues, represents an attractive strategy towards time- and cost-effective CVD graphene TCEs.

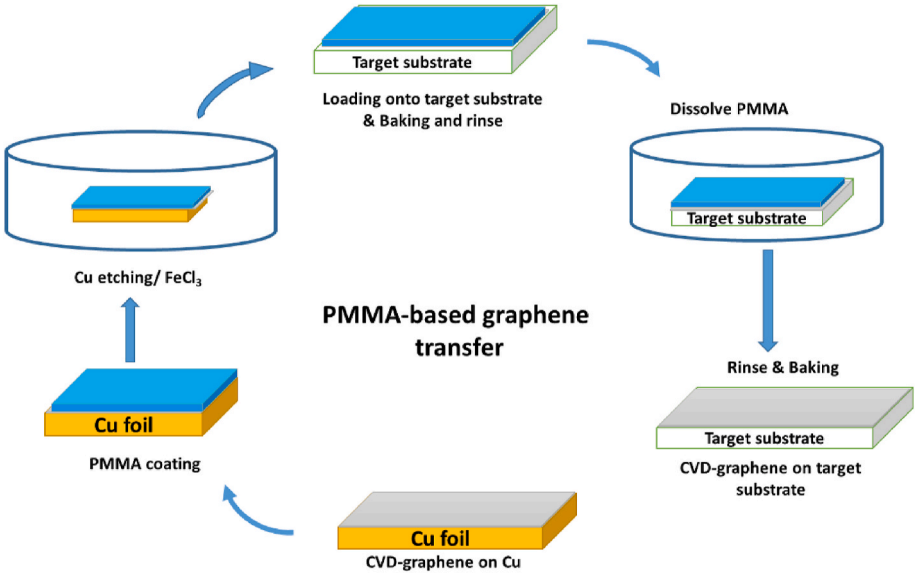

Fig. 5. Schematic illustration of the PMMA-based graphene transfer method.

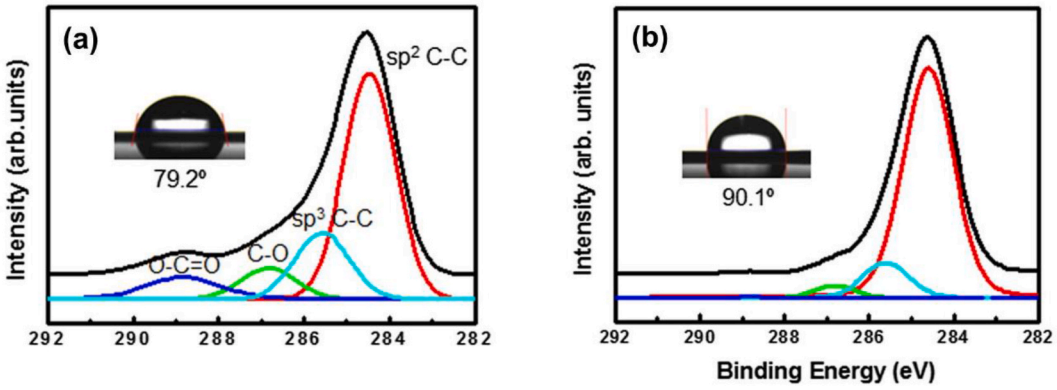

Fig. 6. XPS analysis, with peak deconvolution, of graphene transferred by (a) the conventional PMMA method and (b) the modified PMMA method. Insets illustrate water droplet contact angle, reproduced with a permission from ref. [115].

4.2.2. *Dry transfer*

Dry transfer methods of graphene onto the arbitrary dielectric substrates have been investigated to overcome the challenges associated with WT methods. For example, TRT-based methods were used to achieve a dry transfer of epitaxial graphene (E-Gr) from SiC substrate onto SiO_2/Si substrate [122]. In this approach, a thermal tape is placed directly on top of the E-Gr/SiC substrate and then a uniform mechanical pressure (3–6 N mm^{-2}) is applied to the top of the stack in an evacuated (4×10^{-4} Torr) bonding chamber for 5 min. Subsequently, the tape is peeled off from the stack removing most of the graphene from the surface of the SiC substrate. The peeled-off tape/E-Gr is then placed on the top of the target substrate and inserted into the bonding chamber again where the mechanical press step is repeated for another 5 min. Finally, the stack is thermally annealed on a hot surface at a temperature that 1–2 °C above the release temperature of the tape (120 °C) to remove the adhesion force between the tape and graphene. The tape is easily removed, and graphene is successfully transferred to the target substrate. An additional 10-min annealing step at ~250 °C was recommended to increase the adhesion of graphene with the substrate. It should be noted here that the cleaning and pre-treatment (by O_2 plasma) of the target substrate is crucial to get a uniform and high-quality transferred graphene film. However, the graphene surface on the growth substrate does not require special treatment procedures for effective transfer. The TRT method reported has been used successfully for CVD-graphene on Cu for TCE applications though further optimization for the transport procedure is necessary [122].

For a proper direct and large-area transfer of SLG prepared by CVD on Cu surface, Yoon and Shin et al. [121] measured the adhesion energy between graphene and the Cu substrate using double cantilever mechanics testing. The accurate measurement of this adhesion energy (0.72 ± 0.07 J m^{-2}) enabled them to use the proper type of adhesive material and the magnitude of force needed to exfoliate the SLG from the Cu substrate directly onto the target substrate. Moreover, an easy and time-effective dry transfer method using a commercial photograph laminator to transfer FLG onto flexible ethylene vinyl acetate (EVA)/PET substrate from Ni foil has been reported [123]. However, the transferred FLG on EVA/PET substrate exhibited low optical transmittance (~50 %) and large sheet resistance (Fig. 7a). This degradation of the optical and electrical properties of the transferred graphene was attributed to the random stacking of FLG on top of the laminating film, in contrast to that of the as-synthesized FLG on Ni film that showed continuous covering and well-ordered morphology with lower surface roughness (Fig. 7b–f). The poor, structural, optical and electrical features of such transferred films limit their applicability for optoelectronics.

A direct and renewable peel-off transfer of graphene grown on Cu foil was developed by Chen and colleagues [124]. Their approach utilized a thick (5 μm) polyimide (PI) polymer film, which served as both, a support film and a transparent flexible target substrate. The higher adhesion between the spin coated PI layer and the underlying graphene compared to that between graphene and Cu foil enabled the direct peel-off of freestanding graphene-PI flexible transparent conducting substrate. The proposed transfer method (Fig. 8) enables the reuse of Cu foil for CVD graphene growth, which makes it cost-effective and environmentally-friendly transfer approach. Nonetheless, the transferred graphene films had an R_s between 520 and 860 Ω $\square^{-1}$, which is much higher than that of ITO and graphene films transferred by more complex procedures as discussed earlier.

For a large-area transfer of CVD-graphene onto flexible substrates, R2R based transfer can be used similar to that employed in Ref. [110]. This approach starts with the adhesion of a support layer (polymer) via passing between two rollers to the graphene on Cu foil with the help of adhesive material. After that, the growth substrate (Cu) is removed through etching, followed by the transfer of the graphene/support layer onto a target substrate. Eventually, the support layer is released (Fig. 8b). If TRT is used as a support layer, it is removed by thermal annealing as discussed earlier. This approach included etching of the Cu foil, so it is not reusable for further depositions. However, using a TRT with a strong adhesion can help to avoid the etching step. Moreover, if a target flexible transparent substrate (PEN, PET) is utilized as a support film using a strong adhesive layer, this makes the process more practical due to the use of R2R large-scale transfer without dissolving Cu foil. Other strategies to exploit graphene in optoelectronic devices are based on growing CVD-graphene directly on dielectric substrates in order to avoid the complex transfer procedures as discussed in the following sections.

4.3. *CVD-graphene growth on dielectric substrates*

Despite the remarkable advancement in the transfer of the CVD-graphene, as discussed in the previous section, there are many limitations associated with the different transfer methods. These drawbacks include their high cost, time-demand, complexity, as well as the generation of chemical wastes and potential damage to the transferred graphene. Thus, instead of transferring CVD-graphene previously grown on a metal catalyst, the catalyst-free synthesis of graphene on dielectric substrates has been developed. One of the major obstacles for growing graphene on transparent dielectric substrates such as glass, PET, and PEN is, that these materials cannot resist the high temperature needed for graphene growth in a CVD reactor. The high temperature is needed for the decomposition of the carbon source vapor molecules (e.g. CH_4) and for the nucleation, and growth of graphene on the substrate surface. The application of various types of plasma discharge enables graphene growth at lower temperatures on a wide range of substrates including metals, semiconductors, and dielectrics. In 2008, Malesevic and colleagues reported the successful synthesis of FLG on different substrates

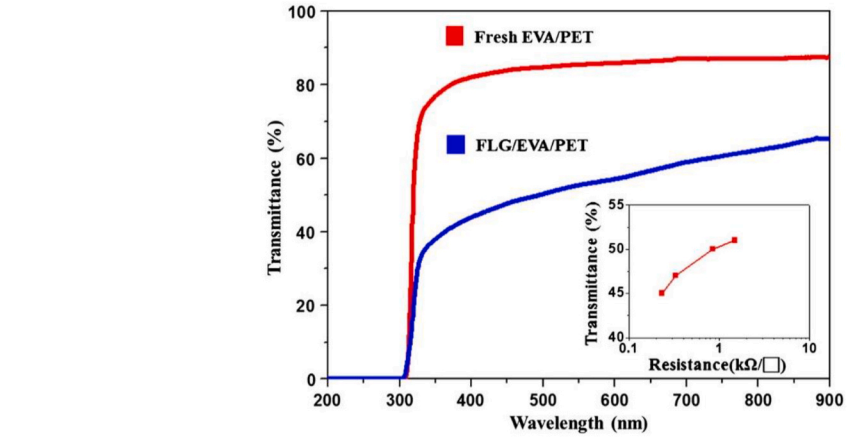

(a)

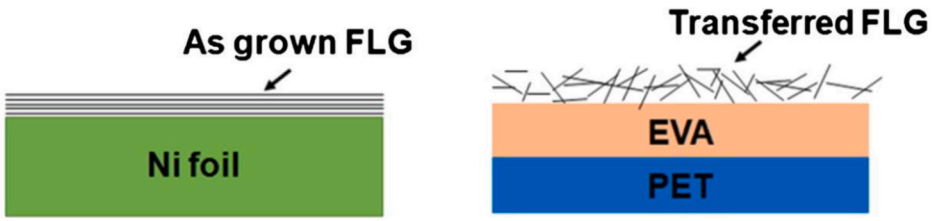

(b)

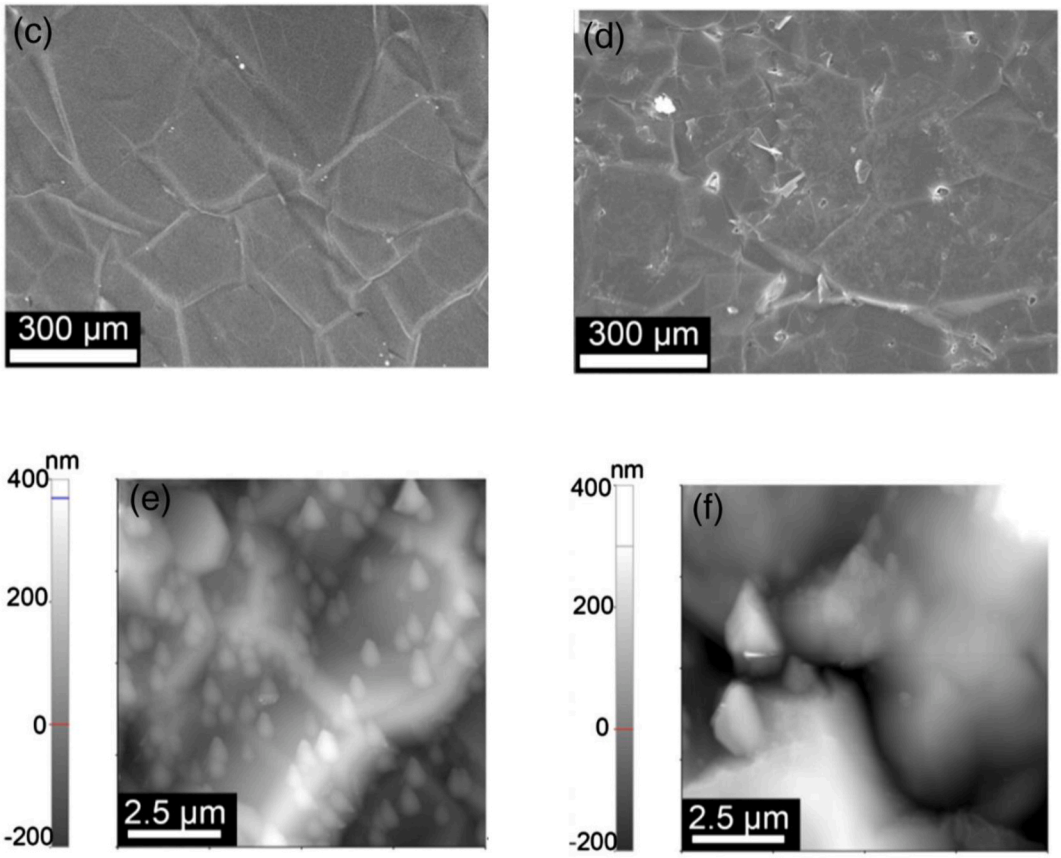

Fig. 7. (a) Transmittance of fresh EVA/PET and transferred FLG/EVA/PET substrates, the inset figure is the plot of sheet resistance versus transmittance at a 600 nm wavelength. (b) Schematic diagrams of the as-grown FLG on Ni foil and the transferred FLG/EVA/PET substrates. FE-SEM surface morphologies of the as-grown FLG on Ni foil (c) and the transferred FLG/EVA/PET substrate (d). AFM measurements of the as-grown FLG on Ni foil (e) and the transferred FLG/EVA/PET substrate (f). The RMS of (e) and (f) are 106 nm and 143 nm, respectively, adapted with a permission from ref. [123].

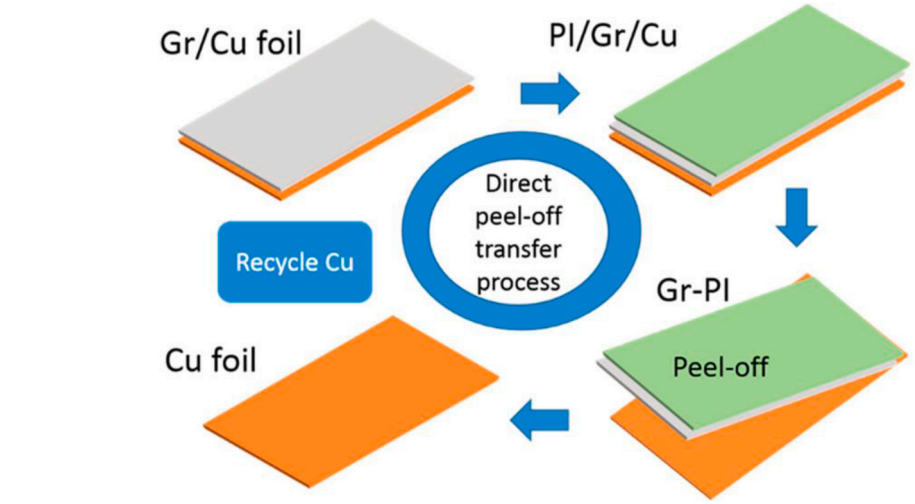

(a)

(b)

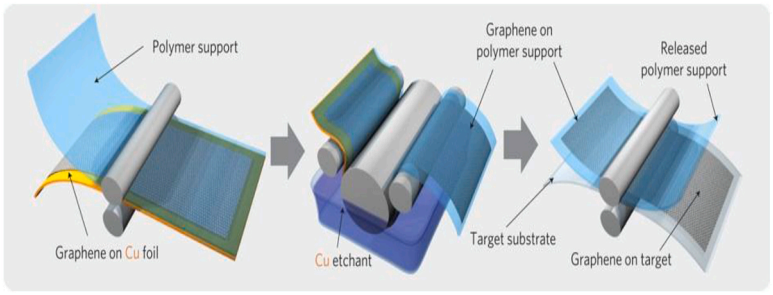

Fig. 8. (a) Steps of the etching-free Gr transfer process based on peel-off after deposition of Gr on a Cu substrate and solidification of a PI film, adapted with a permission from ref. [124]. (b) Schematic of the roll-based production of graphene films grown on a copper foil. The process includes adhesion of polymer supports, copper etching (rinsing) and dry transfer-printing on a target substrate. A wet-chemical doping can be carried out using a set-up similar to that used for etching. reproduced with a permission from ref. [110].

such as Ni, Si, quartz, Pt, and stainless steel using microwave (MW) plasma enhanced CVD at a threshold temperature of 700 °C without external heating [125]. The optimization of deposition parameters, e.g. MW power, deposition time, and the flow rate of the applied gases resulted in the formation of vertically oriented FLG flakes above a graphite layer that grew parallel to the substrate. Their approach paved the way towards low-temperature and catalyst-free production of CVD-graphene for electronics and optoelectronics applications. Lower synthesis temperatures (550 °C) were also reported using radio frequency (RF) from pure methane on dielectric substrates [126] and MW surface-wave (as low as 240 °C) [127] PECVD from C_2H_2/Ar mixture on Cu foil. However, the resulting graphene exhibited low quality, nano-scale lateral size, and poor electrical conductivity.

In addition to plasma implementation in CVD, other strategies were found to lower the synthesis temperature of CVD graphene. For instance, the utilization of solid-state PMMA film coated on Cu produced high quality graphene by thermal annealing at 800 °C in an Ar/H_2 atmosphere [128]. More progress has been reported in this aspect using liquid (C_6H_6) and solid (PMMA, and Ps) precursors in a split tube furnace (Fig. 9a) [81]. In this work, high-quality SLG was synthesized on Cu foil at 300 °C when benzene was used, while with solid precursor the quality and coverage of graphene varied significantly when deposition temperature dropped from 1000 °C to 400 °C (Fig. 9).

The low-temperature synthesis for high-quality graphene in case of C_6H_6 was attributed to the ring structure of benzene molecules, which resembles the hexagonal graphene lattice. Thus, it just required dehydrogenation and linking of benzene rings to form graphene. This explanation was supported by comparing the calculations of energy kinetics of the CVD process for C_6H_6 and CH_4 using density functional theory. The CVD mechanism was divided into three steps (1) collisions of the precursor molecules leading to adsorption on the Cu (111) surface, backscatter to the gas phase, or proceeding to the next step where the molecules partly or totally dehydrogenate to form active surface species, which finally nucleate and grow graphene sheets. The calculations revealed both precursors have low adsorption energy of 0.09 eV and 0.02 eV for C_6H_6 and CH_4, respectively. The higher the adsorption energy, the more relevant the trapping-mediated reactions are. Thus, C_6H_6 may show a slight tendency for graphene growth at lower temperature as the activation energy of trapping-mediated reaction is typically lower than that of the direct counterpart [129]. For the dehydrogenation step, the activation energy for C_6H_6 was found to be 1.47 eV, while that for CH_4 was 1.77 eV. For smaller gas molecules to become active for nucleation, they need to lose more than one H atom per carbon, i.e., the dehydrogenation barrier for methane is higher. Finally, the planar ring-structure of C_6H_6 molecules resulted in a lower nucleation barrier if compared to CH_4. Despite the successful growth of graphene at low temperatures with C_6H_6 and CH_4, it should be noted that the Cu foil had to be initially annealed at 1000 °C for 20 min in a 100 sccm H_2 flow, and then cooled down to the desired temperature prior to graphene synthesis. Thus, from an economical perspective, the cost of graphene synthesis in Ref. [81] is still high. In addition, further procedures are required to transfer the resulting graphene from Cu to the transparent substrate for TCE applications.

Although PECVD system facilitates the growth of graphene at lower

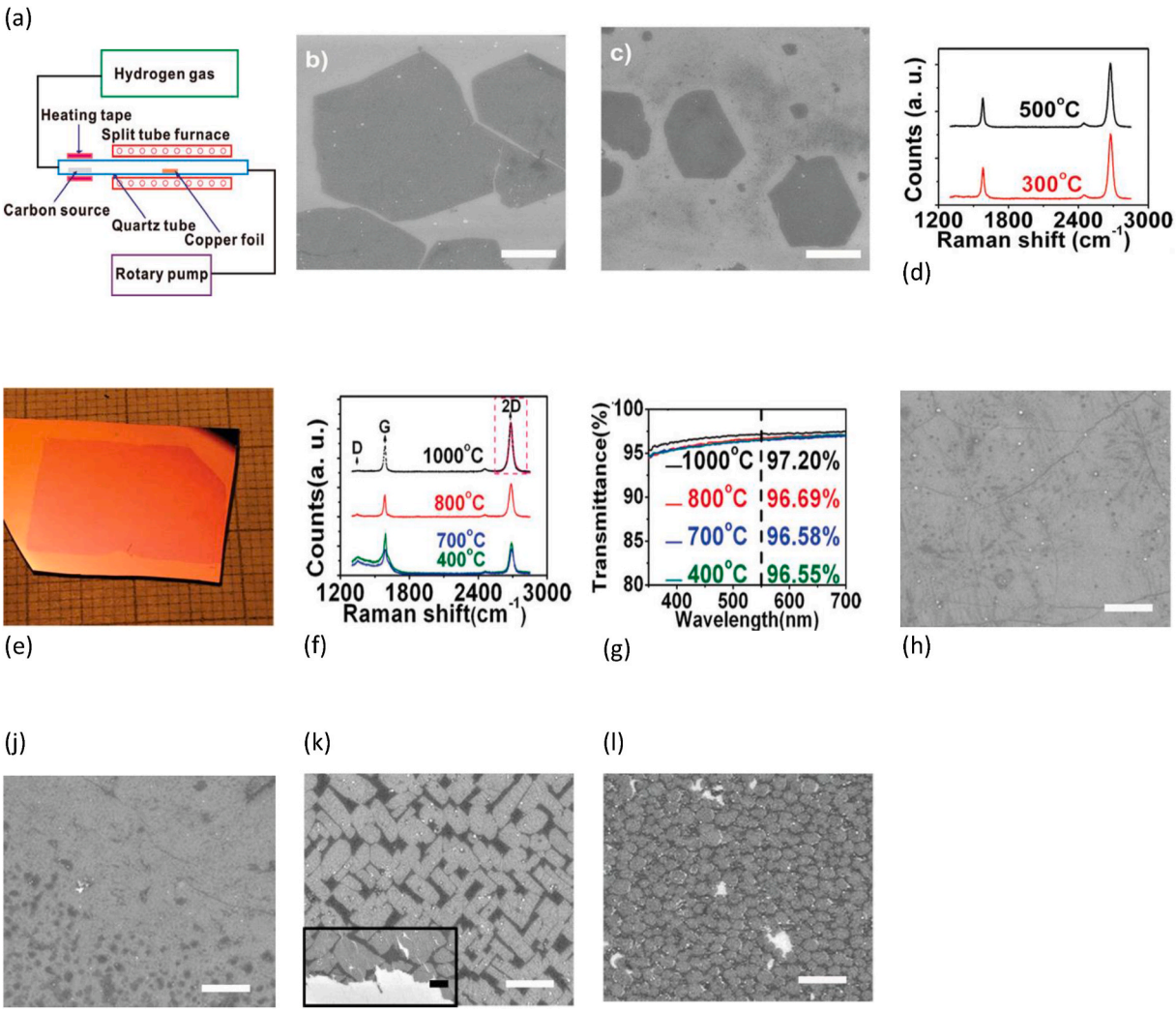

Fig. 9. (a) Schematic of the CVD growth from solid carbon sources on Cu foils. Benzene derived graphene (b–d). (a) Raman spectra of graphene grown at 500 and 300 °C, respectively. (c and d) SEM images of graphene grown at 500 and 300 °C, respectively. Scale bars are 2 μm (c and d). d) [81]. PMMA derived graphene (e–l). (e) Photograph of graphene grown at 1000 °C and transferred to the SiO_2/Si substrate. (f) Raman spectra of graphene grown at 1000, 800, 700, and 400 °C, respectively. (g) Optical transmittance spectra of graphene grown at 1000, 800, 700, and 400 °C, respectively. The transmittances of light at 550 nm for different growth temperatures are also indicated in panel g. (h–l) Typical SEM images of graphene grown at 1000, 800, 700, and 400 °C, respectively. The inset of panel f is an SEM image showing the sharp edge of graphene on the SiO_2/Si substrate. The scale bars are 2 μm (h−l, inset of k). Images were reproduced with a permission from ref. [81].

temperatures, the energetic particles generated by plasma discharge can cause structural defects within the graphene lattice [130]. The presence of such imperfections is always indicated by the D-peak in the Raman spectrum of graphene. Based on the Raman spectra for graphene films deposited using MW [127] or RF [126] PECVD on different substrates including Cu and dielectric substrates, the presence of a strong D-peak can be noticed (Fig. 10), indicating larger structural defects. In contrast, high-quality graphene with low defect density (minimal D-peak) was also reported by Chan et al. using a DC plasma assisted CVD reactor at 600 °C on Cu foil as shown in Fig. 10d [131].

By comparing the experimental setups used in these three publications [126,127,131], it may be concluded that the low-defect structure in case of ref. [131] is attributed to the application of plasma discharge outside the hot zone where graphene deposition occurs. This configuration may assist in reducing the bombardment and collisions between plasma ions and active radicals with the synthesized graphene lattice in contrast to that in Refs. [126,127], where the substrate is installed in the center of the glowing discharge (Fig. 10e–g).

Graphene growth on glass substrates can be remarkably enhanced in the presence of a Cu catalyst in a PECVD system. For instance, VG nanosheets were obtained on commercial glass substrates at 500 °C using Cu-assisted PECVD [132]. Similarly, direct growth of VG on various flexible glass substrates was achieved at temperatures (500–750 °C) in a Cu-foam assisted PECVD reactor [53]. However, the resulting VG nanosheets exhibited high defect density and high sheet resistance in both cases. The vertical orientation of graphene nanosheets is favorable in a PECVD, while in thermal CVD only horizontal growth is observed on different substrates such as metals [85], and dielectric substrates [132]. The growth and the properties of VG can be controlled and tuned by controlling the deposition parameters such as growth time, precursor type, flow rates of the precursor and the carrier gas, substrate type, plasma power, and deposition temperature. For TCE applications for OPVs or other optoelectronics, three main properties of the graphene film can determine its suitability: (1) sheet resistance, (2) optical transmittance, and (3) surface morphology. An efficient graphene TCE should possess low sheet resistance, high optical transmittance, and low surface roughness. The growth of vertical graphene nanosheets can result in a dramatic drop in the film's transparency with significant increase in film roughness. A highly rough surface of a TCE material in OPVs increases the recombination of the photo-generated charge

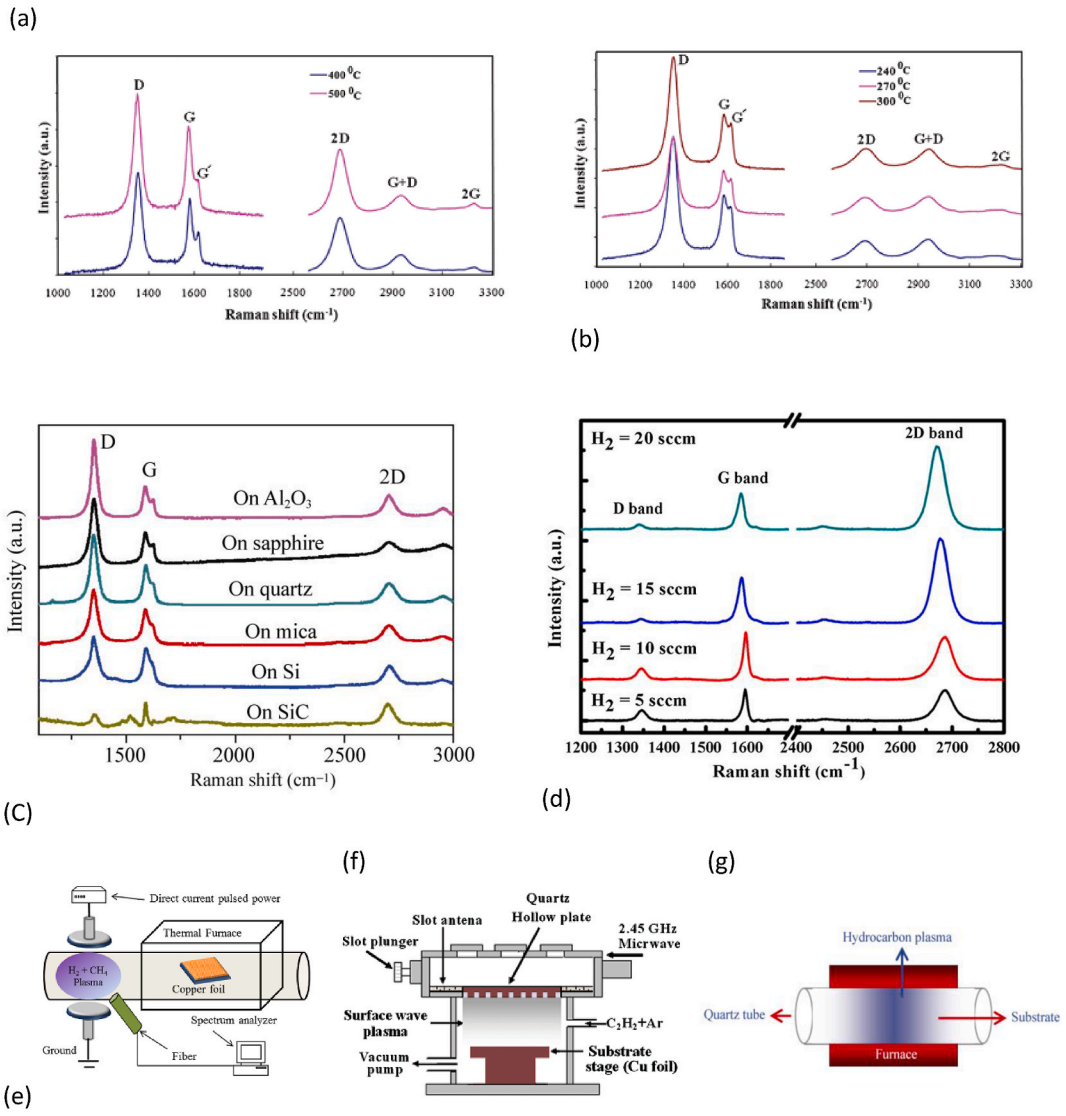

Fig. 10. a) Raman spectra of a graphene film deposited at a substrate temperature of 400 and 500 °C. b) Raman spectra of a graphene film deposited at a substrate temperature of 240, 270 and 300 °C, indicating the presence of 2D peak and formation of a few layers of graphene [127]. c) Raman spectra of nanographene films grown on various substrates [126]. d) Raman spectra of graphene films that were transferred from copper foil to the SiO_2/Si substrate. Samples were synthesized at 600 °C by plasma-assisted thermal CVD using various H_2 flow rates from 5 to 20 sccm for 5 min [131]. (e–g) Schematic illustration of the PECVD setup for graphene film growth in ref. [131] (e), ref. [127] (f), and ref. [126] (g). Images were adapted with permissions from ref. [126,127,131]

carriers and reduces R_{sh} via increasing leakage pathways of photocurrent leading to a dramatic drop in the *FF*, V_{OC} and PCE of the device [133]. Therefore, the height and density of VG nanosheets should be controlled during the synthesis of graphene on transparent substrate in a PECVD system so that the resulting film meets the requirements for an efficient TCE. In addition, further optimization should be conducted so that the in-plane layer can form a high-quality graphene rather than amorphous carbon or graphite. This can help to avoid the formation of rough-surfaces and low-transparency graphene films.

PECVD techniques have enabled graphene synthesis at lower temperatures on different substrates as discussed before. However, the high quality PECVD graphene was grown on metal substrates (mainly Cu) and in some cases the Cu foil required pre-treatment at 1000 °C for 20 min prior to graphene synthesis at lower temperatures [81]. In case of low-temperature PECVD graphene on dielectric substrates such as glass or quartz, the quality of graphene was not adequate to make it a competing TCE candidate for OPVs. The low quality of graphene can be due to non-uniformity, discontinuity, and the presence of defects such as vacancies, voids, dislocations, and grain boundaries, which are high-likely to occur in a typical low-temperature PECVD system on dielectric substrates because of the collisions of energetic ions and radicals with graphene film. These factors cause the properties of the resulting films to deviate from the intrinsic properties of graphene. Consequently, further procedures are required to enhance the properties of the resulting PECVD graphene.

4.4. *Transfer-free CVD-graphene TCEs*

The following section will focus on research efforts towards efficient transfer-free CVD-graphene TCEs. Despite all the progress achieved in the production of high-quality CVD graphene, a few reports can be found on the graphene TCEs produced by single-step procedures. An efficient single-step procedure can produce a high-quality, uniform, and large-area graphene film directly on the transparent glass or flexible substrate with proper electrical and optical properties for TCE applications. In a conventional CVD reactor, the growth of graphene sheets is achieved on the surface of the metal catalyst such as Cu or Ni then the resulting film is transferred onto the transparent substrate, as discussed

earlier. Thus, the utilization of the metal catalyst is crucial for obtaining a high-quality graphene film with minimum defects. One of the major challenges for PECVD-graphene on dielectric substrates is the high density of structural defects within graphene lattice such dislocations, grain boundaries, voids, etc. Consequently, the directly-synthesized PECVD-graphene exhibit a high sheet resistance which hinders its implementation as efficient TCE candidate. Thus, the production of efficient and scalable CVD-graphene TCEs requires innovative approaches which can result in defect- and transfer-free graphene growth. For example, Byun et al. proposed an approach to synthesize CVD-graphene directly on Si/SiO_2 from solution-processed polymers [134]. Their strategy relied on spin coating a thin layer (10 nm) of a commercial polymer such as PMMA, PS, and polyacrylonitrile (PAN) on the Si/SiO_2 substrate then depositing a thin (up to 100 nm) Ni capping layer. Subsequently, the pyrolysis of the polymer film (carbon source) under the metal capping at 1000 °C in an inert atmosphere resulted in FLG film on the Si/SiO_2 substrate (Fig. 11a& b) after etching the metal capping in a 1 M $FeCl_3$ aqueous solution. The metal capping layer was found to play two crucial roles in graphene synthesis (1) it prevents the evaporation of the carbon source, (2) it acts as a catalyst for the growth of graphene. Despite the transfer-free growth of CVD-graphene by the approach proposed in Ref. [134], it required high synthesis temperature. More critically, the precipitation of carbon from Ni during cooling down makes it difficult to get uniform graphene films as explained earlier. To improve this approach, Zhou and co-workers used polycyclic aromatic hydrocarbons (PAHs) as carbon source and Cu capping film [135]. They successfully obtained large-area graphene films on dielectric substrates such as Si/SiO_2, quartz and glass at lower temperatures (600 °C). A thin layer of the PAH precursor was first deposited on the dielectric substrate via thermal evaporation, followed by the deposition a Cu layer (within 200 nm thick) on the PAH film by e-beam evaporation and then heated (at 600–1000 °C) in the CVD reactor. Finally, the top Cu catalyst layer was etched using Marble's reagent ($CuSO_4/HCl/H_2O$ = 10 g/50 ml/50 ml) (Fig. 11c). The thickness of Cu capping layer had a significant effect on the formation and quality of the resulting graphene film as shown in Fig. 11d. The optimum Cu thickness for graphene growth was found to be 200 nm. Thinner Cu films (<50 nm) did not produce graphene due to the agglomeration and partial evaporation of Cu film during the growth process. Thicker Cu (>200 nm) films did not affect the quality of the synthesized graphene. Oppositely, the quality of the graphene films dropped significantly with increasing the thickness of the polymer film from 5 to 20 nm (Fig. 11e). The graphene quality showed a remarkable enhancement with increasing the growth temperature; however, graphene films were obtained at 600 °C (Fig. 11f). In addition, the use of H_2 gas during graphene synthesis increased the defect concentration within the resulting graphene film (Fig. 11g) as a result of its etching impact. The sheet resistances of the resulting graphene films ranged from 550 to 850 $\Omega\square^{-1}$ when the synthesis temperature dropped from 800 °C (quartz) to 600 °C (glass). The synthesized graphene films showed a good potential as a TCE for OLEDs.

Another promising approach to synthesize high-quality and defect-free graphene at 150 °C using a two-stage CVD apparatus was developed by Park et al. [136]. They managed to prepare SLG graphene with high optical transmittance of 97.5 % and an R_s of 618 ± 15 $\Omega\square^{-1}$ on flexible substrates. Their approach was based on the introduction of a thin layer of titanium (Ti) on the growth substrate prior to graphene synthesis, because Ti possesses a high affinity to carbon. The process starts with the deposition of 10-nm thick Ti film by DC sputtering under 0.4 Pa and 20 W for 3 min. Upon the exposure of the Ti-coated substrate to ambient atmosphere, the Ti layer oxidizes into TiO_2, so a reduction step is essential prior to graphene synthesis. The TiO_2-coated substrate is annealed under H_2 atmosphere for 1–4 h to restore the Ti layer (Fig. 12). The configuration of the experimental setup used in that work consisted of two zones; one is kept at a high temperature and the other is at lower temperature to avoid melting of the substrate. After that, the carbon source (CH_4/H_2) is allowed to enter the reaction chamber to form graphene on reduced TiO_2-coated substrate.

The resulting graphene films have shown defect-free structure with their quality and area increased with increasing the reduction time as shown in Fig. 12c–f. However, it should be noted that this method still requires high temperatures of 750 °C and 1100 °C for TiO_2 reduction and the decomposition of CH_4 for graphene growth, respectively.

In 2019, Tran and colleagues made use of the approach reported in Ref. [136] to develop highly flexible graphene TCEs for

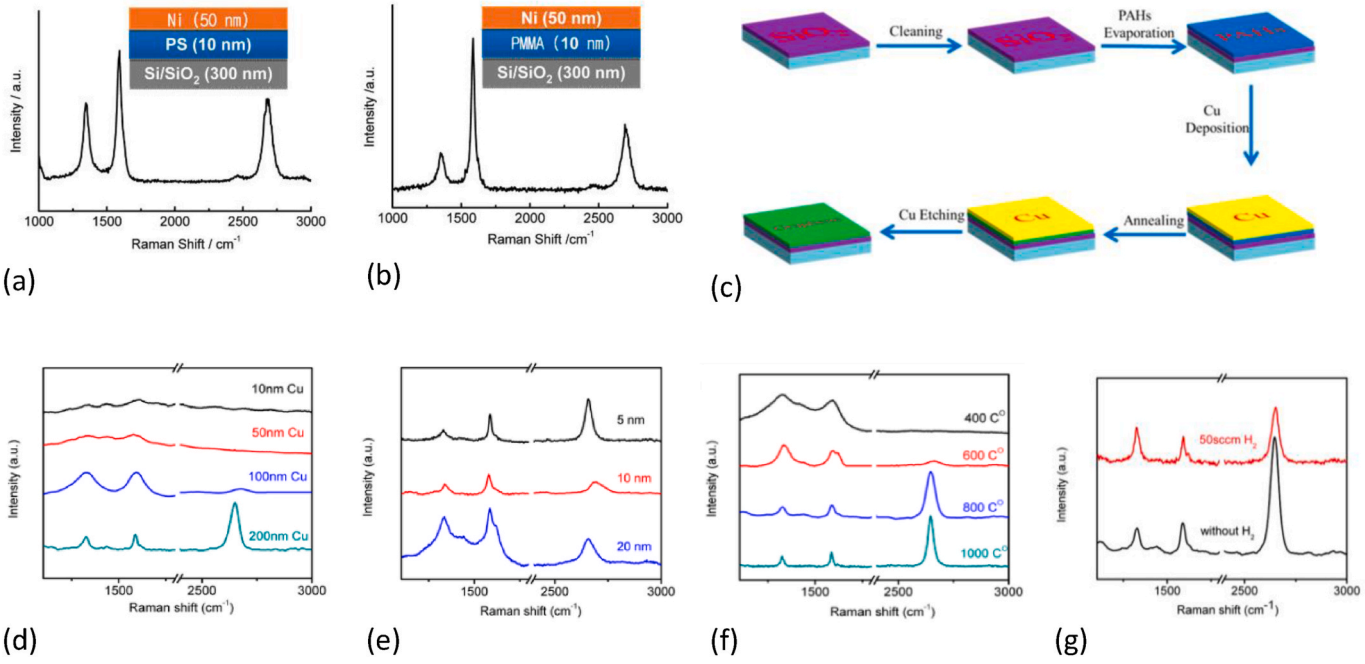

Fig. 11. Raman spectra for the directly synthesized CVD graphene films using different solid carbon sources (a & b) [134]. (c) A schematic illustration to the transfer-free CVD growth of graphene reported in Ref. [135]. (d–f) Raman spectra for graphene films grown under different Cu thickness (a), polymer layer thickness (b), temperatures (c), and H_2 flow [135]. Images were adapted with permission from references [134,135]

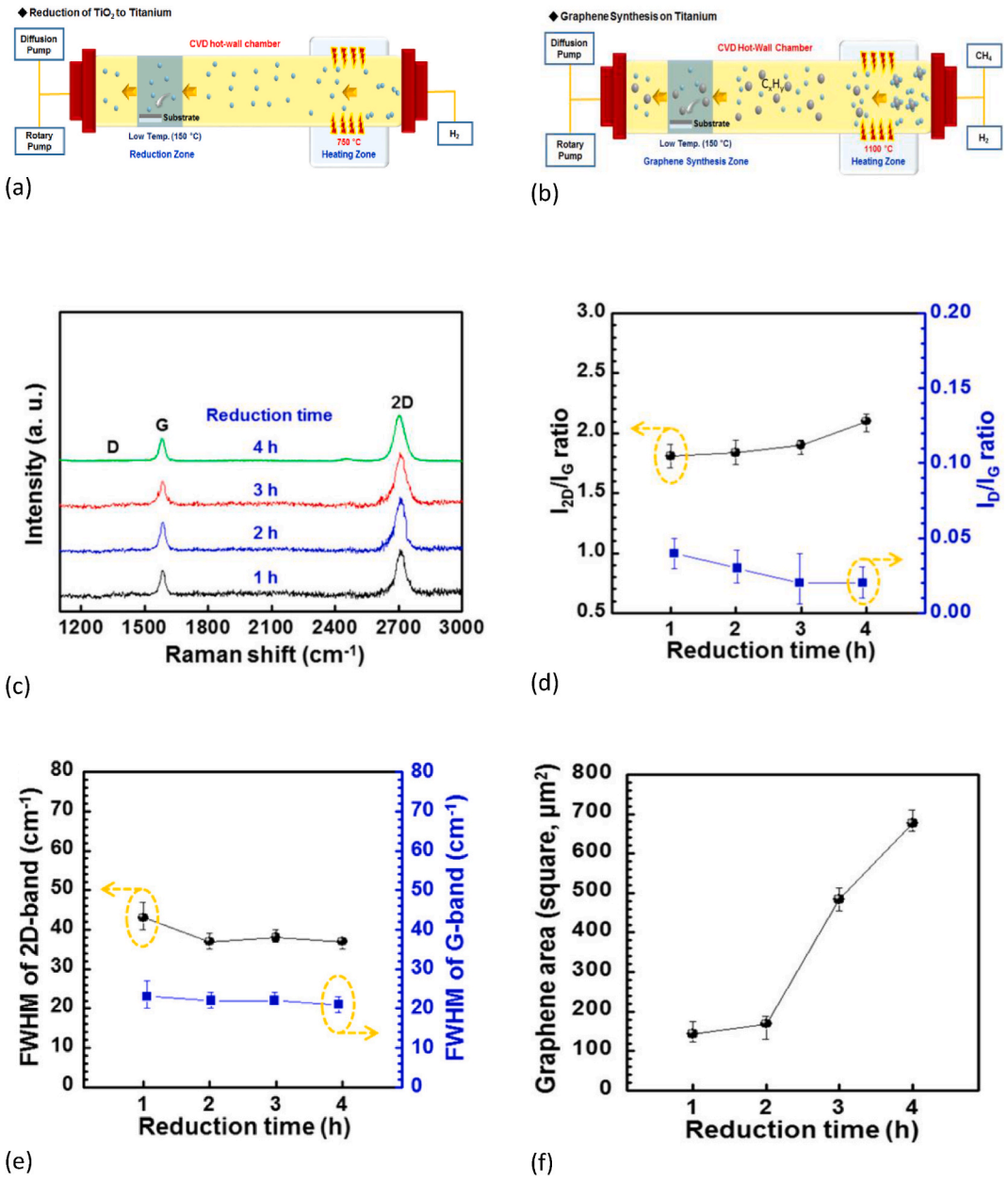

Fig. 12. (a) Schematic of the CVD chamber for reduction of TiO_2 to titanium at 150 °C. (b) Schematic of the CVD chamber for graphene synthesis at 150 °C on reduced titanium-coated substrates. (c) Raman spectra of graphene synthesized at 150 °C on a 10 nm thick Ti layer reduced for different reduction times under hydrogen. (d, e) I_{2D}/I_G and I_D/I_G intensity ratio and fwhm of 2D- and G-bands of graphene synthesized at 150 °C on Ti reduced for different reduction times under hydrogen. (f) Area of graphene synthesized at 150 °C on Ti reduced for different reduction times under hydrogen. Images were reproduced with a permission from ref. [136].

semi-transparent and super-flexible perovskite solar cells [54]. They integrated the DC sputtering system (needed to deposit 10-nm Ti layer prior to graphene synthesis) with the plasma assisted thermal CVD (PATCVD) unit in a single apparatus as shown in Fig. 13a. The directly synthesized graphene was compared to a PMMA-mediated transferred graphene prepared by CVD on Cu foil at 950 °C as shown in Fig. 13b–f. Consequently, the time-consuming and expensive reduction step of TiO_2 can be avoided using the new setup. Graphene synthesis was conducted following the DC sputtering of the Ti (10 nm) film on the flexible polymer substrate; polystyrene (PES) at 150 °C. The sputtering was performed at 25 W using DC power, a gas flow rate of 10/10 sccm Ar/H_2 and at working pressure of 0.7 Pa for 10 min at a 10 cm distance between the PES substrate and the target. Then, graphene synthesis was carried out using PATCVD at a temperature of 150 °C, a working pressure of 0.24 kPa and with gas (H_2:CH_4: Ar) flow rates of 3:10:12 sccm for 90 min.

A pair of plasma guns separated by 8 cm and positioned 10 cm apart from the Ti-coated PES substrate were used for the decomposition of the CH_4 precursor at a RF power of 80 W. However, no estimation to the temperature in the plasma discharge was provided. The transfer-free PATCVD graphene film revealed higher electrical conductivity and optical transmittance than the PMMA-transferred CVD counterpart as shown in Fig. 13 c &d. PATCVD-graphene had an R_s of 82 Ω □$^{-1}$, much lower than that of the transferred graphene (2011 Ω □$^{-1}$), which clearly reveals the impact of transfer procedures on the graphene properties and highlights the need for transfer-free synthesis procedure for graphene TCEs in optoelectronics. More crucially, the transfer-free graphene TCE-based perovskite solar cell showed a maximum PCE of 14.18 % with a *FF*

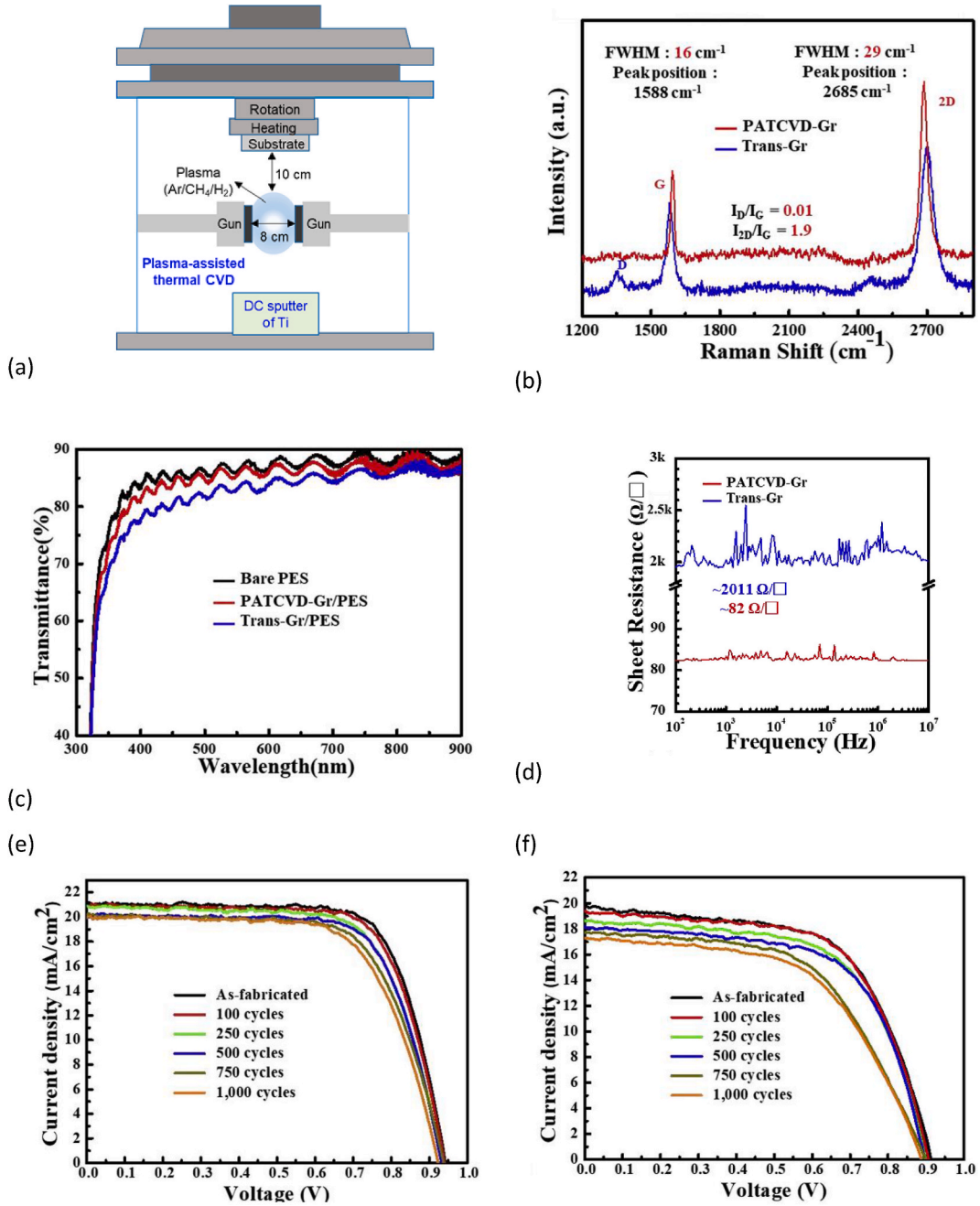

Fig. 13. (a) Schematic diagram of the PATCVD system for *in-situ* graphene synthesis at low temperature. Ti (10 nm)-buffer layer was deposited via dc sputter at 150 °C. Plasma guns for PATCVD were moved toward left and right sides for Ti-deposition via dc sputter. (b) Raman spectra of PATCVD-Gr and *Trans*-Gr. PATCVD-Gr showed no defects compared with defects of *Trans*-Gr. (c) Transmittance of PATCVD-Gr and *Trans*-Gr with bare PES as a reference. (d) Sheet resistance of PATCVD-Gr and *Trans*-Gr as a function of applied frequency via the Z-theta method. Sheet resistance of PATCVD-Gr is as low as ~82 Ω/□. (e) and (f) The J-V characteristics of the PATCVD-Gr and *Trans*-Gr devices, respectively, as a function of bending cycle under a tensile strain of 1.5 %. Images were adapted with a permission from ref. [54].

of 0.73, while the device based on the transferred graphene TCE exhibited a maximum PCE of 12.65 % and a *FF* of 0.65, respectively. Although the performance of the device on transferred graphene lagged behind that of the transfer-free graphene TCE as a result of the high R_s, it exhibited reasonable photovoltaic parameters given the large difference between R_s of both graphene TCEs. Furthermore, the PATCVD-graphene based perovskite solar cell showed a great level of flexibility by retaining more than 90 % of its initial PCE after 1000 binding cycles at 1.5 % tensile strain with 4 mm equivalent radii (Fig. 13e and f).

In spite of the advancement achieved in terms of the economic aspect [52,54,136], all of them required relatively long reaction times of 2–3 h and used an environmentally-hazardous and unsustainable carbon source (methane), and carrier gases. Furthermore, the deposition of additional metal thin films on the transparent insulating substrate [136, 137] prior to the CVD process increases the overall expense and complexity of the synthesis procedure. Also, in some cases [53], the directly-synthesized graphene films exhibited high I_D/I_G ratios of 1.4–1.6 and hence high defect concentrations. Therefore, further procedures are necessary to enhance the properties of the as-prepared graphene to be suitable for TCE applications. In this context, Kamel et al. reported a rapid and transfer-free production of graphene on commercial glass from a cheap, environmentally-friendly, and sustainable liquid carbon source, i.e. plant extract, using RF-PECVD [14]. This approach facilitated a time- and cost-effective preparation of large-area

graphene films without carrier gas or catalyst through a 2-min reaction at 600 °C. The as-synthesized films showed uniform coverage to the glass with high optical transmittance, medium sheet resistance, and had I_D/I_G ratio of 0.72. Controlling the growth of vertical nano sheets resulted in uniform graphene films with good optical transmittance (65–81 %) and medium sheet resistance (0.9–1.6 kΩ $\square^{-1}$). Consequently, inverted geometry OPV devices based on the as-synthesized graphene TCEs have shown a comparable photovoltaic performance to that of ITO. The fabricated graphene-based device had higher J_{SC} and V_{OC}, resulting in achieving 78 % and 80 % of the *FF* and PCE of the control (ITO-based) device (Fig. 14). However, further enhancement to the electrical properties of the transfer-free graphene is needed to make it more competitive to ITO. Several strategies have been proposed over the past years to improve the features of graphene TCEs such as doping and hybridization with silver nanowires (AgNWs), which will be discussed in the following sections.

4.5. Doped CVD-graphene

One of the challenges of directly synthesized CVD graphene TCEs is to achieve low levels of sheet resistance at high optical transmittance. Consequently, doping is an effective approach to enhance the conductivity of graphene via increasing carrier density [138]. Graphene doping can be achieved in different pathways including adsorption of molecules and atoms [139,140], substitution of atoms within the lattice [141,142], and functionalization [143]. The doping of graphene helps tune its work

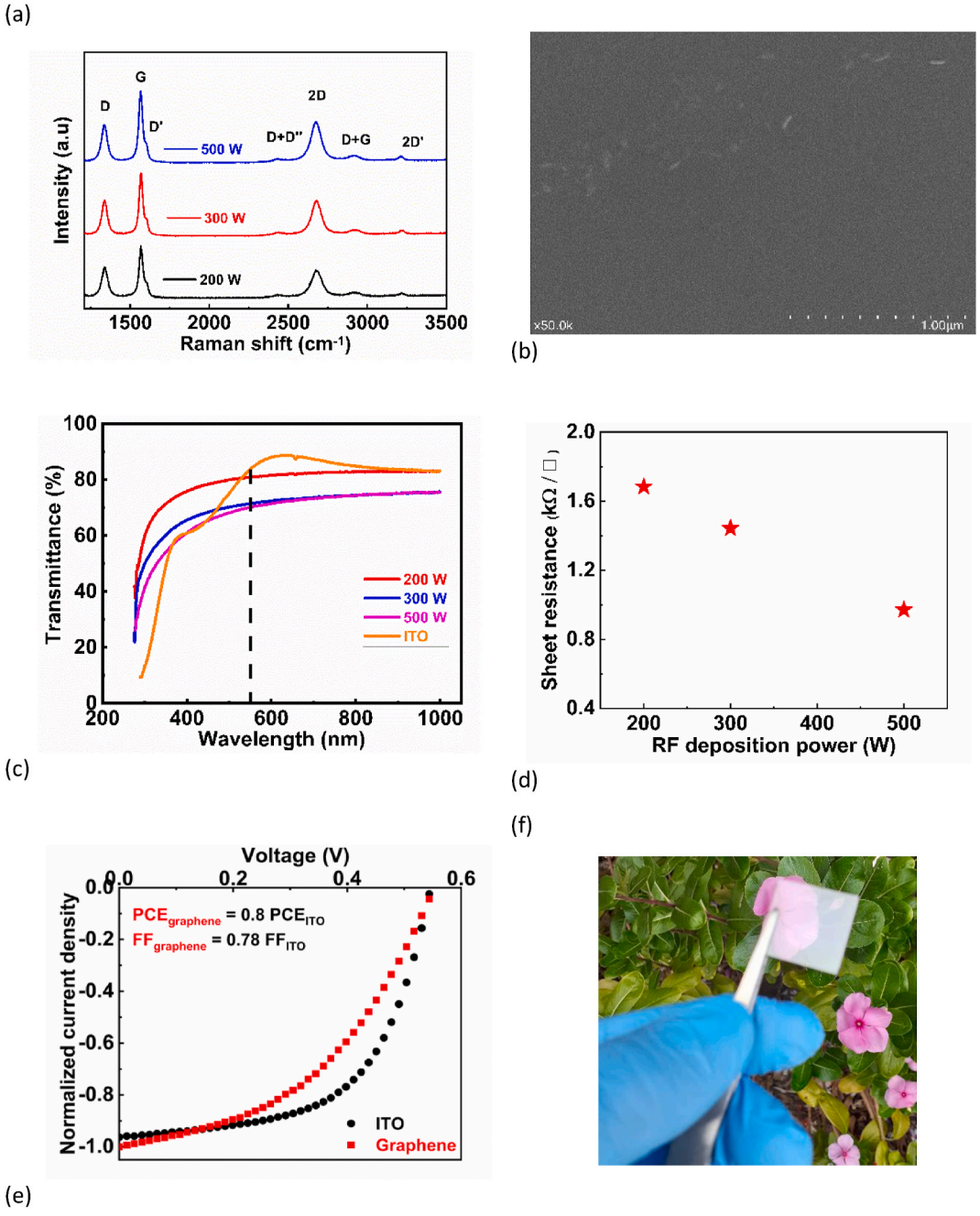

Fig. 14. a) Raman spectra for graphene samples prepared at various RF input power levels. b) SEM images for graphene films prepared at 200 W. c) Optical transmittance of the different graphene electrodes measured by a J. Woollam Ellipsometer. d) The variation of the sheet resistance of the synthesized graphene TCEs with RF input power. f) Typical image to the synthesized graphene TCE. Images were reproduced with a permission from ref. [14].

function (WF), wettability, and R_s to become more suitable TCE candidate for optoelectronics. Graphene doping can be achieved via a direct growth process, which results in a doped-graphene structure (e.g. Nitrogen-doped graphene) or through a post-treatment method. Post-treatment methods can be divided into (1) dry, and (2) wet processes. A dry post-treatment includes plasma, thermal treatment, electrostatic field, and evaporation methods. Conversely, wet doping post-treatment of graphene includes the usage of strong acids, metal chlorides, and polar organic molecules via solution processing methods such as spin and dip coating. In the following sections, a brief overview of the main doping routes of CVD-graphene as well as the progress achieved in device performance of doped-graphene TCEs is given.

4.5.1. Direct doping

The direct doping of CVD-graphene is achieved during the growth process using precursors containing the hetero dopant element to be impeded within the graphene lattice. For instance, the direct synthesis of *N*-doped graphene has been widely reported using different precursors such as carbon source and nitrogen-containing gas mixtures [141,144]. The precursor molecules decompose and recombine resulting in a doped graphene sheet on the substrate surface. The direct doping of graphene includes the substitution of carbon atoms by the dopant atom. The most common forms of direct doping of graphene are nitrogen- and boron-doped graphene leading to n-type and p-type doped graphene, respectively. The electronic and electrical properties of the resulting doped graphene differ from that of the pristine graphene and depend on the level of doping, which can be controlled via adjusting the ratio of the components within precursor mixture. The direct synthesis of *N*-doped graphene was first reported by Wei et al. using CVD [141]. They used a mixture of CH_4 and NH_3 to grow *N*-doped graphene (Fig. 15) at 800 °C on a 25 nm thick Cu film coated on Si substrate. The nitrogen doping was confirmed by XPS and Raman data. More interestingly, the doped film revealed n-type semiconductor behaviour, which affirms the tunability of graphene properties by direct doping.

Directly-doped graphene films grown by CVD on metal catalysts may not be the best choice for TCE applications as they still need to be transferred onto transparent substrates, which can result in substantial damage to the transferred films as discussed earlier. To avoid the film transfer, the direct growth of *N*-doped graphene films on dielectric substrates such as Si/SiO_2, quartz and glass was also reported by Zhou et al. in Ref. [135]. *N*-doped graphene was obtained by the same method through the *N*-containing carbon source. The doping percentage within graphene films was found to depend on the *N*-content in the precursor. Thus, using a proper carbon source and optimizing the deposition parameters can result in transfer-free CVD graphene with different dopant atoms.

4.5.2. Post-treatment doping

4.5.2.1. Dry methods. The main objective of the dry post-treatment of CVD-graphene is to tune the WF of graphene in order to make it more suitable for device fabrication purposes. The first layer on the TCE in an

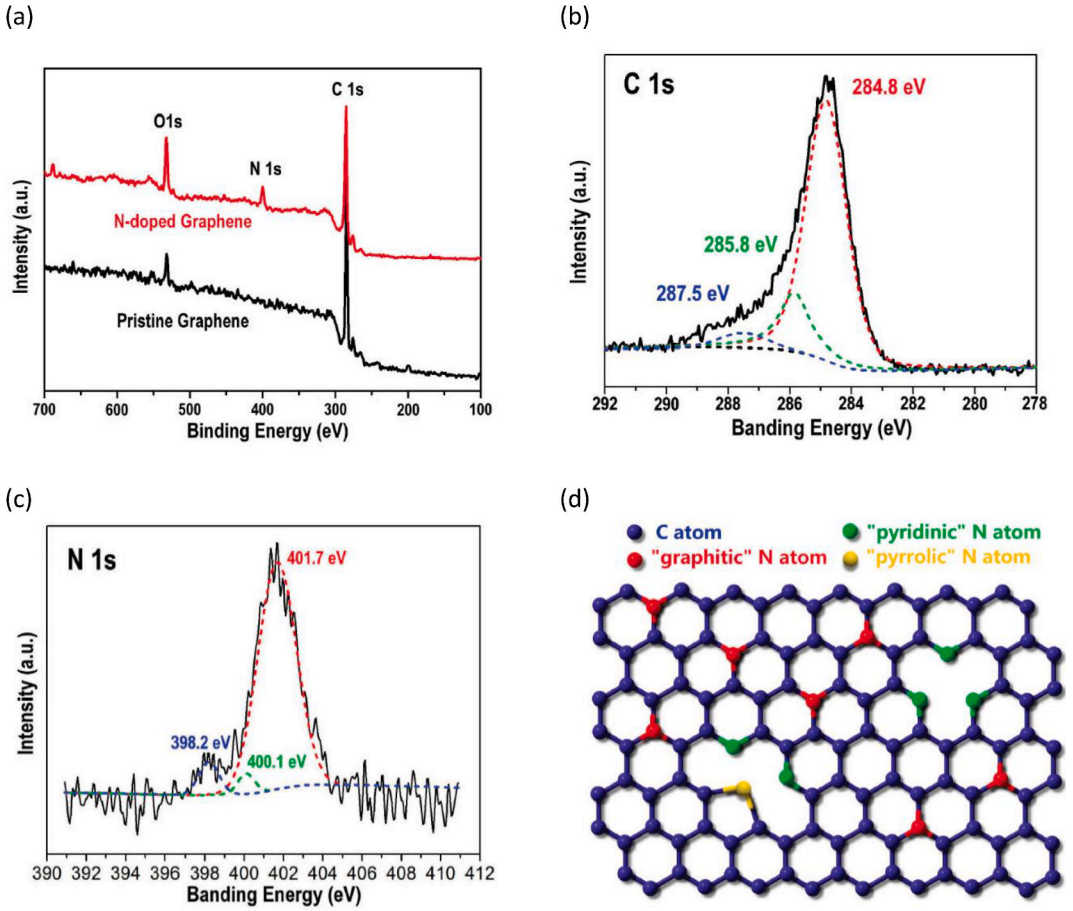

Fig. 15. (a) XPS spectra of the pristine graphene and the *N*-doped graphene. (b) XPS C 1s spectrum and (c) XPS N 1s spectrum of the *N*-doped graphene. The C 1s peak can be split to three Lorentzian peaks at 284.8, 285.8, and 287.5 eV, which are labelled by red, green, and blue dashed lines. The N 1s peak can be split to three Lorentzian peaks at 401.7, 400.1, and 398.2 eV, which are labelled by red, green, and blue dashed lines. (d) Schematic representation of the *N*-doped graphene. The blue, red, green, and yellow spheres represent the C, "graphitic" N, "pyridinic" N, and "pyrrolic" N atoms in the *N*-doped graphene, respectively. Images were adapted with a permission from ref. [141].

organic solar cell (OSC) is a charge transport layer (ETL or HTL) and is usually deposited by a solution processing method such as spin coating. The hydrophobic nature of graphene hinders the formation of a uniform coating of the charge transport layer. In addition, the low WF of intrinsic graphene (4.3 eV) [145,146] can lead to inefficient collection of the photo-generated charge carriers as a result of poor alignment between its Fermi level (E_f) and the HOMO/valence band of the HTL in regular geometry OSCs similar to the case of PEDOT: PSS HTL. In addition, the low WF of the TCE material can reduce the V_{OC} of the OPV device and hence cause a low PCE [147]. The R_s of CVD-graphene can also be reduced via some of the dry post treatment procedures such as thermal annealing [148]. O_2 plasma treatment of graphene was found to improve its wettability due to the formation of polar groups (*C*–O bonds), but the R_S increased compared to pristine graphene. Interestingly, the increase in R_S was found to be less as the number of layers in graphene film increased, which confirmed that O_2 plasma affects the top layer. However, the overall performance of the OPV device based on the O_2 plasma-treated graphene was much higher than that of the pristine graphene, which had a very poor performance as a result of graphene hydrophobicity, which hindered the formation of a uniform PEDOT: PSS HTL [149]. Plasma has also been widely used for nitrogen (N)-doping of graphene [150–153]. For example, ammonia (NH_3) gas was used to fabricate *N*-doped graphene upon RF plasma discharge [151]. CVD-graphene films were post-treated in an RF plasma reactor in an NH_3 atmosphere. The resulting *N*-doped graphene exhibited different electronic structure with its E_f shifted in the conduction band compared to the pristine graphene, whose E_f lies on the top of the valence band due to the electron donor nitrogen atoms, which makes *N*-graphene act as n-type semiconductor. Similarly, plasma was used to synthesize boron-doped graphene for a p-type doping [154]. In addition to plasma post-doping, UV-ozone has been reported as an effective method to produce oxygen (O)-doped graphene which was employed as a hole interfacial layer in regular geometry OPVs [155]. The O-functionalized CVD-graphene was synthesized by UV-Ozone treatment of the transferred CVD-graphene on top of PEDOT: PSS HTL for various time spans. The optimum *O*-graphene resulted in an enhancement in the device performance and stability under ambient conditions compared to the control device without graphene, while that with pristine graphene exhibited a declined performance. The improved PCE of the device based on the optimum *O*-graphene was attributed to the enhanced hole extraction and tuning of the surface energy of the *O*-graphene's hydrophilic surface. More importantly, the *O*-graphene layer prevented the acidic PSS (in PEDOT: PSS) from penetrating into the photoactive layer resulting in higher device stability. Similarly, electron-beam (EB) irradiation for a few seconds was reported to be an effective method to produce O-doped graphene with improved surface wettability [156]. A P3HT: PCBM-based OPV device built on an EB-irradiated CVD-graphene (with 5 s irradiation time) had an improved PCE of 2.76 % due to the enhanced *FF* (0.54) and J_{SC} (8.96 mA/cm^2) compared to that based on the non-EB irradiated graphene, which had lower values for PCE (1.78 %), *FF* (0.41) and J_{SC} (7.74 mA/cm^2). This significant improvement was attributed to the improved hydrophilicity of the irradiated graphene leading to uniform coating of PEDOT: PSS HTL. Nevertheless, long irradiation time (100 s) resulted in a decline in the device performance due to the increased defect concentration in the graphene lattice leading to an increased R_s value. Thermal treatment [157] and electrochemical [158] *N*-doping have been also reported, but these methods produce low N content *N*-graphene. In addition, thermal evaporation is an effective way to synthesize doped graphene through the deposition of an ultrathin metal oxide layer such as MoO_x to improve the electronic band structure and wettability of graphene [159,160]. For example, it was reported that thermally-evaporated 2 nm thick MoO_3 on top of a graphene anode in a regular geometry P3HT: PCBM based OPV device led to a significant increase in its PCE [147]. The performance enhancement was attributed to the improved hydrophilicity of graphene, which led to a uniform HTL of PEDOT: PSS and the increased WF of pristine graphene from 4.36 eV to 5.47 eV for MoO_3-coated graphene due to the high WF of MoO_3 (6.1–6.6 eV) [161]. The higher WF of MoO_3-graphene achieved more efficient band alignment with the HOMO (5.2 eV) of the P3HT donor polymer, resulting in improved hole extraction. Similar advancement was later reported by Sung et al. for perovskite solar cells (PSCs) [94]. They found that adding a 2 nm layer of MoO_3 on top SLG TCE reduced the contact angle of PEDOT: PSS solution from 90.4° (with pristine SLG) to 30°. In addition, the sheet resistance of the 2 nm MoO_3-coated SLG dropped from >2 kΩ $\square^{-1}$ to 500 Ω $\square^{-1}$. The improved wettability, electrical properties and the increased WF of the MoO_3-doped SLG resulted in a high-performance PSC with PCE >17 %, while the fabrication of a functional device, with the same structure, on the as-grown graphene was not possible, which is understandable given the high hydrophobicity of the pristine graphene (Fig. 16).

4.5.2.2. Wet doping. Wet doping of graphene includes the post-treatment with strong acids, polar organic components, and metal chloride. Similar to dry doping, the wet doping of graphene facilitates tuning the properties of graphene for specific applications. For example, Han and colleagues reported a reduced R_s and higher WF for CVD-graphene TCEs for OLEDs via HNO_3 and $AuCl_3$ doping [162]. Many researchers have reported the chemical doping of graphene using inorganic small molecule acids [110,162,163] such as HNO_3, H_2SO_4, and HCl as well as metal chlorides ($FeCl_3$, $AuCl_3$, etc.) [162,164–167]. However, there are some drawbacks associated with these dopants such as environmental instability and the reduction of metal cations. In case of inorganic acids, the sheet resistance of the doped graphene increases with time because of the volatile nature of these molecules. For metal chloride dopants, the reduction of metal cations results in metal particles on the surface of graphene, which can reduce its optical transmittance, especially when these particles are large, and can degrade the graphene morphology by forming protrudes that increase leakage current of the device [162,164–167]. In order to overcome these issues, Kown et al. [168] employed non-volatile polymeric acid (perfluorinated polymeric sulfonic acid (PFSA)) to produce p-type doped CVD-graphene. PFSA was spin coated on top of a 4-layer high quality CVD-graphene leading to significant enhancement in the conductivity of the resulting PFSA-doped graphene with outstanding chemical and thermal stability. The PFSA-graphene exhibited a reduced R_s of 91.4 ± 30 Ω $\square^{-1}$ compared to pristine graphene (352 ± 48 Ω $\square^{-1}$), which, in contrast to HNO_3-doped graphene, remained extremely-stable under different conditions including ambient air, chemical solvents, and temperature. Moreover, the PFSA dopant increased the WF of the doped graphene by 0.71 eV compared to pristine 4-layer graphene. The optical transmittance of the doped film exhibited a slight drop from 90 % (pristine graphene) to 89 %. Despite the remarkable stability and the enhanced properties of the PFSA-graphene, it increased the hydrophobicity of graphene. The water contact angle (WCA) of PFSA-graphene was 96.7°, while the pristine 4-layer graphene had a WCA of 55.3°, which is often unfavourable for device fabrication as discussed earlier. Likewise, polar organic components showed excellent potential to improve the R_s, morphology, and the WF of CVD-graphene for optoelectronics [169,170]. For instance, bis(trifluoromethanesulfonyl)amide (TFSA) caused the WF of the TFSA-doped graphene to increase to 5.1 eV compared to that of pristine graphene (4.4 eV). Since the HOMO of the most common HTL material (PEDOT: PSS) lies at 5.2 eV [94], the TFSA-graphene should form an appropriate band alignment with PEDOT: PSS, which facilitates enhanced hole transport. In addition, the TFSA-5 layer graphene had as low R_s as 90 Ω $\square^{-1}$ with high optical transmittance of 88 % at 550 nm [169].

4.6. Graphene & AgNWs hybridization

The extraordinary electrical conductivity of graphene is mainly attributed to its extensive carrier mobility (theoretical value of 200 000

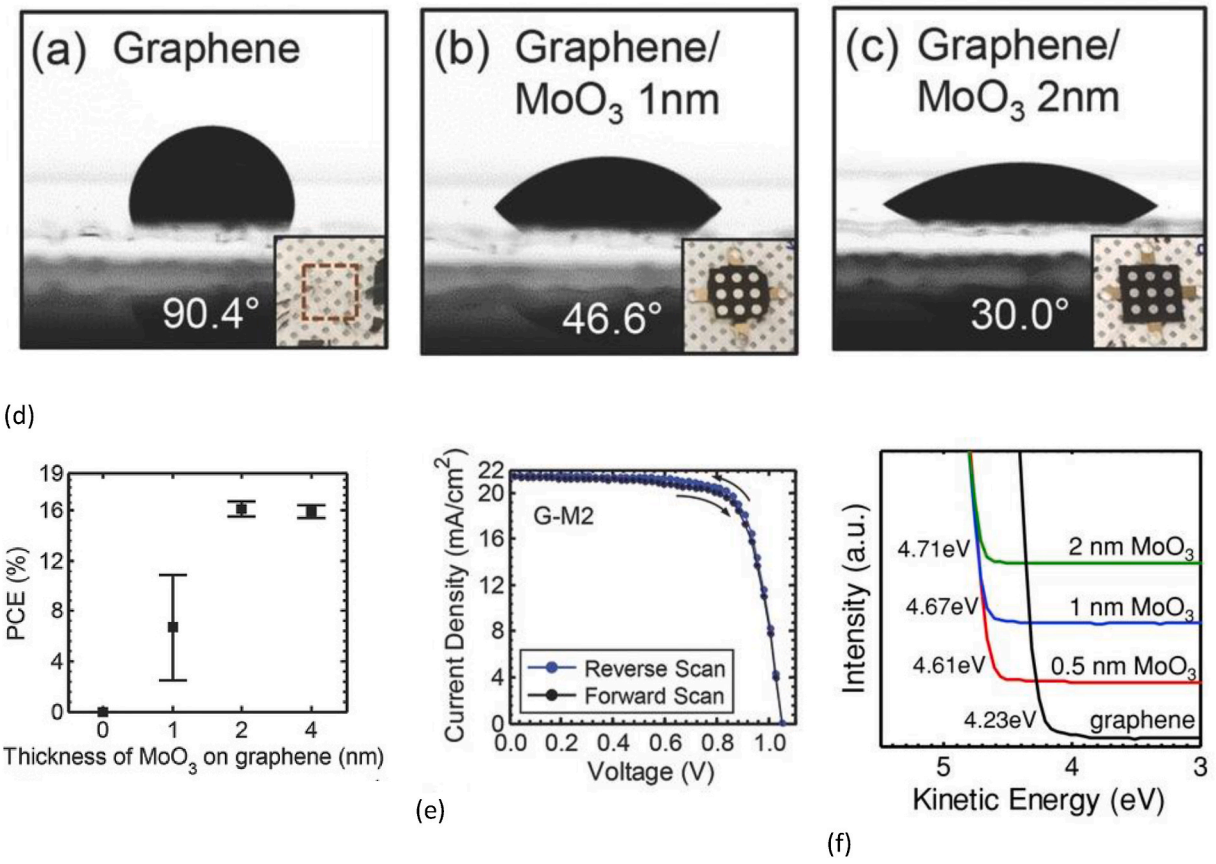

Fig. 16. Droplets of PEDOT: PSS on a) as-prepared graphene, b) graphene covered with 1 nm MoO_3, c) graphene covered with 2 nm MoO_3. (d) Relationship between average PCE and MoO_3 thickness for graphene electrodes. (e) J–V curves for best performing G-M2. (f) UPS spectra and calculated work functions of graphene with MoO_3 layers of varying thickness. Images were reproduced with a permission from ref. [94].

cm^2/V.S) [171]. This outstanding behaviour is due to the ballistic transport of charge carriers, which means that electrons travel at high speed within the graphene lattice without being scattered off. The presence of different kinds of structural imperfections such as voids, vacancies, dislocations, wrinkles, ripples, folds, tears, cracks, etc. increases the electron scattering within graphene and results in a dramatic drop in its carrier mobility and electrical conductivity compared to its intrinsic properties. Although defect-free and high-quality CVD graphene has been reported for films synthesized on metal catalysts at elevated temperatures (~1000 °C), structural defects are induced during transfer processes or low-temperature PECVD of graphene growth on dielectric substrates leading to high R_s, which limits their applicability as TCEs for optoelectronics. The utilization of one-dimensional materials (metal NWs) to suppress the detrimental impact of structural line defects in transferred CVD-SLG was theoretically predicted by Jeong and colleagues [172]. Later, this approach was experimentally validated by Kholmanov et al. [148], who found that transferring CVD-graphene grown on Cu foil onto AgNWs-coated glass reduced the R_s from 1050 $\Omega\,\square^{-1}$ to 64 $\Omega\,\square^{-1}$, while the AgNWs film was not conductive as a result of the sub-percolation network AgNWs. This improvement in electrical conductivity revealed that AgNWs bridge the line disruptions and line defects and provide new pathways for charge transport.

AgNWs are also excellent TCE candidate for optoelectronics due to their remarkable optical and electrical properties despite their chemical and mechanical instabilities [173,174]. The transfer of graphene onto the conducting AgNWs network was also investigated [175–177]. For instance, CVD-SLG was transferred onto a highly conductive AgNWs film coated-glass for OPVs [176]. AgNWs-graphene hybrid TCE-based inverted-geometry OPV device with PTB7: $PC_{71}BM$ active layer achieved competitive PCE and *FF* of 8.12 % and 0.69 to those of the reference device built on ITO (8.22 % and 0.70) and higher than the AgNWs-based counterpart (7.32 % and 0.65) as shown in Fig. 17 [176]. Adding graphene on top of AgNWs reduced the R_s of AgNWs film from 18.5 $\Omega\,\square^{-1}$ to 14.9 $\Omega\,\square^{-1}$ for hybrid AgNWs-graphene with higher figure of merit (FoM).

Furthermore, the hybrid film had a smoother surface than the pristine AgNWs, which is more favorable for device performance to avoid short-circuits. More importantly, the chemical stability of AgNWs film under ambient air was greatly enhanced due to the top graphene layer, which prevented oxygen molecules from reaching AgNWs underneath, thus increasing the stability of AgNWs under environmental conditions. Consequently, the R_s of the AgNWs-graphene hybrid film was almost unchanged under ambient air for two months, while that of AgNWs increased by 80 % because of oxidation of Ag as confirmed by morphology change (Fig. 17). Additionally, the hybrid electrode showed a good corrosion resistance in NaOH solution (1 M) with constant R_s due to the graphene protection layer, while the pristine AgNWs film degraded rapidly. Similar findings were obtained for flexible OPV devices based on AgNWs-graphene hybrid TCEs on PET substrate with much higher mechanical stability for both AgNWs-hybrid and AgNWs-based devices compared to ITO [175,177]. The graphene protective layer did not only improve the stability of the hybrid TCE due to its gas-barrier characteristics, but also enhanced the overall stability of the OPV device as shown in Fig. 17f [175]. The OSC (with P3HT: $PC_{60}BM$ active layer) on the hybrid AgNWs-Gr retained 61 % of its original PCE after 480 h, while AgNWs-based OSC lost half of its initial PCE within 320 h as a result of fast degradation of J_{SC} under ambient conditions. This enhancement was ascribed to the minimum degradation of the interface between the electron transport layer (ZnO) and AgNWs due to the transferred graphene layer [178].

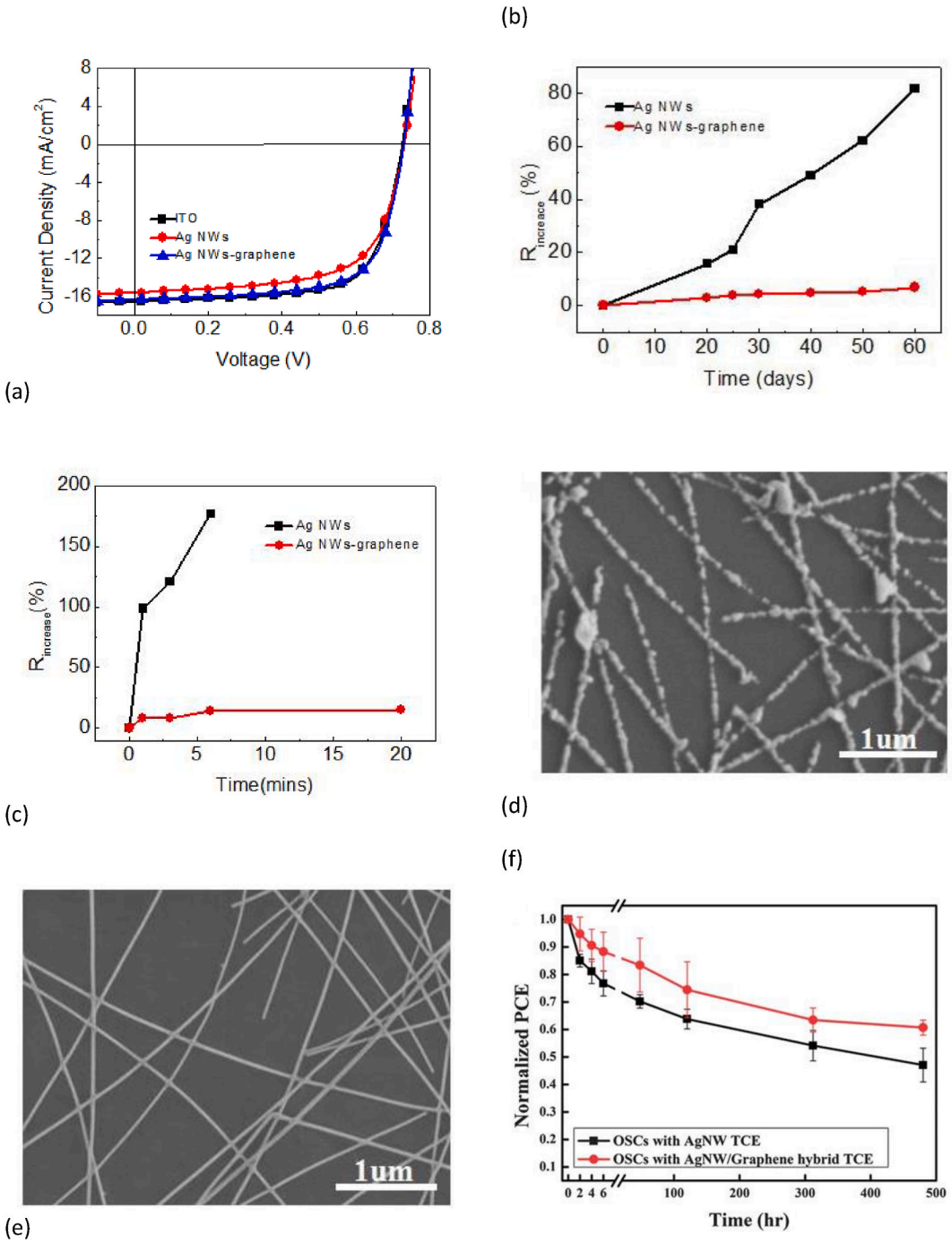

Fig. 17. (a) *J-V* and (c) EQE curves of the devices based on the ITO, pristine AgNWs, and AgNWs-graphene TCEs.(b) Change in sheet resistance of the pristine AgNWs and AgNWs-graphene TCEs exposed to ambient at room temperature for 2 months. (c) Change in sheet resistance of the pristine AgNWs and AgNWs-graphene TCEs exposed to NaOH solution (1 mol/L). SEM images of the pristine AgNWs (d) and AgNWs-graphene (e) exposed to ambient at room temperature for 2 months. Images were adapted with a permission from ref. [176]. (f) Device performance of inverted BHJ OSCs with AgNWs and AgNWs–graphene hybrid TCEs as a function of exposure time under ambient conditions without encapsulation. Images were reproduced with a permission from ref. [175].

AgNWs were also coupled with graphene nanosheets synthesized by different approaches such as electrochemical exfoliation [29]. The exfoliated graphene (EG) was spray coated on a conductive AgNWs mesh to form hybrid AgNWs-EG TCE for rigid and flexible optoelectronics. Significant improvements in the electrical conductivity, morphology, chemical and mechanical stabilities were recorded for the hybrid film in comparison to the pristine AgNWs counterpart as shown in Fig. 18a–d. More interestingly, EG played a vital role in flattening AgNWs rough surface while the pristine AgNWs based OSC exhibited short circuit because of the high surface roughness and large heights at the junction sites of the nanowires. Devices based on AgNWs-EG TCEs exhibited a comparable performance to the reference ITO-counterpart, while devices fabricated on bare AgNWs were short circuited (Fig. 18e).

Another strategy to efficiently hybridize graphene with AgNWs for TCE applications can be realized through adding AgNWs on top of graphene. In this approach, AgNWs also provide additional transport channels for charge carriers and can help connect graphene domains leading to a dramatic drop in the R_s with a little reduction in the optical

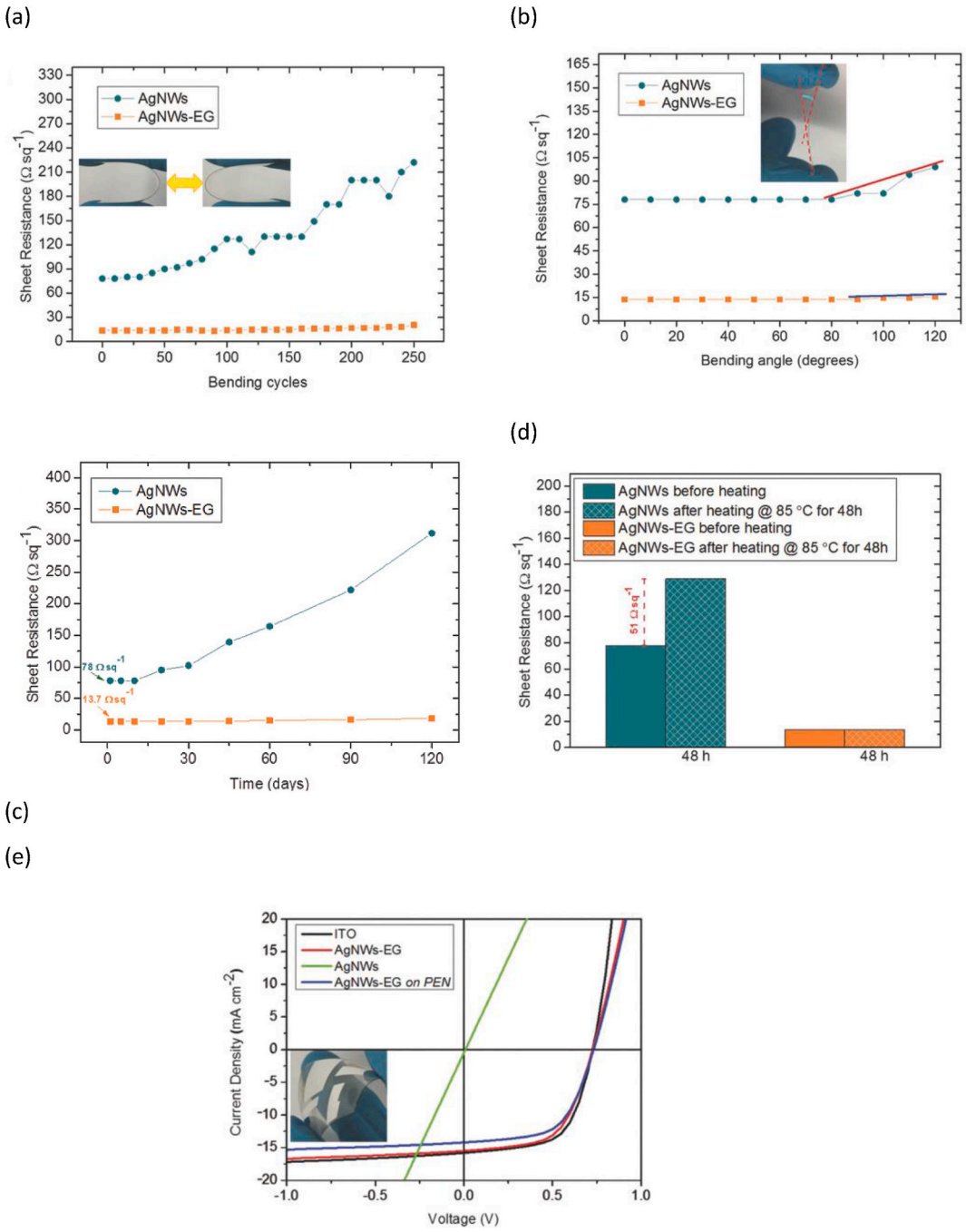

Fig. 18. R_s response of AgNWs and AgNWs–EG films on PEN substrate to a) different bending cycles, b) bending angles, c) air exposure over a period of 120 days, and d) 48 h at 85 °C, e) *J–V* curves of the OSC devices (inset: flexible AgNWs–EG OSC). Images were adapted with a permission from ref. [29].

transmittance of the hybrid film [179]. Moreover, this strategy improves the wettability of the TCE surface leading to homogeneous and uniform coating of the charge transport layer. However, further procedures may be needed to planarize the rough surface of AgNWs and to avoid shorts during device fabrication [180]. Several reports on the deposition of AgNWs onto graphene for TCEs with improved performance can be found in literature [181–183].

In this regard, AgNWs were brush painted on top of bi-layer PMMA-transferred CVD-graphene for flexible OPVs [184]. Compared to the pristine transferred bi-layer graphene on PET, the graphene-AgNWs (Gr-AgNWs) hybrid films showed lower R_s, which significantly dropped with increasing the brush cycles (the number of brush paintings) with a subsequent slight drop in their optical transmittance. The pristine graphene and the optimum hybrid film (at 3 brush cycles) showed excellent mechanical flexibility, but the later had much higher FoM and improved wettability. As a result, flexible regular-geometry OSC with P3HT: PCBM active layer developed on the hybrid Gr-AgNWs had higher PCE (2.681 %), *FF* (0.5498), J_{SC} (8.244 mA cm^{-2}), and V_{OC} (0.591 V) than that on graphene with PCE (1.681 %), *FF* (0.4114), J_{SC} (7.488 mA cm^{-2}), and V_{OC} (0.5498 V), respectively. The lower V_{OC} was attributed to the lower WF of pristine graphene which increased the barrier for hole collection, while the reduced *FF* was due to the non-uniform coverage of the PEDOT: PSS HTL because of the hydrophobic nature of pristine graphene. On the contrary, the Gr-AgNWs hybrid configuration can cause instability issues due to the degradation of AgNWs under ambient conditions as discussed earlier. Zhang et al. [185] reported the

degradation of Gr-AgNWs films under elevated temperature of 80 °C and relative humidity (RH) of 50 % over the exposure time. They found that the R_s of the hybrid film increased by almost four times to its initial magnitude after 7 days because of thermal oxidation of Ag. Additionally, their hybrid film exhibited a change in R_s of more than 300 % after 3000 bending cycles at a bending radius of 5 mm. To overcome these limitations, they introduced a poly vinyl alcohol (PVA) encapsulation thin layer by spin coating to the Gr-AgNWs hybrid film, which resulted in a significant enhancement in the film stability without sacrificing its optical or electrical features. Further enhancement in the features of hybrid Gr-AgNWs TCEs for flexible OSCs (FOSCs) has been achieved by spin coating graphene quantum dots (GQDs) on top of the Gr-AgNWs hybrid film [186]. The addition of GQDs improved the electrical conductivity and light harvest and increased the WF of the hybrid TCE film, leading to a better photovoltaic performance. In addition, the mechanical stability of the GQDs-hybrid TCE and the associated FOSCs remarkably enhanced compared to the control Gr-AgNWs counterpart as shown in Fig. 19. GQDs-hybrid TCE-based FOSCs maintained 92 % of its initial PCE after 1000 bending cycles, while that without GQDs lost 60 % of its original PCE after the same test. This finding was in a good agreement with the change of R_s with bending due to cracks in AgNWs in case of Gr-AgNWs, while the GQDs protected AgNWs from cracking. They also found that bare graphene film had an excellent stability against bending. In addition, the GQDs layer was found to protect AgNWs within the hybrid film from oxidation in ambient atmosphere and thus increased the storing longevity of the device.

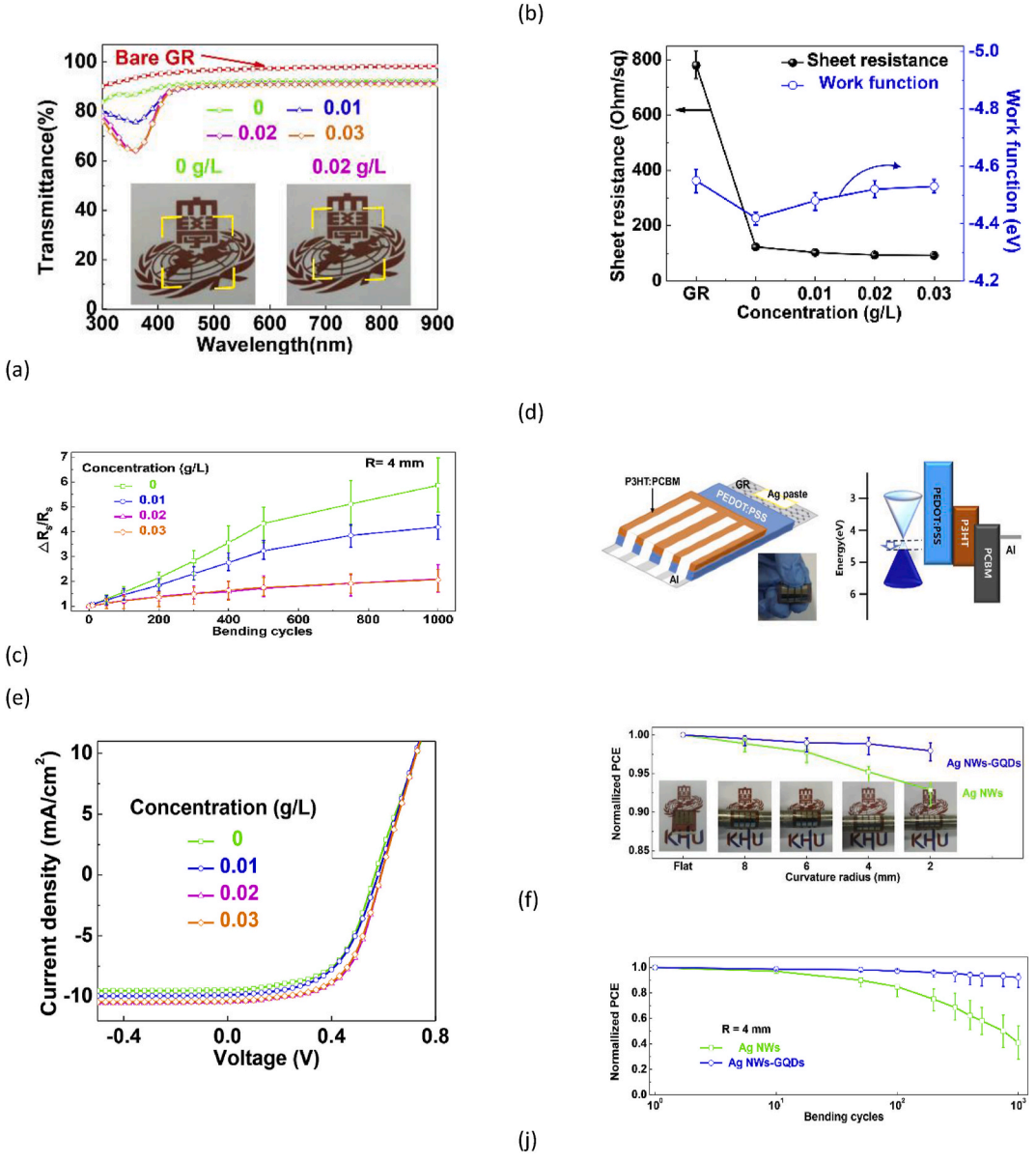

Fig. 19. (a) Optical transmittance spectra, (b) sheet resistances, and work functions of GR, Ag NWs/GR, and GQDs-mixed Ag NWs/GR TCEs. Here, the concentration of GQDs (n_G) is varied from 0.01 to 0.03 g/L. The yellow brackets in the inset of (a) show real images of the Ag NWs/GR TCEs with/without GQDs, indicating their excellent transparency. (c) Normalized $\Delta R_s/R_s$ of Ag NWs/GR TCEs as functions of bending cycle at a curvature radius of 4 mm for various n_G. (d) Schematic structure and energy band diagram of a typical FOSC containing Ag NWs/GR TCEs with/without GQDs. The inset in (a) shows a real image of the FOSC and the blue arrow indicates the shift of Fermi level in the Ag NWs/GR TCEs. (e) Photo *J-V* curves of the Ag NWs/GR TCE/FOSCs for various n_G. (f) Normalized PCEs of the Ag NWs/GR TCE/FOSCs as functions of bending radius for $n_G = 0$ and 0.02 g/L. The inset shows real images of the FOSCs at each R. (j) Normalized PCEs of the Ag NWs/GR TCE/FOSCs as functions of bending cycle at a fixed bending radius of 4 mm for $n_G = 0$ and 0.02 g/L. Here, the data are presented with error bars of standard deviation after being averaged for four separate FOSCs. Images were reproduced with a permission from ref. [186].

Despite the progress achieved in improving the performance of OSCs via the hybridization of CVD-graphene and AgNWs, graphene films produced with such hybrid TCEs still require complex transfer procedures. Therefore, more research effort is needed to develop cost and time-effective strategies to produce scalable transfer-free graphene/AgNWs TCEs for OPVs and other optoelectronic devices. In this context, Kamel et al. [86] have investigated effective pathways to hybridize AgNWs with directly synthesized graphene TCEs on glass substrates via RF-PECVD from sustainable plant extract to avoid graphene transfer. They reported two hybridization approaches: 1) growing graphene directly on top of AgNWs-coated glass, 2) spin-coating AgNWs on top of the VG synthesized on glass (Fig. 20). In the first case, the electrical conductivity of the resulting hybrid AgNWs-graphene film and the performance of the associated OPV device were found to improve compared to pristine graphene at low concentration of AgNWs (<2 mg/ml). This enhancement was assigned to the reduced R_s of the AgNWs-graphene (AgNWs-Gr) hybrid TCE because of additional conduction pathways provided by AgNWs. At higher concentrations (3 mg/ml) of AgNWs dispersion, the resulting AgNWs-Gr TCE had a lower optical transmittance, high R_s and highly rough surface due to the increased and non-uniformly distributed growth of VG nanosheets close to and above AgNWs. More interestingly, following the second approach, they noticed that the growth of VG nanosheets overcame the impact of the rough surface of AgNWs, which was found to uniformly distribute on top of graphene without large aggregations compared to AgNWs on bare glass as confirmed by SEM images (Fig. 20 b &c).

Consequently, P3HT: PCBM OSCs fabricated on the developed hybrid graphene-AgNWs TCEs exhibited a comparable PCE (2.18 %) and *FF* (0.63) to the ITO-counterpart (2.22 % and 0.60), while devices on bare AgNWs were short-circuited. The addition of AgNWs onto transfer-free graphene significantly reduced the R_s of the resulting graphene-AgNWs hybrid film. More crucially, the higher *FF* of OPVs based on Gr-AgNWs TCE was attributed to the increased contact area of the interface between the Gr-AgNWs and the active layer leading to enhanced collection of the photo-generated charge carriers compared to that built on ITO.

5. Comparison between graphene and other TCE candidates

In this section, a comparison between graphene and other TCE candidates, namely ITO, CNTs, AgNWs, and PEDOT: PSS is provided. Although ITO is the most common TCE material due to its low sheet resistance and good optical transmittance (>80 % at 550 nm), its high cost, scarcity of indium and poor mechanical and stabilities push researchers to develop affordable and stable alternatives. In addition, ITO is not a good choice for flexible solar cells due to its fast degradation under mechanical bending. Since the PV parameters widely vary with different active layers, interlayers, film thickness, preparation

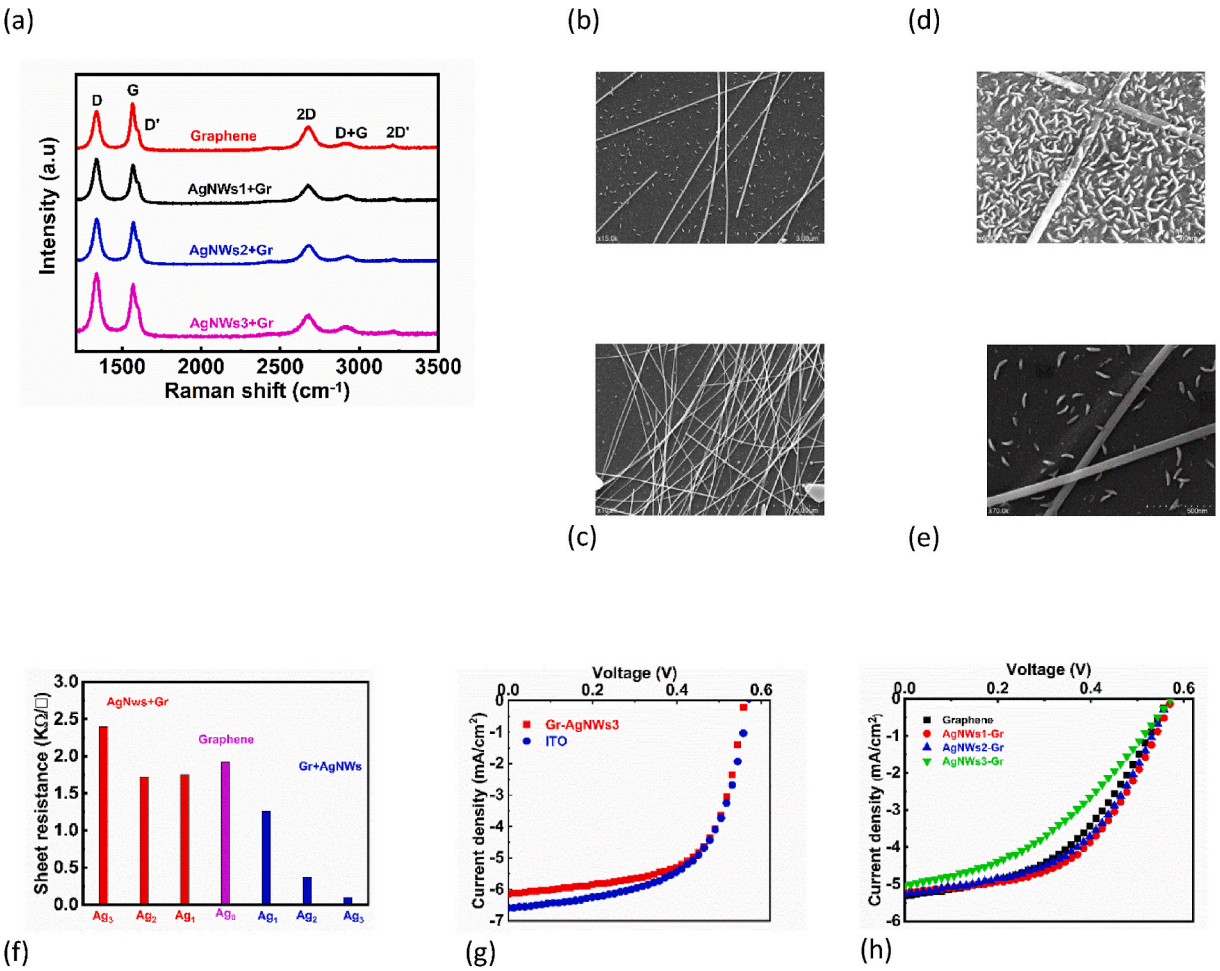

Fig. 20. (a) Raman spectra for graphene films grown on AgNWs-coated glass with different concentrations of AgNWs (1–3 mg/ml). SEM images for AgNWs (3 mg/ml) spin coated on top of (b) graphene and (c) bare glass. (d) SEM image for graphene growth on top of AgNWs (3 mg/ml) on glass which shows thick VG nanosheets. (e) High resolution SEM image for AgNWs (1 mg/ml) on top of graphene revealing AgNWs reset among VG nanosheets. (f) R_s of transfer-free graphene, AgNWs-graphene, and graphene-AgNWs at different concentrations of AgNWs (1–3 mg/ml). J-V curves for P3HT: PCBM OPVs developed on the hybrid graphene-AgNWs3 compared to ITO-counterpart (e) and for the devices on pristine graphene and the AgNWs-graphene hybrid TCEs (h) at concentrations of AgNWs varying from 1 to 3 mg/ml. Images were adapted with a permission from ref. [86].

conditions, it will be hard to give a fair comparison between devices with different TCEs. Therefore, the PV parameters of such devices will be compared to their ITO-counterparts, prepared in the same work, when appropriate.

Different values of R_s and transmittance for these different TCE candidates are reported in literature. For example, the sheet resistance of CNTs were mentioned to vary between 100 and 10 000 Ω $\square^{-1}$ at transmittance around 80 % [187]. Thus, in Table 1, the transmittance and sheet resistance of the particular electrode will be provided as reported in each cited work rather than giving an overall range for each category.

Several examples from literature on graphene TCEs by CVD (either transferred or transfer-free synthesis) were provided in Table 1 to highlight its excellent potential to replace ITO. However, the goal of this review is to pave the way towards cost- and time-effective transfer-free production of graphene TCEs for OPVs.

6. Limitations and outlooks

OPVs have shown a promising potential to replace their inorganic counterparts due to their low fabrication cost, solution processability, abundance and tunability of materials. In addition, the mechanical flexibility and lightweight of OPVs make them perfect candidates for wearable and portable applications. Solution processability of OPVs enables their cost-effective and scalable printing via R2R production. The innovation of new donor polymers and non-fullerene acceptors as well as the progress in device engineering has revolutionized the field of OPVs and increased its feasibility towards large-scale commercialization. The PCE of OPVs has recently achieved new records with single-junction and tandem devices approaching and exceeding 20 %, respectively. However, many issues need to be addressed before OPVs can be commercialized.

One of the major challenges for OPVs is developing efficient TCE that can overcome the issues offered by the benchmark ITO such as high costs, mechanical brittleness, and scarcity of indium. Several alternatives have been proposed including conducting polymers, graphene, metal nanowires, thin metal films, and carbon nanotube. Among those materials, graphene with its sp^2 hybridized hexagonal carbon structure of single atom thickness has received the greatest research interest due to its outstanding and tunable optical, electrical, and mechanical properties. Various methods have been developed to synthesize graphene for a wide range of applications.

CVD is an excellent bottom-up approach to synthesize large-area graphene films. CVD has been the most extensively investigated method for developing graphene TCEs for OPVs due to its scalability, and potential to produce high-quality graphene. In brief, CVD of graphene includes the flow of vaporized molecules of a carbon source (e.g., CH_4) through a metal (e.g., Cu, Ni) catalyst surface at high temperature (~1000 °C) in the presence of carrier gas/es (H_2, Ar). The precursor molecules thermally decompose into dehydrogenated species, which then adsorb onto the substrate surface and nucleate before the growth of graphene sheets. The resulting CVD-graphene film is later transferred from the metal catalyst onto a target transparent substrate such as glass, PET, PEN, etc. To be used as TCE. Thus, the quality of CVD-graphene TCEs critically depends on the deposition parameters and the transfer procedures.

Although thermal CVD can produce SLG or FLG films with low or minimum structural defects, it has several limitations that need to be overcome prior to its wide use for optoelectronics. These drawbacks include the high cost, time-consumption, use of environmentally hazardous and unsustainable carbon sources, and the complexity of the procedure. More importantly, the expensive, multi-step and complicated transfer processes can induce structural defects in the graphene films and hence deteriorate their electrical and optical characteristics. Intensive research interest has focused on the development of efficient CVD-graphene TCEs for OPVs and other optoelectronics including perovskite and dye sensitized solar cells, and organic light emitting diodes. Great progress has been made in CVD-graphene TCEs including R2R production (on Cu foils) and R2R transfer of CVD-graphene. The development of time- and cost-effective, large-scale, and damage-free transfer methods of CVD-graphene is an effective strategy towards commercial CVD-graphene TCEs. Nonetheless, the high temperature and complexity of the overall production of CVD-graphene TCEs make it less competitive to ITO.

The transfer-free production of CVD-graphene TCEs represents the ideal approach for scientists and researchers towards ITO-free future optoelectronics. The employment of various types of plasma in CVD resulted in a reduction in the temperature needed for the decomposition of precursor molecules and for the nucleation and growth of graphene. Consequently, PECVD facilitated the direct synthesis of graphene on a wide range of dielectric substrates including different types of glass. However, the directly synthesized PECVD-graphene on dielectric substrates has exhibited several limitations such as high concentration of structural defects (because of energetic particles in plasma), small grains, and discontinuity, which increase its sheet resistance. More interestingly, PECVD-graphene films consist of vertically oriented graphene (VG) nanosheets on top of a horizontal carbon buffer layer in contrast to the in-plane graphene films in traditional thermal CVD. This in-plane buffer layer can be amorphous carbon, graphite, or graphene depending on the deposition parameters. The vertical growth of graphene nanosheets makes the surface of the resulting PECVD-graphene rough, which is not favorable for device fabrication because of the increased carrier recombination and leakage current [87].

Advances have been made over the past decade to improve the electrical properties of the directly synthesized CVD/PECVD-graphene without deteriorating its optical transmittance. This included several strategies such as optimizing the deposition parameters, doping, post-treatment, deposition of metal catalyst ultrathin films on the dielectric substrate prior to graphene synthesis, and the hybridization with one dimensional materials mainly silver nanowires (AgNWs). The optimization of the deposition parameters of PECVD control growth of VG nanosheets for an optimum trade-off between the sheet resistance and optical transmittance. Graphene doping can be realized by direct synthesis or post-treatment methods. Different dopants such as strong acids, metal oxides, organic polar components, and metal chlorides can improve the electrical conductivity, morphology, and wettability of graphene films. Furthermore, doping can increase the work function of graphene, which is essential for efficient energy band alignment with many common charge transport layers such as PEDOT: PSS.

Post-treatment procedures such thermal and vacuum annealing as well as low power and short-time plasma treatment can also reduce the sheet resistance and hydrophobicity of graphene, respectively. The pre-deposition of thin layer of a metal catalyst on the transparent dielectric substrate has been reported to facilitate the production of high-quality SLG and FLG TCEs on PET substrates at 150 °C in a dc sputtering –integrated PECVD reactor [54] and a split thermal CVD setup [136]. AgNWs have been widely used with CVD-graphene for optoelectronics. The AgNWs-graphene hybrid TCEs offer excellent optical and electrical properties. Moreover, the addition of graphene on top of AgNWs reduces the surface roughness and increases the stability of AgNWs due to its barrier properties. However, this approach necessitates graphene transfer procedures. Instead, AgNWs can be coated on top of graphene, which greatly enhances its electrical properties, but this configuration has low stability due to oxidation of Ag within the exposed AgNWs. More importantly, further procedures such as hot-rolling are needed to modify the rough surface of AgNWs to avoid shorts during device fabrication.

Based on the different aspects discussed in this review, some perspectives for future research towards efficient and scalable production of CVD-graphene for OPVs and other optoelectronics can be proposed. The use of environmentally friendly carbon sources such as volatile and carbon-rich plant extracts of essential oils makes graphene synthesis sustainable and eco-friendly process. Liquid carbon sources (e.g.

Table 1
Summarizes the PV parameters and electrode properties for some OPV and perovskite solar cell devices based on different TCE materials and compared to the state-of-the-art ITO under identical conditions. The advantages and challenges of each TCE candidates are also listed.

TCE	R_s ($\Omega\,\square^{-1}$)	T (%)	Active layer	PCE (%)	FF	J_{SC} (mA/cm^2)	V_{OC} (V)
PEDOT: PSS [188]	–	–	PBDB-T: IT-M	10.6	0.72	16.01	0.925
ITO	–	–		11.01	0.77	16.08	0.93
Flex-PEDOT:PSS	Ca. 40	Ca. 86		10.12	0.703	15.49	0.93
Flex-ITO	–	Ca. 81		7.93	0.65	13.56	0.905
PEDOT: PSS [189]	Ca. 250	Ca. 76	P3HT: PCBM	Ca. 2.6	0.52	8.5	0.58
ITO	12	Ca. 80		Ca. 3.4	0.62	Ca. 9	Ca. 0.59
Flex-AgNWs [190]	24.4	83.2	PBDB-T-2F:IT-4F	11.6	0.72	19.6	0.82
ITO	–	85.7		12.3	0.73	20.50	0.82
Flex-AgNWs	24.4	83.2	PTB7-Th:IEICO-4F	10.3	0.67	22.69	0.68
Flex-AgNWs	24.4	83.2	PBDB-T: ITIC	9.3	0.67	15.72	0.88
Flex-AgNWs [17]	10	92	PTB7-Th: $PC_{71}BM$	9.82	0.702	17.43	0.802
ITO (glass)	–	–		10.12	0.704	18	0.799
Flex-AgNWs	10	92	Tandem device	16.55	0.71	14.22	1.64
SW-CNTs [191]	101	90	P3HT: PCBM	2.43	0.46	8.84	0.59
ITO	–	–		2.83	0.50	9.42	0.60
SW-CNTs	28.5	65 %	PTP7:PCBM	6.04	0.61	13.7	0.72
ITO	–	–		7.31	0.64	15.5	0.74
Pristine DW-CNTs [192]	150	Ca. 80	Perovskite	15.6	0.725	21.4	1.01
HNO_3-doped CNTs	125	Ca. 80		16.7	0.742	20.7	1.04
TFMS-doped CNTs	110	Ca. 80		17.2	0.771	21.4	1.05
ITO	12	Ca. 88		19	0.779	22.9	1.06
Pristine SW-CNTs [193]	250	Ca. 75	Perovskite	12.8	0.76	17.5	0.96
HNO_3-CNTs	51 ± 10	–		15.3	0.78	19.9	0.98
ITO	–	–		17.8	0.83	21.6	0.99
CNTs (flexible)	–	–		11	0.65	18.8	0.90
ITO	–	–		16	0.83	20.1	0.96
Graphene [193]	625 ± 107	90	Perovskite	14.2	0.70	21.2	0.96
ITO	–	–		17.8	0.83	21.6	0.99
Cu/Graphene [194]	9.6	94.9	PTB7-Th:$PC_{71}BM$	8.5	0.65	16.3	0.80
ITO	–	92.5		8.4	0.67	15.6	0.80
Flex-Graphene [195]	83	92.2	PM6: Y6	15.2	0.702	25.8	0.84
PET-ITO	–	–		14.8	0.726	24.6	0.83
Flex-transfer-free Gr [196]	81 ± 6.5	Ca. 85	Perovskite	14.18	0.73	20.9	0.93
Flex-transferred-Gr	(2 ± 0.12) k	Ca. 82		11.65	0.65	19.7	0.91
Graphene [92]	286 ± 12	90.3	PTB7-Th: $PC_{71}BM$	8.38	0.656	16.5	0.773
ITO	–	–		9.22	0.68	17.12	0.788
Flex-Gr	–	–		7.53	0.62	16.01	0.757
Graphene [197]	73.6	87.5	P3HT:PCBM	2.07	0.48	7.62	0.57
ITO	15	–		2.86	0.62	8.07	0.577
Transfer-free Gr [89]	Ca 1.3 k	67	P3HT:$PC_{71}BM$	1.27	0.45	5.14	0.56
ITO	–	Ca. 81		1.58	0.55	4.95	0.55
Transfer-free Gr [86]	1.92 k	73.3	P3HT: PCBM	1.41	0.47	5.32	0.56
ITO	–	–		2.22	0.60	6.58	0.56
Graphene [198]	300	–	PDTP: PCBM	4.7	0.52	12.8	0.71
ITO	–	–		4.8	0.52	13.1	0.71
Flex-Graphene	–	–		4.1	0.46	12.5	0.71
Flex-ITO	–	–		4.5	0.53	12.3	0.70
Trans-free Gr-AgNW [86]	103	66	P3HT: PCBM	2.18	0.63	6.15	0.56
ITO	–	–		2.22	0.60	6.58	0.56
Trans-free Gr-AgNW	103	66	P3HT: $PC_{71}BM$	2.33	0.61	7.0	0.55
ITO	–	–		2.33	0.57	7.11	0.57
Trans-free Gr-AgNW	103	66	PM6: Y6	9.75	0.59	21.4	0.77
ITO	–	–		10.3	0.59	22.5	0.78
Graphene [94]	>2k– 0.5 k	97	Perovskite	16.1	0.72	21.9	1.03
ITO	9.5	89		18.2	0.83	22.6	0.97

Comparison between different TCEs

	PEDOT: PSS	CNTs	AgNWs	CVD-graphene	ITO
Pros	Solution processability Mechanical flexibility Scalable	Optical transmittance Solution processible High mechanical stability Scalable	High conductivity Excellent optical transmittance Solution-processable Excellent mechanical stability	High optical transmittance High electrical conductivity Excellent mechanical flexibility Excellent chemical stability	Good optical transmittance High electrical conductivity
Cons	Relatively low conductivity Low transmittance at long wavelengths	Random network increases surface roughness. Low conductivity due to poor contact at junctions	High surface roughness Degradation under ambient conditions Weak adhesion to the substrate	Energy-consuming deposition Time-ineffectiveness Hazardous precursors Complex transfer procedures	Poor mechanical stability Low chemical stability High cost Scarcity of indium

benzene) have shown great potential to synthesize graphene at low temperature on Cu foil, but more research in this area is needed to synthesize graphene on glass and polymer substrates. Transfer-free AgNWs-graphene hybridization can produce efficient TCEs at lower expenses and with minimum damage. Controlling the size and height of VG nanosheets can be exploited to suppress the impact of the rough surface of AgNWs above graphene without additional procedures (e.g., hot-rolling) [180]. This should increase the area of interface between the TCE and the photoactive area of the device for better carrier collection. Finally, more effort should be devoted to the pre-treatment of the dielectric substrate prior to graphene synthesis as this can have a significant impact on the graphene quality.

7. Conclusion

This work presents a comprehensive overview of CVD-graphene TCE for OPVs. The progress made in the implementation of CVD-graphene TCEs in OPVs has been thoroughly reviewed. The fundamentals of graphene growth by CVD and plasma enhanced CVD (PE-CVD) on different substrates were discussed in detail. In addition, a discussion of the relevant characterization methods needed for the assessment of graphene TCEs for OPVs and how the graphene features can impact the device performance was systematically given. The advancement in dry and wet transfer methods of CVD-graphene from metal substrates (e.g. Cu foil) onto transparent target substrates (e.g. glass, PET, PEN, etc.) was presented. Moreover, the scalable transfer methods compatible with R2R fabrication of large-area OPVs were covered. Besides, different strategies such as post-treatment and doping for the enhancement of graphene properties for TCE applications were discussed. The recent achievements in transfer-free CVD/PECVD graphene TCEs for OPVs and perovskite solar cells were discussed in detail. The use of CVD reactors with split heating zones showed emerging potential to enable the growth of defect-free graphene onto transparent flexible polymer substrates pre-coated with ultrathin layers of metals with high affinity to carbon (e.g. Ti). Sustainable plant extracts of essential oils are carbon-rich and eco-friendly precursors that can replace traditional hazardous carbon sources such as methane and have been recently reported in transfer-free PECVD graphene TCEs. A detailed comparison between CVD-graphene and other TCE candidates including CNTs, AgNWs, and PEDOT: PSS and ITO, in terms of the device performance, sheet resistance, optical transmittance, pros and cons of each category was provided. The current limitations and potential research directions were also presented to help researchers develop single-step, and green synthesis approaches for scalable CVD/PECVD-graphene TCEs for OPVs and other optoelectronic devices.

Declaration of competing interest

The authors declare that they have no known competing financial interests or personal relationships that could have appeared to influence the work reported in this paper.

Data availability

No data was used for the research described in the article.

Acknowledgement

Michael S. A. Kamel would like to acknowledge financial support by James Cook University through a JCUPRS scholarship.

References

[1] Han C, Wang J, Zhang S, Chen L, Bi F, Wang J, et al. Over 19% efficiency organic solar cells by regulating multidimensional intermolecular interactions. Adv Mater 2023;35:2208986.
[2] Li C, Zhou J, Song J, Xu J, Zhang H, Zhang X, et al. Non-fullerene acceptors with branched side chains and improved molecular packing to exceed 18% efficiency in organic solar cells. Nat Energy 2021;6:605–13.
[3] Liu M, Ge X, Jiang X, Chen D, Guo F, Gao S, et al. 18% efficiency of ternary organic solar cells enabled by integrating a fused perylene diimide guest acceptor. Nano Energy 2023;112:108501.
[4] Kamel MSA, Al-jumaili A, Oelgemöller M, Jacob MV. Inorganic nanoparticles to overcome efficiency inhibitors of organic photovoltaics: an in-depth review. Renew Sustain Energy Rev 2022;166:112661.
[5] Kamel MS, Oelgemöller M, Jacob MV. Sustainable plasma polymer encapsulation materials for organic solar cells. J Mater Chem A 2022;10:4683–94.
[6] Liu X, Chen H, Tan S. Overview of high-efficiency organic photovoltaic materials and devices. Renew Sustain Energy Rev 2015;52:1527–38.
[7] Alkhalayfeh MA, Aziz AA, Pakhuruddin MZ. An overview of enhanced polymer solar cells with embedded plasmonic nanoparticles. Renew Sustain Energy Rev 2021;141:110726.
[8] Søndergaard R, Hösel M, Angmo D, Larsen-Olsen TT, Krebs FC. Roll-to-roll fabrication of polymer solar cells. Mater Today 2012;15:36–49.
[9] Angmo D, Larsen-Olsen TT, Jørgensen M, Søndergaard RR, Krebs FC. Roll-to-Roll inkjet printing and photonic sintering of electrodes for ITO free polymer solar cell modules and facile product integration. Adv Energy Mater 2013;3:172–5.
[10] Liu C, Xiao C, Xie C, Li W. Flexible organic solar cells: materials, large-area fabrication techniques and potential applications. Nano Energy 2021;89:106399.
[11] Ahmad Z, Najeeb MA, Shakoor R, Al-Muhtaseb SA, Touati F. Limits and possible solutions in quantum dot organic solar cells. Renew Sustain Energy Rev 2018;82:1551–64.
[12] Kumavat PP, Sonar P, Dalal DS. An overview on basics of organic and dye sensitized solar cells, their mechanism and recent improvements. Renew Sustain Energy Rev 2017;78:1262–87.
[13] Wang X, Zhi L, Tsao N, Tomović Ž, Li J, Müllen K. Transparent carbon films as electrodes in organic solar cells. Angew Chem Int Ed 2008;47:2990–2.
[14] Kamel MSA, Stoppiello CT, Jacob MV. Single-step, catalyst-free, and green synthesis of graphene transparent electrode for organic photovoltaics. Carbon 2023;202:150–8.
[15] Jin Z, Yan J, Huang X, Xu W, Yang S, Zhu D, et al. Solution-processed transparent coordination polymer electrode for photovoltaic solar cells. Nano Energy 2017;40:376–81.
[16] Oseni SO, Mola GT. Properties of functional layers in inverted thin film organic solar cells. Sol Energy Mater Sol Cell 2017;160:241–56.
[17] Sun Y, Chang M, Meng L, Wan X, Gao H, Zhang Y, et al. Flexible organic photovoltaics based on water-processed silver nanowire electrodes. Nature Electronics 2019;2:513–20.
[18] Du J, Zhang D, Wang X, Jin H, Zhang W, Tong B, et al. Extremely efficient flexible organic solar cells with a graphene transparent anode: dependence on number of layers and doping of graphene. Carbon 2021;171:350–8.
[19] Liu Z, You P, Xie C, Tang G, Yan F. Ultrathin and flexible perovskite solar cells with graphene transparent electrodes. Nano Energy 2016;28:151–7.
[20] Mahmoudi T, Wang Y, Hahn Y-B. Graphene and its derivatives for solar cells application. Nano Energy 2018;47:51–65.
[21] Wu J, Que X, Hu Q, Luo D, Liu T, Liu F, et al. Multi-length scaled silver nanowire grid for application in efficient organic solar cells. Adv Funct Mater 2016;26:4822–8.
[22] Manzano-Ramírez A, López-Naranjo EJ, Soboyejo W, Meas-Vong Y, Vilquin B. A review on the efficiency of graphene-based BHJ organic solar cells. J Nanomater 2015;2015:3.
[23] Espinosa N, García-Valverde R, Urbina A, Krebs FC. A life cycle analysis of polymer solar cell modules prepared using roll-to-roll methods under ambient conditions. Sol Energy Mater Sol Cell 2011;95:1293–302.
[24] Hösel M, Angmo D, Søndergaard RR, dos Reis Benatto GA, Carlé JE, Jørgensen M, et al. High-volume processed, ITO-free superstrates and substrates for roll-to-roll development of organic electronics. Adv Sci 2014;1:1400002.
[25] Sharma S, Shriwastava S, Kumar S, Bhatt K, Tripathi CC. Alternative transparent conducting electrode materials for flexible optoelectronic devices. Opto-Electron Rev 2018;26:223–35.
[26] Sun Y, Zhang W, Chi H, Liu Y, Hou CL, Fang D. Recent development of graphene materials applied in polymer solar cell. Renew Sustain Energy Rev 2015;43:973–80.
[27] Zheng X, Zuo L, Zhao F, Li Y, Chen T, Shan S, et al. High-efficiency ITO-free organic photovoltaics with superior flexibility and up-scalability. Adv Mater 2022:2200044.
[28] Worfolk BJ, Andrews SC, Park S, Reinspach J, Liu N, Toney MF, et al. Ultrahigh electrical conductivity in solution-sheared polymeric transparent films. In: Proceedings of the national academy of sciences, 112; 2015. p. 14138–43.
[29] Ricciardulli AG, Yang S, Wetzelaer GJA, Feng X, Blom PW. Hybrid silver nanowire and graphene-based solution-processed transparent electrode for organic optoelectronics. Adv Funct Mater 2018;28:1706010.
[30] Wu J, Que X, Hu Q, Luo D, Liu T, Liu F, et al. Multi-length scaled silver nanowire grid for application in efficient organic solar cells. Adv Funct Mater 2016;26:4822–8.
[31] Chen X, Xu G, Zeng G, Gu H, Chen H, Xu H, et al. Realizing ultrahigh mechanical flexibility and> 15% efficiency of flexible organic solar cells via a "welding" flexible transparent electrode. Adv Mater 2020;32:1908478.
[32] Huang J, Ren Z, Zhang Y, Liu K, Zhang H, Tang H, et al. Stretchable ITO-free organic solar cells with intrinsic anti-reflection substrate for high-efficiency outdoor and indoor energy harvesting. Adv Funct Mater 2021;31:2010172.

[33] Grilli M, Di Sarcina I, Bossi S, Rinaldi A, Pilloni L, Piegari A. Ultrathin and stable Nickel films as transparent conductive electrodes. Thin Solid Films 2015;594:261–5.
[34] Shtein M. Thin metal films as simple transparent conductors. SPIE Newsroom 2009;10:1848.
[35] Song YS, Seong NJ, Choi KJ, Ryu SO. Optical and electrical properties of transparent conducting gallium-doped ZnO electrodes prepared by atomic layer deposition for application in organic solar cells. Thin Solid Films 2013;546:271–4.
[36] Wan J, Xia Y, Fang J, Zhang Z, Xu B, Jinzhao W, et al. Solution-processed transparent conducting electrodes for flexible organic solar cells with 16.61% efficiency. Nano-Micro Lett 2021;13.
[37] Fan Q, Zhang Q, Zhou W, Yang F, Zhang N, Xiao S, et al. Highly conductive and transparent carbon nanotube-based electrodes for ultrathin and stretchable organic solar cells. Chin Phys B 2017;26:028801.
[38] Basarir F, Irani FS, Kosemen A, Camic BT, Oytun F, Tunaboylu B, et al. Recent progresses on solution-processed silver nanowire based transparent conducting electrodes for organic solar cells. Mater Today Chem 2017;3:60–72.
[39] Lee J-Y, Connor ST, Cui Y, Peumans P. Solution-processed metal nanowire mesh transparent electrodes. Nano Lett 2008;8:689–92.
[40] Zeng G, Chen W, Chen X, Hu Y, Chen Y, Zhang B, et al. Realizing 17.5% efficiency flexible organic solar cells via atomic-level chemical welding of silver nanowire electrodes. J Am Chem Soc 2022;144:8658–68.
[41] Garg R, Elmas S, Nann T, Andersson MR. Deposition methods of graphene as electrode material for organic solar cells. Adv Energy Mater 2017;7:1601393.
[42] Katsnelson MI. Graphene: carbon in two dimensions. Mater Today 2007;10:20–7.
[43] Wassei JK, Kaner RB. Graphene, a promising transparent conductor. Mater Today 2010;13:52–9.
[44] Emmott CJ, Urbina A, Nelson J. Environmental and economic assessment of ITO-free electrodes for organic solar cells. Sol Energy Mater Sol Cell 2012;97:14–21.
[45] Zhang Y, Zhang L, Zhou C. Review of chemical vapor deposition of graphene and related applications. Accounts Chem Res 2013;46:2329–39.
[46] Xin H, Li W. A review on high throughput roll-to-roll manufacturing of chemical vapor deposition graphene. Appl Phys Rev 2018;5:031105.
[47] Saeed M, Alshammari Y, Majeed SA, Al-Nasrallah E. Chemical vapour deposition of graphene—synthesis, characterisation, and applications: a review. Molecules 2020;25:3856.
[48] Lin Y-C, Lu C-C, Yeh C-H, Jin C, Suenaga K, Chiu P-W. Graphene annealing: how clean can it be? Nano Lett 2012;12:414–9.
[49] Lin Y-C, Jin C, Lee J-C, Jen S-F, Suenaga K, Chiu P-W. Clean transfer of graphene for isolation and suspension. ACS Nano 2011;5:2362–8.
[50] Park H, Brown PR, Bulović V, Kong J. Graphene as transparent conducting electrodes in organic photovoltaics: studies in graphene morphology, hole transporting layers, and counter electrodes. Nano Lett 2012;12:133–40.
[51] Zhang Z, Du J, Zhang D, Sun H, Yin L, Ma L, et al. Rosin-enabled ultraclean and damage-free transfer of graphene for large-area flexible organic light-emitting diodes. Nat Commun 2017;8:1–9.
[52] Sun J, Chen Y, Cai X, Ma B, Chen Z, Priydarshi MK, et al. Direct low-temperature synthesis of graphene on various glasses by plasma-enhanced chemical vapor deposition for versatile, cost-effective electrodes. Nano Res 2015;8:3496–504.
[53] Wei N, Li Q, Cong S, Ci H, Song Y, Yang Q, et al. Direct synthesis of flexible graphene glass with macroscopic uniformity enabled by copper-foam-assisted PECVD. J Mater Chem A 2019;7:4813–22.
[54] Tran V-D, Pammi SVN, Park B-J, Han Y, Jeon C, Yoon S-G. Transfer-free graphene electrodes for super-flexible and semi-transparent perovskite solar cells fabricated under ambient air. Nano Energy 2019;65:104018.
[55] Matacena I, Lancellotti L, Lisi N, Delli Veneri P, Guerriero P, Daliento S. Impedance spectroscopy for the characterization of the all-carbon graphene-based solar cell. Energies 2020;13:1908.
[56] Lancellotti L, Bobeico E, Capasso A, Noce MD, Dikonimos T, Lisi N, et al. Effects of HNO3 molecular doping in graphene/Si Schottky barrier solar cells. In: Fotonica AEIT Italian conference on photonics Technologies2014; 2014. p. 1–3.
[57] Park SH, Roy A, Beaupré S, Cho S, Coates N, Moon JS, et al. Bulk heterojunction solar cells with internal quantum efficiency approaching 100%. Nat Photonics 2009;3:297.
[58] Gholizadeh A, Reyhani A, Parvin P, Mortazavi S. Efficiency enhancement of ZnO nanostructure assisted Si solar cell based on fill factor enlargement and UV-blue spectral down-shifting. J Phys Appl Phys 2017;50:185501.
[59] Abdulrazzaq OA, Saini V, Bourdo S, Dervishi E, Biris AS. Organic solar cells: a review of materials, limitations, and possibilities for improvement. Part Sci Technol 2013;31:427–42.
[60] Zhang X, Yao N, Wang R, Li Y, Zhang D, Wu G, et al. On the understanding of energy loss and device fill factor trade-offs in non-fullerene organic solar cells with varied energy levels. Nano Energy 2020;75:105032.
[61] Calvaresi M, Quintana M, Rudolf P, Zerbetto F, Prato M. Rolling up a graphene sheet. ChemPhysChem 2013;14:3447–53.
[62] Allen MJ, Tung VC, Kaner RB. Honeycomb carbon: a review of graphene. Chem Rev 2010;110:132–45.
[63] Sheehy DE, Schmalian J. Optical transparency of graphene as determined by the fine-structure constant. Phys Rev B 2009;80:193411.
[64] Bolotin KI, Sikes K, Jiang Z, Klima M, Fudenberg G, Hone J, et al. Ultrahigh electron mobility in suspended graphene. Solid State Commun 2008;146:351–5.
[65] Novoselov KS, Geim AK, Morozov SV, Jiang D-e, Zhang Y, Dubonos SV, et al. Electric field effect in atomically thin carbon films. Science 2004;306:666–9.
[66] Terrones M, Botello-Méndez AR, Campos-Delgado J, López-Urías F, Vega-Cantú YI, Rodríguez-Macías FJ, et al. Graphene and graphite nanoribbons: morphology, properties, synthesis, defects and applications. Nano Today 2010;5:351–72.
[67] Lloyd-Hughes J, Jeon T-I. A review of the terahertz conductivity of bulk and nano-materials. J Infrared, Millim Terahertz Waves 2012;33:871–925.
[68] Kamel S, El-Sakhawy MA, Anis B, Tohamy H-AS. Graphene: structure, synthesis, and characterization; a brief review. Egypt J Chem 2019;62:593-608.
[69] Lim JY, Mubarak NM, Abdullah EC, Nizamuddin S, Khalid M, Inamuddin. Recent trends in the synthesis of graphene and graphene oxide based nanomaterials for removal of heavy metals — a review. J Ind Eng Chem 2018;66:29–44.
[70] Kumar N, Salehiyan R, Chauke V, Joseph Botlhoko O, Setshedi K, Scriba M, et al. Top-down synthesis of graphene: a comprehensive review. FlatChem 2021;27:100224.
[71] Achee TC, Sun W, Hope JT, Quitzau SG, Sweeney CB, Shah SA, et al. High-yield scalable graphene nanosheet production from compressed graphite using electrochemical exfoliation. Sci Rep 2018;8:14525.
[72] Vacacela Gomez C, Guevara M, Tene T, Villamagua L, Usca GT, Maldonado F, et al. The liquid exfoliation of graphene in polar solvents. Appl Surf Sci 2021;546:149046.
[73] Hummers Jr WS, Offeman RE. Preparation of graphitic oxide. J Am Chem Soc 1958;80:1339.
[74] Toh SY, Loh KS, Kamarudin SK, Daud WRW. Graphene production via electrochemical reduction of graphene oxide: synthesis and characterisation. Chem Eng J 2014;251:422–34.
[75] Guex LG, Sacchi B, Peuvot KF, Andersson RL, Pourrahimi AM, Ström V, et al. Experimental review: chemical reduction of graphene oxide (GO) to reduced graphene oxide (rGO) by aqueous chemistry. Nanoscale 2017;9:9562–71.
[76] Chen W, Yan L. Preparation of graphene by a low-temperature thermal reduction at atmosphere pressure. Nanoscale 2010;2:559–63.
[77] Gutiérrez-Cruz A, Ruiz-Hernández AR, Vega-Clemente JF, Luna-Gazcón DG, Campos-Delgado J. A review of top-down and bottom-up synthesis methods for the production of graphene, graphene oxide and reduced graphene oxide. J Mater Sci 2022;57:14543–78.
[78] Chen X, Zhang L, Chen S. Large area CVD growth of graphene. Synth Met 2015;210:95–108.
[79] Reina A, Thiele S, Jia X, Bhaviripudi S, Dresselhaus MS, Schaefer JA, et al. Growth of large-area single-and bi-layer graphene by controlled carbon precipitation on polycrystalline Ni surfaces. arXiv preprint arXiv:09062236 2009;2:509-516.
[80] Vlassiouk I, Regmi M, Fulvio P, Dai S, Datskos P, Eres G, et al. Role of hydrogen in chemical vapor deposition growth of large single-crystal graphene. ACS Nano 2011;5:6069–76.
[81] Li Z, Wu P, Wang C, Fan X, Zhang W, Zhai X, et al. Low-temperature growth of graphene by chemical vapor deposition using solid and liquid carbon sources. ACS Nano 2011;5:3385–90.
[82] Zhao P, Kumamoto A., Kim S., Chen X., Hou B., Chiashi S., Einarsson E., Ikuhara Y., and Maruyama S. "Self-limiting chemical vapor deposition growth of monolayer graphene from ethanol." *The Journal of Physical Chemistry C* 12013; 117: 10755-10763.
[83] Ma Y, Jang H, Kim SJ, Pang C, Chae H. Copper-assisted direct growth of vertical graphene nanosheets on glass substrates by low-temperature plasma-enhanced chemical vapour deposition process. Nanoscale Res Lett 2015;10:1019.
[84] Li M, Liu D, Wei D, Song X, Wei D, Wee ATS. Controllable synthesis of graphene by plasma-enhanced chemical vapor deposition and its related applications. Adv Sci 2016;3:1600003.
[85] Jiang L, Yang T, Liu F, Dong J, Yao Z, Shen C, et al. Controlled synthesis of large-scale, uniform, vertically standing graphene for high-performance field emitters. Adv Mater 2013;25:250–5.
[86] Kamel MSA, Stoppiello CT, Jacob MV. Improved transfer-free sustainable graphene electrode using silver nanowires for organic photovoltaics. ACS Appl Energy Mater 2023;6:11168–78.
[87] Kamel MSA, Oelgemöller M, Jacob MV. Influence of deposition temperature and hydrogen on sustainable and transfer-free graphene transparent electrode for organic solar cells. FlatChem 2024;44:100627.
[88] Ferrari AC, Meyer JC, Scardaci V, Casiraghi C, Lazzeri M, Mauri F, et al. Raman spectrum of graphene and graphene layers. Phys Rev Lett 2006;97:187401.
[89] Kamel MS, Stoppiello CT, Jacob MV. Single-step, catalyst-free, and green synthesis of graphene transparent electrode for organic photovoltaics. Carbon 2023;202:150–8.
[90] Topsoe H. Geometric factors in four point resistivity measurement. Bulletin 1968;472:63.
[91] Miccoli I, Edler F, Pfnür H, Tegenkamp C. The 100th anniversary of the four-point probe technique: the role of probe geometries in isotropic and anisotropic systems. J Phys Condens Matter 2015;27:223201.
[92] Jung S, Lee J, Choi Y, Lee SM, Yang C, Park H. Improved interface control for high-performance graphene-based organic solar cells. 2D Mater 2017;4:045004.
[93] Gosling JH, Makarovsky O, Wang F, Cottam ND, Greenaway MT, Patanè A, et al. Universal mobility characteristics of graphene originating from charge scattering by ionised impurities. Commun Phys 2021;4:30.
[94] Sung H, Ahn N, Jang MS, Lee JK, Yoon H, Park NG, et al. Transparent conductive oxide-free graphene-based perovskite solar cells with over 17% efficiency. Adv Energy Mater 2016;6:1501873.
[95] Kim KS, Zhao Y, Jang H, Lee SY, Kim JM, Kim KS, et al. Large-scale pattern growth of graphene films for stretchable transparent electrodes. Nature 2009;457:706–10.
[96] Eizenberg M, Blakely J. Carbon monolayer phase condensation on Ni (111). Surf Sci 1979;82:228–36.

[97] Eizenberg M, Blakely J. Carbon interaction with nickel surfaces: monolayer formation and structural stability. J Chem Phys 1979;71:3467–77.
[98] Hamilton J, Blakely J. Carbon segregation to single crystal surfaces of Pt, Pd and Co. Surf Sci 1980;91:199–217.
[99] Somani PR, Somani SP, Umeno M. Planer nano-graphenes from camphor by CVD. Chem Phys Lett 2006;430:56–9.
[100] Obraztsov A, Obraztsova E, Tyurnina A, Zolotukhin A. Chemical vapor deposition of thin graphite films of nanometer thickness. Carbon 2007;45:2017–21.
[101] De Arco LG, Zhang Y, Kumar A, Zhou C. Synthesis, transfer, and devices of single- and few-layer graphene by chemical vapor deposition. IEEE Trans Nanotechnol 2009;8:135–8.
[102] Li X, Cai W, An J, Kim S, Nah J, Yang D, et al. Large-area synthesis of high-quality and uniform graphene films on copper foils. Science 2009;324:1312–4.
[103] Wang Y, Chen X, Zhong Y, Zhu F, Loh KP. Large area, continuous, few-layered graphene as anodes in organic photovoltaic devices. Appl Phys Lett 2009;95:209.
[104] Yu Q, Lian J, Siriponglert S, Li H, Chen YP, Pei S-S. Graphene segregated on Ni surfaces and transferred to insulators. Appl Phys Lett 2008;93:113103.
[105] Reina A, Jia X, Ho J, Nezich D, Son H, Bulovic V, et al. Large area, few-layer graphene films on arbitrary substrates by chemical vapor deposition. Nano Lett 2009;9:30–5.
[106] Gomez De Arco L, Zhang Y, Schlenker CW, Ryu K, Thompson ME, Zhou C. Continuous, highly flexible, and transparent graphene films by chemical vapor deposition for organic photovoltaics. ACS Nano 2010;4:2865–73.
[107] Liu Z, Li J, Sun Z-H, Tai G, Lau S-P, Yan F. The application of highly doped single-layer graphene as the top electrodes of semitransparent organic solar cells. ACS Nano 2012;6:810–8.
[108] Hesjedal T. Continuous roll-to-roll growth of graphene films by chemical vapor deposition. Appl Phys Lett 2011;98:133106.
[109] Kobayashi T, Bando M, Kimura N, Shimizu K, Kadono K, Umezu N, et al. Production of a 100-m-long high-quality graphene transparent conductive film by roll-to-roll chemical vapor deposition and transfer process. Appl Phys Lett 2013;102:023112.
[110] Bae S, Kim H, Lee Y, Xu X, Park J-S, Zheng Y, et al. Roll-to-roll production of 30-inch graphene films for transparent electrodes. Nat Nanotechnol 2010;5:574–8.
[111] Kobayashi T, Bando M, Kimura N, Shimizu K, Kadono K, Umezu N, et al. Production of a 100-m-long high-quality graphene transparent conductive film by roll-to-roll chemical vapor deposition and transfer process. Appl Phys Lett 2013;102:023112.
[112] Jiao L, Fan B, Xian X, Wu Z, Zhang J, Liu Z. Creation of nanostructures with poly(methyl methacrylate)-mediated nanotransfer printing. J Am Chem Soc 2008;130:12612–3.
[113] Li X, Zhu Y, Cai W, Borysiak M, Han B, Chen D, et al. Transfer of large-area graphene films for high-performance transparent conductive electrodes. Nano Lett 2009;9:4359–63.
[114] Her M, Beams R, Novotny L. Graphene transfer with reduced residue. Phys Lett 2013;377:1455–8.
[115] Jeong HJ, Kim HY, Jeong SY, Han JT, Baeg K-J, Hwang JY, et al. Improved transfer of chemical-vapor-deposited graphene through modification of intermolecular interactions and solubility of poly(methylmethacrylate) layers. Carbon 2014;66:612–8.
[116] Johnson BY, Liu X, Mazumder P, Soni KK, Chen T, Marchena M, et al. Transfer of monolayer graphene onto flexible glass substrates. Google Patents; 2017.
[117] Chen X-D, Liu Z-B, Zheng C-Y, Xing F, Yan X-Q, Chen Y, et al. High-quality and efficient transfer of large-area graphene films onto different substrates. Carbon 2013;56:271–8.
[118] Choi W, Shehzad MA, Park S, Seo Y. Influence of removing PMMA residues on surface of CVD graphene using a contact-mode atomic force microscope. RSC Adv 2017;7:6943–9.
[119] Gammelgaard L, Caridad JM, Cagliani A, Mackenzie DMA, Petersen DH, Booth TJ, et al. Graphene transport properties upon exposure to PMMA processing and heat treatments. 2D Mater 2014;1:035005.
[120] Pirkle A, Chan J, Venugopal A, Hinojos D, Magnuson CW, McDonnell S, et al. The effect of chemical residues on the physical and electrical properties of chemical vapor deposited graphene transferred to SiO2. Appl Phys Lett 2011;99:122108.
[121] Yoon T, Shin WC, Kim TY, Mun JH, Kim T-S, Cho BJ. Direct measurement of adhesion energy of monolayer graphene as-grown on copper and its application to renewable transfer process. Nano Lett 2012;12:1448–52.
[122] Caldwell JD, Anderson TJ, Culbertson JC, Jernigan GG, Hobart KD, Kub FJ, et al. Technique for the dry transfer of epitaxial graphene onto arbitrary substrates. ACS Nano 2010;4:1108–14.
[123] Chen C-S, Hsieh C-K. An easy, low-cost method to transfer large-scale graphene onto polyethylene terephthalate as a transparent conductive flexible substrate. Thin Solid Films 2014;570:595–8.
[124] Chen TL, Ghosh DS, Marchena M, Osmond J, Pruneri V. Nanopatterned graphene on a polymer substrate by a direct peel-off technique. ACS Appl Mater Interfaces 2015;7:5938–43.
[125] Malesevic A, Vitchev R, Schouteden K, Volodin A, Zhang L, Van Tendeloo G, et al. Synthesis of few-layer graphene via microwave plasma-enhanced chemical vapour deposition. Nanotechnology 2008;19:305604.
[126] Zhang L, Shi Z, Wang Y, Yang R, Shi D, Zhang G. Catalyst-free growth of nanographene films on various substrates. Nano Res 2011;4:315–21.
[127] Kalita G, Wakita K, Umeno M. Low temperature growth of graphene film by microwave assisted surface wave plasma CVD for transparent electrode application. RSC Adv 2012;2:2815–20.
[128] Sun Z, Yan Z, Yao J, Beitler E, Zhu Y, Tour JM. Growth of graphene from solid carbon sources. Nature 2010;468:549–52.
[129] Jachimowski T, Hagedorn C, Weinberg W. Direct and trapping-mediated dissociative chemisorption of methane on Ir (111). Surf Sci 1997;393:126–34.
[130] Woehrl N, Ochedowski O, Gottlieb S, Shibasaki K, Schulz S. Plasma-enhanced chemical vapor deposition of graphene on copper substrates. AIP Adv 2014;4:047128.
[131] Chan S-H, Chen S-H, Lin W-T, Li M-C, Lin Y-C, Kuo C-C. Low-temperature synthesis of graphene on Cu using plasma-assisted thermal chemical vapor deposition. Nanoscale Res Lett 2013;8:1–5.
[132] Ma Y, Jang H, Kim SJ, Pang C, Chae H. Copper-assisted direct growth of vertical graphene nanosheets on glass substrates by low-temperature plasma-enhanced chemical vapour deposition process. Nanoscale Res Lett 2015;10:1–8.
[133] Dahou FZ, Cattin L, Garnier J, Ouerfelli J, Morsli M, Louarn G, et al. Influence of anode roughness and buffer layer nature on organic solar cells performance. Thin Solid Films 2010;518:6117–22.
[134] Byun S-J, Lim H, Shin G-Y, Han T-H, Oh SH, Ahn J-H, et al. Graphenes converted from polymers. J Phys Chem Lett 2011;2:493–7.
[135] Zhuo Q-Q, Wang Q, Zhang Y-P, Zhang D, Li Q-L, Gao C-H, et al. Transfer-free synthesis of doped and patterned graphene films. ACS Nano 2015;9:594–601.
[136] Park B-J, Choi J-S, Eom J-H, Ha H, Kim HY, Lee S, et al. Defect-free graphene synthesized directly at 150 C via chemical vapor deposition with no transfer. ACS Nano 2018;12:2008–16.
[137] Marchena M, Janner D, Chen TL, Finazzi V, Pruneri V. Low temperature direct growth of graphene patterns on flexible glass substrates catalysed by a sacrificial ultrathin Ni film. Opt Mater Express 2016;6:2487–507.
[138] D'Arsié L, Esconjauregui S, Weatherup RS, Wu X, Arter WE, Sugime H, et al. Stable, efficient p-type doping of graphene by nitric acid. RSC Adv 2016;6:113185–92.
[139] Kim H, Kim HH, Jang JI, Lee SK, Lee GW, Han JT, et al. Doping graphene with an atomically thin two dimensional molecular layer. Adv Mater 2014;26:8141–6.
[140] D'Arsié L, Esconjauregui S, Weatherup R, Guo Y, Bhardwaj S, Centeno A, et al. Stability of graphene doping with MoO3 and I2. Appl Phys Lett 2014;105:103103.
[141] Wei D, Liu Y, Wang Y, Zhang H, Huang L, Yu G. Synthesis of N-doped graphene by chemical vapor deposition and its electrical properties. Nano Lett 2009;9:1752–8.
[142] Wang H, Maiyalagan T, Wang X. Review on recent progress in nitrogen-doped graphene: synthesis, characterization, and its potential applications. ACS Catal 2012;2:781–94.
[143] Sinitskii A, Dimiev A, Corley DA, Fursina AA, Kosynkin DV, Tour JM. Kinetics of diazonium functionalization of chemically converted graphene nanoribbons. ACS Nano 2010;4:1949–54.
[144] Qu L, Liu Y, Baek J-B, Dai L. Nitrogen-doped graphene as efficient metal-free electrocatalyst for oxygen reduction in fuel cells. ACS Nano 2010;4:1321–6.
[145] Song SM, Bong Jh, Cho BJ. Work function tuning of metal/graphene stack electrode. Appl Phys Lett 2014;104:083512.
[146] Rut'kov EV, Afanas'eva EY, Gall NR. Graphene and graphite work function depending on layer number on Re. Diam Relat Mater 2020;101:107576.
[147] Wang Y, Tong SW, Xu XF, Özyilmaz B, Loh KP. Interface engineering of layer-by-layer stacked graphene anodes for high-performance organic solar cells. Adv Mater 2011;23:1514–8.
[148] Kholmanov IN, Magnuson CW, Aliev AE, Li H, Zhang B, Suk JW, et al. Improved electrical conductivity of graphene films integrated with metal nanowires. Nano Lett 2012;12:5679–83.
[149] La Notte L, Villari E, Palma AL, Sacchetti A, Giangregorio MM, Bruno G, et al. Laser-patterned functionalized CVD-graphene as highly transparent conductive electrodes for polymer solar cells. Nanoscale 2017;9:62–9.
[150] Wang Y, Shao Y, Matson DW, Li J, Lin Y. Nitrogen-doped graphene and its application in electrochemical biosensing. ACS Nano 2010;4:1790–8.
[151] Rybin M, Pereyaslavtsev A, Vasilieva T, Myasnikov V, Sokolov I, Pavlova A, et al. Efficient nitrogen doping of graphene by plasma treatment. Carbon 2016;96:196–202.
[152] Moon J, An J, Sim U, Cho S-P, Kang JH, Chung C, et al. One-step synthesis of N-doped graphene quantum sheets from monolayer graphene by nitrogen plasma. Adv Mater 2014;26:3501–5.
[153] Lin Y-C, Lin C-Y, Chiu P-W. Controllable graphene N-doping with ammonia plasma. Appl Phys Lett 2010;96:133110.
[154] Tang Y-B, Yin L-C, Yang Y, Bo X-H, Cao Y-L, Wang H-E, et al. Tunable band gaps and p-type transport properties of boron-doped graphenes by controllable ion doping using reactive microwave plasma. ACS Nano 2012;6:1970–8.
[155] Baeck U, Nguyen DN, Choi M, Kim J, Choe W-S, Lee JY, et al. Boosting hole migration through oxygen species–functionalized graphene interlayer for organic-based optoelectronic devices with enhanced efficiency and long-term durability. Appl Surf Sci 2023;615:156383.
[156] Kim S-H, Noh Y-J, Kwon S-N, Kim B-N, Lee B-C, Yang S-Y, et al. Efficient modification of transparent graphene electrodes by electron beam irradiation for organic solar cells. J Ind Eng Chem 2015;26:210–3.
[157] Guo B, Liu Q, Chen E, Zhu H, Fang L, Gong JR. Controllable N-doping of graphene. Nano Lett 2010;10:4975–80.
[158] Wang X, Li X, Zhang L, Yoon Y, Weber PK, Wang H, et al. N-doping of graphene through electrothermal reactions with ammonia. Science 2009;324:768–71.
[159] Meyer J, Kidambi PR, Bayer BC, Weijtens C, Kuhn A, Centeno A, et al. Metal oxide induced charge transfer doping and band alignment of graphene electrodes for efficient organic light emitting diodes. Sci Rep 2014;4:1–7.
[160] Hellstrom SL, Vosgueritchian M, Stoltenberg RM, Irfan I, Hammock M, Wang YB, et al. Strong and stable doping of carbon nanotubes and graphene by MoO x for transparent electrodes. Nano Lett 2012;12:3574–80.

[161] Lin C-T, Yeh C-H, Chen M-H, Hsu S-H, Wu C-I, Pi T-W. Influences of evaporation temperature on electronic structures and electrical properties of molybdenum oxide in organic light emitting devices. J Appl Phys 2010;107:053703.
[162] Han T-H, Lee Y, Choi M-R, Woo S-H, Bae S-H, Hong BH, et al. Extremely efficient flexible organic light-emitting diodes with modified graphene anode. Nat Photonics 2012;6:105–10.
[163] Kasry A, Kuroda MA, Martyna GJ, Tulevski GS, Bol AA. Chemical doping of large-area stacked graphene films for use as transparent, conducting electrodes. ACS Nano 2010;4:3839–44.
[164] Kim KK, Reina A, Shi Y, Park H, Li L-J, Lee YH, et al. Enhancing the conductivity of transparent graphene films via doping. Nanotechnology 2010;21:285205.
[165] Gunes F, Shin H-J, Biswas C, Han GH, Kim ES, Chae SJ, et al. Layer-by-layer doping of few-layer graphene film. ACS Nano 2010;4:4595–600.
[166] Kwon KC, Choi KS, Kim SY. Increased work function in few-layer graphene sheets via metal chloride doping. Adv Funct Mater 2012;22:4724–31.
[167] Syu J-Y, Chen Y-M, Xu K-X, He S-M, Hung W-C, Chang C-L, et al. Wide-range work-function tuning of active graphene transparent electrodes via hole doping. RSC Adv 2016;6:32746–56.
[168] Kwon S-J, Han T-H, Ko TY, Li N, Kim Y, Kim DJ, et al. Extremely stable graphene electrodes doped with macromolecular acid. Nat Commun 2018;9:2037.
[169] Kim D, Lee D, Lee Y, Jeon DY. Work-function engineering of graphene anode by bis (trifluoromethanesulfonyl) amide doping for efficient polymer light-emitting diodes. Adv Funct Mater 2013;23:5049–55.
[170] Ni G-X, Zheng Y, Bae S, Tan CY, Kahya O, Wu J, et al. Graphene–ferroelectric hybrid structure for flexible transparent electrodes. ACS Nano 2012;6:3935–42.
[171] Morozov S, Novoselov K, Katsnelson M, Schedin F, Elias DC, Jaszczak JA, et al. Giant intrinsic carrier mobilities in graphene and its bilayer. Phys Rev Lett 2008;100:016602.
[172] Jeong C, Nair P, Khan M, Lundstrom M, Alam MA. Prospects for nanowire-doped polycrystalline graphene films for ultratransparent, highly conductive electrodes. Nano Lett 2011;11:5020–5.
[173] Hu L, Kim HS, Lee J-Y, Peumans P, Cui Y. Scalable coating and properties of transparent, flexible, silver nanowire electrodes. ACS Nano 2010;4:2955–63.
[174] Garnett EC, Cai W, Cha JJ, Mahmood F, Connor ST, Greyson Christoforo M, et al. Self-limited plasmonic welding of silver nanowire junctions. Nat Mater 2012;11:241–9.
[175] Lee D, Lee H, Ahn Y, Jeong Y, Lee D-Y, Lee Y. Highly stable and flexible silver nanowire–graphene hybrid transparent conducting electrodes for emerging optoelectronic devices. Nanoscale 2013;5:7750–5.
[176] Ye N, Yan J, Xie S, Kong Y, Liang T, Chen H, et al. Silver nanowire–graphene hybrid transparent conductive electrodes for highly efficient inverted organic solar cells. Nanotechnology 2017;28:305402.
[177] Ye N, Liang T, Zhan L, Kong Y, Xie S, Ma X, et al. High-performance bendable organic solar cells with silver nanowire-graphene hybrid electrode. IEEE J Photovoltaics 2018;9:214–9.
[178] Grossiord N, Kroon JM, Andriessen R, Blom PW. Degradation mechanisms in organic photovoltaic devices. Org Electron 2012;13:432–56.
[179] Chen R, Das SR, Jeong C, Khan MR, Janes DB, Alam MA. Co-percolating graphene-wrapped silver nanowire network for high performance, highly stable, transparent conducting electrodes. Adv Funct Mater 2013;23:5150–8.
[180] Hosseinzadeh Khaligh H, Goldthorpe IA. Hot-rolling nanowire transparent electrodes for surface roughness minimization. Nanoscale Res Lett 2014;9:1–5.
[181] Zhang W, Song W, Huang J, Huang L, Yan T, Ge J, et al. Graphene: silver nanowire composite transparent electrode based flexible organic solar cells with 13.4% efficiency. J Mater Chem A 2019;7:22021–8.
[182] Seo TH, Park AH, Park S, Chandramohan S, Lee GH, Kim MJ, et al. Improving the graphene electrode performance in ultra-violet light emitting diode using silver nanowire networks. Opt Mater Express 2015;5:314–22.
[183] Li H, Liu Y, Su A, Wang J, Duan Y. Promising hybrid graphene-silver nanowire composite electrode for flexible organic light-emitting diodes. Sci Rep 2019;9:1–10.
[184] Seo K-W, Lee J-H, Cho NG, Kang SJ, Kim H-K, Na S-I, et al. Simple brush painted Ag nanowire network on graphene sheets for flexible organic solar cells. J Vac Sci Technol A: Vacuum, Surfaces, and Films 2014;32:061201.
[185] Zhang Q, Di Y, Huard CM, Guo LJ, Wei J, Guo J. Highly stable and stretchable graphene–polymer processed silver nanowires hybrid electrodes for flexible displays. J Mater Chem C 2015;3:1528–36.
[186] Shin DH, Seo SW, Kim JM, Lee HS, Choi S-H. Graphene transparent conductive electrodes doped with graphene quantum dots-mixed silver nanowires for highly-flexible organic solar cells. J Alloys Compd 2018;744:1–6.
[187] Niu C. Carbon nanotube transparent conducting films. MRS Bull 2011;36:766–73.
[188] Song W, Fan X, Xu B, Yan F, Cui H, Wei Q, et al. All-solution-processed metal-oxide-free flexible organic solar cells with over 10% efficiency. Adv Mater 2018;30:1800075.
[189] Ahlswede E, Mühleisen W, bin Moh Wahi MW, Hanisch J, Powalla M. Highly efficient organic solar cells with printable low-cost transparent contacts. Appl Phys Lett 2008;92.
[190] Dong X, Shi P, Sun L, Li J, Qin F, Xiong S, et al. Flexible nonfullerene organic solar cells based on embedded silver nanowires with an efficiency up to 11.6. J Mater Chem A 2019;7:1989–95.
[191] Jeon I, Cui K, Chiba T, Anisimov A, Nasibulin AG, Kauppinen EI, et al. Direct and dry deposited single-walled carbon nanotube films doped with MoO x as electron-blocking transparent electrodes for flexible organic solar cells. J Am Chem Soc 2015;137:7982–5.
[192] Jeon I, Yoon J, Kim U, Lee C, Xiang R, Shawky A, et al. High-performance solution-processed double-walled carbon nanotube transparent electrode for perovskite solar cells. Adv Energy Mater 2019;9:1901204.
[193] Jeon I, Yoon J, Ahn N, Atwa M, Delacou C, Anisimov A, et al. Carbon nanotubes versus graphene as flexible transparent electrodes in inverted perovskite solar cells. J Phys Chem Lett 2017;8:5395–401.
[194] Jeong G, Jung S, Choi Y, Lee J, Seo J, Kim DS, et al. A highly robust and stable graphene-encapsulated Cu-grid hybrid transparent electrode demonstrating superior performance in organic solar cells. J Mater Chem A 2018;6:24805–13.
[195] Koo D, Jung S, Seo J, Jeong G, Choi Y, Lee J, et al. Flexible organic solar cells over 15% efficiency with polyimide-integrated graphene electrodes. Joule 2020;4:1021–34.
[196] Tran V-D, Pammi S, Park B-J, Han Y, Jeon C, Yoon S-G. Transfer-free graphene electrodes for super-flexible and semi-transparent perovskite solar cells fabricated under ambient air. Nano Energy 2019;65:104018.
[197] Kim K, Bae S-H, Toh CT, Kim H, Cho JH, Whang D, et al. Ultrathin organic solar cells with graphene doped by ferroelectric polarization. ACS Appl Mater Interfaces 2014;6:3299–304.
[198] Song Y, Chang S, Gradecak S, Kong J. Visibly-transparent organic solar cells on flexible substrates with all-graphene electrodes. Adv Energy Mater 2016;6:1600847.